University of Hamburg

Dissertation

Mechanisms of Picosecond Infrared Laser Desorption Ionization

submitted by

Frederik Busse

in partial fulfillment of the requirements for the degree of Doctor of Philosophy at the

Faculty of Mathematics, Informatics, and Natural Sciences

Department of Physics at the University of Hamburg

Hamburg, April 2019

Frederik Busse

Mechanisms of Picosecond Infrared Laser Desorption Ionization

Gutachter der Dissertation:

Prof. Dr. R. J. Dwayne Miller

Prof. Dr. Robert H. Blick

Zusammensetzung der Prüfungskommission:

Prof. Dr. R. J. Dwayne Miller

Prof. Dr. Robert H. Blick

Prof. Dr. Daniela Pfannkuche

Prof. Dr. Arwen Pearson

Dr. Sadia Bari

Vorsitzende der Prüfungskommission:

Prof. Dr. Daniela Pfannkuche

Datum der Disputation:

15.07.2019

Vorsitzender des Fach-Promotionsausschusses Physik:

Prof. Dr. Michael Potthoff

Leiter des Fachbereichs Physik:

Prof. Dr. Wolfgang Hansen

Dekan der Fakultät MIN:

Prof. Dr. Heinrich Graener

Eidesstattliche Versicherung

Hiermit erkläre ich an Eides statt, dass ich die vorliegende Dissertationsschrift selbst verfasst und keine anderen als die angegebenen Quellen und Hilfsmittel benutzt habe.

Hamburg, den 30.04.2019 Frederik Busse

List of publications

This thesis is in part based on the following publications:

- E. C. Schulz, J. Kaub, **F. Busse**, P. Mehrabi, H. M. Müller-Werkmeister, E. F. Pai, W. D. Robertson, and R. J. D. Miller: *Protein crystals IR laser ablated from aqueous solution at high speed retain their diffractive properties: applications in high-speed serial crystallography.* Journal of Applied Crystallography, vol. 50, no. 6, pp. 1773–1781, Dec. 2017. DOI: 10.1107/S1600576717014479 [1]

- **F. Busse**, S. Kruber, W. D. Robertson, and R. J. D. Miller: *Digital interference microscopy and density reconstruction of picosecond infrared laser desorption at the water-air interface.* Journal of Applied Physics, vol. 124, no. 9, p. 094701, Sep. 2018. DOI: 10.1063/1.5030741 [2]

Abstract

Direct analysis of tissues and cells by mass spectrometry is an emerging approach in guided laser surgery, high-throughput clinical bio-diagnostics, and mass spectrometry imaging. Especially for the analysis of labile compounds such as large proteins and non-covalently bound complexes, a soft sampling technique which preserves the integrity of the analyte molecules is desirable. Infrared (IR) laser desorption is a promising method for soft material extraction as it provides high spatial resolution, requires minimal sample preparation, and can be easily coupled to purification and separation techniques such as liquid chromatography. A core limitation to be overcome is the relatively low ionization efficiency when compared to other techniques commonly used with mass spectrometry, such as matrix assisted laser desorption ionization (MALDI) or electrospray ionization (ESI).

By using a picosecond infrared laser (PIRL) at 3 µm wavelength, desorption by impulsive vibrational excitation (DIVE) establishes optimal ablation conditions. Depositing energy at a higher rate than it can be dissipated by mechanical relaxation leads to a maximal pressure buildup before material ejection ensues, and to less collateral material damage since dissipation channels corresponding to thermal as well as acoustic damage to the specimen are reduced. This leaves even large biomolecules intact for subsequent analysis.

Within the scope of this thesis, the ablation and ionization characteristics of PIRL-DIVE were investigated in two different scenarios: first, the material ejection at atmospheric pressure was characterized using time-resolved digital interference microscopy, a photographic technique which showed high contrast for otherwise transparent objects such as acoustic shocks and ejected water vapor. Different ablation regimes exhibiting varying amounts of liquid and vapor-phase material were identified, and droplet generation could be suppressed when smaller volumes of liquid were irradiated. This opened up possibilities to further investigate the role of droplet generation and desolvation in analyte ionization. Second, the suitability of PIRL-DIVE for mass spectrometry imaging was investigated in a custom-built time-of-flight mass analyzer. Substantial improvements in signal strength, stability, and reproducibility were achieved compared to previous IR laser desorption ionization studies performed under vacuum conditions. The influence of several parameters such as laser fluence, extraction voltage, and pH value of the sample solution was investigated. The sample preparation protocol had significant impact on the observed signal quality. The obtained results potentially pave the way towards high-resolution, high-sensitivity mass spectrometry imaging from frozen cryo-sections of tissues and cells using the DIVE process.

Zusammenfassung

Die direkte massenspektrometrische Analyse von Geweben und Zellen ist ein relativ neuer Ansatz in der computergestützten Laser-Chirurgie, in der klinischen Biodiagnostik und im Gebiet der massenspektrometrischen Bildgebung. Vor allem für die Analyse labiler Stoffe wie besonders großer Moleküle und nicht-kovalent gebundener Komplexe ist eine Untersuchungsmethode wünschenswert, welche die Integrität der Analytmoleküle bewahrt. Die Infrarot (IR) Laserdesorption ist eine vielversprechende Methode zur "weichen" Probenentnahme, die eine hohe räumliche Auflösung bei minimaler Probenvorbereitung bietet und sich leicht an Aufreinigungs- und Separationstechniken wie die Flüssigchromatographie koppeln lässt. Bisher limitierend ist die relativ niedrige Ionisationseffizienz im Vergleich mit anderen Massenspektrometrie-Methoden wie zum Beispiel der Matrix-unterstützten Laserdesorption und Ionisation (MALDI) und der Elektrospray Ionisation (ESI).

Optimale Ablationsbedingungen können durch die Nutzung eines Pikosekunden Infrarot Lasers (PIRL) mit einer Wellenlänge von 3 µm erreicht werden, ein Verfahren welches auch *Desorption by Impulsive Vibrational Excitation* (DIVE) genannt wird. Wird die Energie schneller zugeführt als sie durch mechanische Relaxation abgebaut werden kann, wird ein maximaler Ablationsdruck erreicht und das umliegenden Gewebe weniger beansprucht, da sowohl thermische als auch akustische Dissipationskanäle, die zu Schäden an der Probe führen könnten, vermieden werden. Selbst große Biomoleküle bleiben so für die weitere Analyse intakt.

Ziel dieser Arbeit war die Untersuchung der PIRL Ablation und Ionisation in zwei unterschiedlichen Szenarien: Zunächst wurde der Materialausstoß unter Atmosphärendruck mittels zeitaufgelöster digitaler Interferenzmikroskopie charakterisiert, ein photographisches Verfahren mit welchem ein hoher Kontrast für ansonsten transparente Objekte wie Druckwellen und Wasserdampf erzielt werden konnte. Verschiedene Regimes der Materialablation wiesen unterschiedliche Verhältnisse von flüssigem zu gasförmigem Material auf, wobei die Tröpfchenbildung für die Ablation von mikroskopischen Flüssigkeitsvolumen vollständig unterdrückt werden konnte. Dies zeigte eine Möglichkeit zur weiteren Untersuchung der Rolle der Tröpfchenbildung und -desolvatisierung für die Ionisierung von Analytmolekülen auf. Des Weiteren wurde die Eignung von PIRL-DIVE für die massenspektrometrische Bildgebung untersucht. Dazu wurde ein Flugzeit-Massenspektrometer aufgebaut und charakterisiert und der Einfluss mehrerer Parameter wie der Laser-Fluenz, der Extraktionsspannung und des pH-Werts geprüft. Es konnte eine wesentliche Verbesserung der Signalstärke, -stabilität und -reproduzierbarkeit im Vergleich zu vorhergehenden Studien der IR Laserdesorption und Ionisation unter Vakuumbedingungen demonstriert werden. Zudem wurde gezeigt, dass besonders die Probenvorbereitung eine wichtige Rolle für die Signalqualität spielte. Die erzielten Ergebnisse ebnen potenziell den Weg für eine hochauflösende und hoch-sensible massenspektrometrische Bildgebung von gefrorenen Probenschnitten mittels DIVE.

Contents

Chapter 1

Introduction

Classical light-microscopy deceivingly presents an image of the cell resembling a well-organized compartment which contains a nucleus, a few organelles, and lots of empty space enclosed by the cell membrane. However, the cytosol which fills this space is comprised of a vast variety of different molecules, many of which interact to perform key metabolomic functions. For example, electrochemical gradients or the binding of ligands such as adenosine triphosphate (ATP) can cause transmembrane proteins to initiate conformational changes that make them permeable for specific molecules. Enzymes can modify other molecules and cause post-translational modifications of proteins to regulate their chemical activity. Molecular chaperones ensure correct protein folding and prevent unwanted aggregation, processes which are critical for the functionality of the cell. The high biomolecule concentrations in this crowded environment can significantly alter the behavior of individual molecules with respect to more dilute conditions. The cell can thus be understood as a complex system governed by the strong interactions between its constituents. If these interactions are disrupted, this can lead to atypical cellular function and disease, such as alzheimers and cancer. Understanding the spatial correlations between different biomolecules is essential for understanding the system as a whole.

One technique capable of investigating these correlations is mass spectrometry imaging (MSI) [3–6]. Mass spectrometry (MS) is an untargeted technique capable of detecting, identifying, and quantitating molecules without having to previously label them. It also offers enormous sensitivity, facilitating the detection of compounds over a large range of concentrations. Spatial resolution is achieved by ablating different locations on the sample surface using a laser, and introducing the produced vapor into the mass analyzer. The success and vast proliferation of laser-based mass spectrometry devices – even without making explicit use of spatial mapping – is largely owed to the development of matrix assisted laser desorption ionization (MALDI) in the 1980s [7, 8], a technique in which the laser energy is not directly absorbed by the analyte compound, but by small organic molecules which

are admixed to the sample. This "matrix" enables a particularly soft and sensitive way of vaporization and ionization in the sense that large molecules can be detected with only little fragmentation and from samples containing only low concentrations of analytes. While the commercial application of MALDI has been highly successful, the method continues to suffer from certain shortcomings, most importantly the intricacies of choosing the right matrix, difficulties in sample preparation, and limited reproducibility [9]. These have proven to be major hurdles for the development of quantitative MALDI protocols [10]. Moreover, fundamental studies have struggled to give accurate predictions for optimal parameter sets and the resulting mass spectra [11, 12]. Over the years, a picture of a two-step process has emerged [13–15], in which the final outcome of a MALDI experiment is determined both by the hydrodynamics of the material ejection and by chemical reactions proceeding in the hot cloud of ejected matter, also called the ablation plume, but the description is far from complete.

Besides, little effort has so far been spent on developing similar models for infrared laser desorption ionization (IR-LDI) [16]. With this technique, ablation and ionization can be achieved without the addition of a reactive matrix, which would greatly simplify mass spectrometry workflows if the process was made sufficiently efficient. Reasons for the so far little popularity of IR-LDI include the high cost of suitable laser sources and the comparably low ionization efficiency, but are also due to the fast takeoff of UV-MALDI which left other techniques behind [16]. For many applications in analytical biochemistry and especially for MSI, water would be a particularly convenient matrix as it is endogenous to many samples of interest, including cells, tissues, and bodily fluids. Water shows strong optical absorption in the mid-infrared, where its O−H stretching vibration can be efficiently excited without affecting those vibrational modes which are prevalent in most biomolecules. Due to the strong hydrogen-bond network of water, the deposited energy is very quickly redistributed from the initial vibrational mode and converted into heat, which facilitates an impulsive increase in temperature. Such desorption by impulsive vibrational excitation (DIVE), which can be implemented with sub-nanosecond laser pulses at roughly 3 µm wavelength, has been postulated to facilitate particularly efficient ablation and ionization [17]. A reduction of the energy loss from heat diffusion and from rapid mechanical relaxation in form of acoustic transients results in very high initial pressure gradients which are believed to lead to faster evaporative cooling of the analyte ions, and ultimately to a softer ablation process.

Increasing the efficiency of IR-LDI could have a major impact on clinical diagnostics and mass spectrometry imaging. In the former, vaporization under atmospheric conditions and a reduction of the complexity of the sample preparation are desirable to increase throughput [18]. This can allow for the analysis of biomolecules to be performed in a

more natural aqueous solvent, and decrease waiting times in a clinical environment, ideally yielding on-line information during treatment or surgery. In the latter, i.e. in MSI, detection sensitivity is often the limiting factor in reducing the pixel size of a molecular map further [5]. Moreover, a "top-down" approach to proteomics, which requires a soft ablation method such as IR-LDI, could help to increase the information content gained from an MS experiment by preserving a protein's complete structure and removing ambiguities in identification [19]. DIVE could thus form a critical step towards the development of top-down MSI, and ultimately to the recording of the full molecular map of the cell.

This work aims to investigate the ablation and ionization under DIVE conditions and to explore the method's potential for mass spectrometry imaging. A brief overview of the developed models describing the ionization processes of MALDI will be given in the first half of chapter 2 of this thesis, before previous studies concerning DIVE and possible applications thereof will be summarized in the second half. In chapter 3, a photographic method named digital interference microscopy (DIM) is employed to characterize the plume dynamics initiated by picosecond infrared laser (PIRL) irradiation under atmospheric conditions. Potential differences between stress-confined and merely thermally confined ablation are examined, and the role of droplets, vapor phase material, and plasma generation is discussed in the context of ion generation. Chapter 4 deals with the application of PIRL-DIVE in the vacuum of a time-of-flight mass spectrometer (TOF-MS). Ablation under vacuum conditions is likely necessary to perform high-resolution MSI with high sensitivity, as this way less material is lost during transfer to the detector compared to ablation in atmosphere. The increase in initial pressure generated under DIVE conditions can be expected to be a big advantage for TOF-MS, because a more forward-peaked material ejection increases the collection efficiency and reduces the spread of the resulting ion arrival times. Moreover, stronger evaporative cooling should lead to a reduction in internal ion energies and thus to reduced ion fragmentation. To investigate these effects, a linear time-of-flight mass spectrometer was constructed which facilitated the analysis of thin samples at cryogenic temperatures in both front-side and back-side ablation. The investigation of frozen samples containing water ice under vacuum is challenging because water will evaporate quickly unless sufficiently cooled, and condensation of ambient air must be avoided during sample preparation and transfer. Previous studies with nanosecond IR irradiation had shown no significant ion yield for proteins in bulk water ice in a TOF geometry [20, 21], which was surprising given that excellent spectra could be acquired from proteins dissolved in glycerol [22] and even from air-dried and subsequently frozen protein-layers [20] under the same conditions. This thesis revisits the problem in the regime of PIRL-DIVE.

Chapter 2

Laser Desorption in Mass Spectrometry

This chapter starts out by giving a brief historical overview over the most important desorption and ionization methods used in mass spectrometry. Then, the different proposed models for laser-based techniques are reviewed. Based on an understanding of the various processes relevant to desorption and ionization, advantages of the method investigated in the current work are outlined. The chapter concludes with applications and current trends of infrared laser desorption.

Within the last 100 years, mass spectrometry (MS) has developed into a field encompassing a multitude of different ion generation and detection methods, each with their own advantages and shortcomings [7]. The first ion sources [23] used either thermal ionization (TI) or electron impact ionization (EI) and were thus limited to thermally stable and easily vaporizable compounds with low mass number. More labile molecules would simply fragment and the parent- or molecular ion would not be discernible in the recorded mass spectrum. As interest grew to investigate heavier and organic molecules starting in the 1940s, new methods were invented that could generate gas phase ions with masses in the range of several thousand Da [8]. A selection of these methods is depicted in fig. 2.1.

Chemical ionization (CI), first demonstrated in 1966 [24], relies on gas-phase reactions between the analyte molecules and a charged carrier gas through which ionized analyte species are produced. Compared to EI, in which ions are created by collisions with fast electrons (usually around 70 to 100 eV), CI imparts much less internal energy onto the analyte ions. The amount of surplus energy on the final ions strongly depends on the exothermicity of the gas-phase reaction, a concept also applicable to other ionization methods as described below. The amount of ionization and fragmentation can thus be controlled by the choice of carrier gas, e.g. by changing from H_2 with a proton affinity (PA) of 424 kJ/mol to methane (PA = 552 kJ/mol) to ammonia (PA = 854 kJ/mol) [25]. This control provides the means to acquire structural information, as molecules will typically break at the most labile bond.

Field desorption (FD) is capable of producing ions directly from the solid state and was

thus of major interest for the many cases involving nonvolatile compounds such as peptides, nucleotides, and carbohydrates. First introduced in 1969 [26], the method is based on creating a very strong electric field around a sharp emitter tip. Typically a thin tungsten wire covered with field-enhancing micro-needles (or "whiskers") is used so as to increase the number of active sites, and is coated with the analyte compound. Analyte desorption is triggered by thermal activation (heating) of the emitter. Several fundamental ionization mechanisms are believed to contribute to the final ion yield [27]: thermally desorbed neutrals can be ionized in the gas phase via electron tunneling in the strong electric field of the emitter. Less volatile analytes can be desorbed via field assisted ion evaporation/desolvation if ionization takes place within the sample surface prior to evaporation. A radical cation $M^{\bullet+}$ is formed if the strong polarization by the external field leads to the withdrawal of an electron. Alternatively, ions such as salts can be preformed, or intermolecular reactions such as protonation or cation attachment can lead to ionization. The latter becomes apparent in the mass spectrum in form of a dominant peak of the quasi-molecular ion $[M + A]^+$ instead of the molecular ion M^+, where A is the proton or cation (usually an alkali metal). Elevated temperatures increase the diffusion of these charged molecules towards a desorption site where charge accumulates, lowering the barrier for evaporation. Finally, at high temperatures, thermal ionization can contribute to the ion yield independent of the applied extraction field.

Laser desorption ionization (LDI) from metallic or silicon surfaces was developed starting in the 1960s, and the first intact quasi-molecular ions of nonvolatile compounds generated by this technique were demonstrated in 1970 [28]. Again, a number of processes is expected to contribute to desorption and ionization in LDI, as will be discussed in section 2.1. Although the method had some success in the analysis of industrial polymers, oligosaccharides, and lipids, the achievable mass range did not surpass few kDa [29]. Minimal sample preparation and simple integration with existing mass spectrometers and workflows nonetheless make LDI an interesting technique even today. For example, a more recent variant, desorption ionization on porous silicon (DIOS) [30] makes use of the high surface area and strong optical absorption of a nanostructured substrate surface to achieve a higher sensitivity (femto- to attomole) and minimal background signal for small organic molecules (up to 3 kDa [31]) such as peptides.

Fast atom bombardment (FAB) was the first method that could reliably produce ions of larger molecules such as complex carbohydrates, biopolymers, and proteins. It is a sputtering technique in which desorption and ionization is achieved by directing a beam of either ions (similar to secondary ion mass spectrometry, SIMS) or neutrals (similar to plasma desorption, PD) at the sample surface. It was shown in 1981 [32, 33] that when

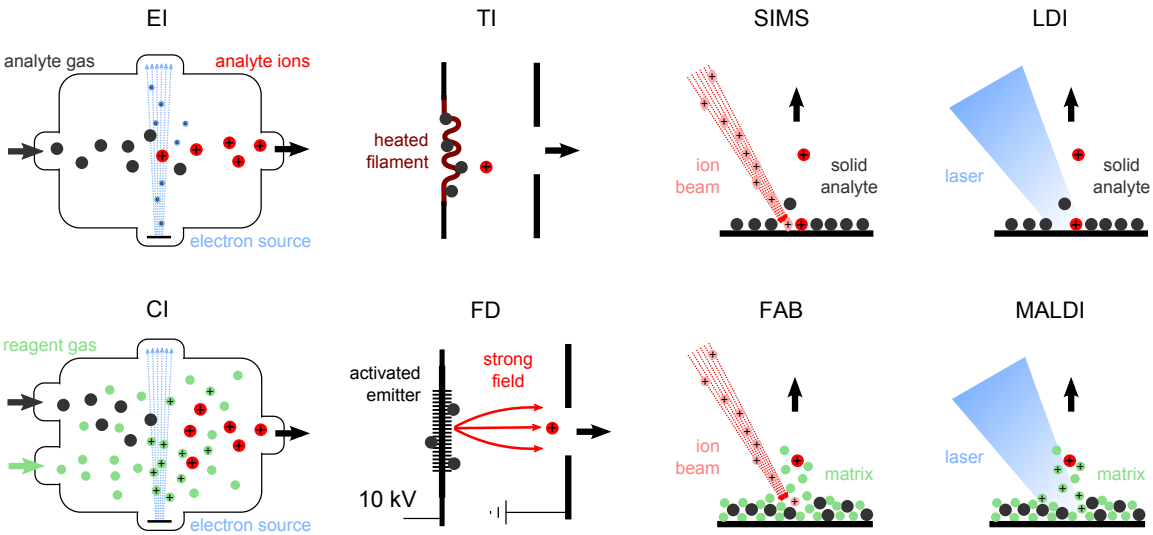

Figure 2.1: Illustration of several popular ionization techniques used in mass spectrometry: electron impact ionization (EI), chemical ionization (CI), thermal ionization (TI), field desorption (FD), secondary ion mass spectrometry (SIMS), fast atom bombardment (FAB), laser desorption ionization (LDI), and matrix assisted laser desorption ionization (MALDI).

the sample was mixed with a nonvolatile liquid matrix such a glycerol – instead of letting it dry out before insertion into the mass spectrometer which was done in the standard preparation – the number of spectra that could be acquired from one sample position could be increased drastically and sensitivity was improved. This way, a variety of analytes could be successfully detected including proteins up to a mass of 24 kDa.

The breakthrough for desorption ionization of nonvolatile and high-mass compounds brought about by the use of a matrix into which the analyte was dissolved quickly spread into other ionization techniques. Electrospray ionization (ESI) and matrix assisted laser desorption ionization (MALDI) have become the two most widely used ionization methods for biomolecule identification of today. In ESI, first demonstrated by John B. Fenn et al. in 1988 [34], a fine mist of charged droplets is produced by pumping an analyte solution through a metal capillary at a high electric potential with respect to the mass spectrometer inlet [35]. Charge accumulates in the liquid facing the extraction electrode until the Coulomb-forces distort the surface into a Taylor-Cone. The electric potential pulls the liquid out of the nozzle and disperses it into a fine mist, which then undergoes solvent evaporation. Because the evaporating molecules are mostly neutral, but the droplets are statistically charged according to the charge accumulation in the Taylor cone, the charge density on individual droplets increases. Once it approaches the Rayleigh-limit, a new Taylor cone can form on the droplet surface and eject a set of smaller charged droplets. The final analyte ion is formed by either ion evaporation, which is similar to the ion extraction process described for

field desorption (FD), or by full solvent evaporation which is described by the charge residue model. What is remarkable about ESI as an ionization mechanism is, on the one hand, that there is seemingly no upper mass limit, because charged analyte molecules are protected from thermal damage by evaporative cooling, and, on the other hand, that the final ions typically accumulate a large number of charges [35]. This makes the method particularly interesting for mass analyzers with high precision but limited mass range [8].

First experiments with a liquid matrix for laser desorption were presented in 1988 by K. Tanaka et al. with an approach very similar to that taken in FAB [36]. The addition of cobalt nanoparticles to a glycerol matrix yielded sufficient optical absorption of the 337 nm light produced by a N_2 laser, and detection of intact proteins with masses up to 34 kDa and clusters of lysozyme with masses up to 100 kDa were demonstrated. This method became known as soft laser desorption (SLD). At about the same time, F. Hillenkamp and M. Karas were working on their own matrix based technique, MALDI, in which the analyte is embedded in a layer of small organic molecules with high optical absorption [37, 38]. Only shortly after Tanaka's success, MALDI was demonstrated to facilitate desorption and ionization of proteins as large as 67 kDa [39]. Having a higher sensitivity than SLD, it gained popularity quickly, and was shown to facilitate the detection of ions with molecular masses of more than 300 kDa [40]. The current understanding of the mechanistic aspects of laser-based desorption ionization techniques shall be briefly summarized in the following sections, with a focus on the processes occurring under vacuum conditions such as those of time-of-flight mass analyzers.

2.1 Matrix-free Laser Desorption Ionization (LDI)

In matrix-free laser desorption ionization, the analyte can be directly applied to a surface for analysis and does not need to be mixed with a matrix, which greatly simplifies sample preparation. Moreover, no additional matrix peaks are introduced into the mass spectrum, which can be beneficial for the analysis of small molecular compounds otherwise shadowed by the matrix and its fragment ions. Interest in the research of LDI for larger molecules, however, faded with the advent of MALDI, and developments until this time are summarized in refs. [29, 41]. Following F. Hillenkamp [41], four possible pathways lead to desorption and ionization in LDI from a solid sample:

1. thermal evaporation of neutral molecules with subsequent ionization in the gas phase,
2. thermal evaporation of preformed ions,
3. ion formation in a laser-generated plasma, and
4. collective, non-equilibrium processes.

Desorption in the first two mechanisms is simply caused by heating, and thus very similar to thermal ionization (TI). There, the ratio of positively charged ions n^+ to neutrals n_0 emitted from a heated metal filament can be described by the Langmuir-Saha equation [27],

$$\frac{n^+}{n_0} \propto e^{-(\Delta E_{\mathrm{ion}} - W)/k_{\mathrm{B}}T}, \tag{2.1}$$

where W is the electronic work function of the surface, ΔE_{ion} is the ionization potential, k_{B} is the Boltzmann-constant, and T is the surface temperature. This assumes that the system is in complete thermal equilibrium. The ionization efficiency can be tuned by an applied electrostatic potential or by changing the surface properties, both of which will affect the work function. The rate of desorption is given by the Arrhenius equation

$$\frac{dN}{dt} \propto (N_0 - N)\, e^{-\Delta E/k_{\mathrm{B}}T}, \tag{2.2}$$

where dN/dt is the desorption rate, N the number of emitted molecules per unit surface area, N_0 is the initial surface coverage, and ΔE is the activation energy for this process [42]. Preformed ions can be detected at lower temperatures because they only need to overcome the desorption barrier and not reach the typically higher ionization potential [29]. Thermal desorption ionization can be the dominating process in LDI in case of long laser pulses (above about 1 µs), if large focus diameters are used, or if the laser fluence is considerably above the ion detection threshold [29]. The initial kinetic energy of the ions will then be in the thermal regime ($\sim 0.3\,\mathrm{eV}$), and ion emission can last for tens of microseconds, severely deteriorating the mass resolution on time-of-flight mass analyzers which rely on an impulsive ionization event [29].

At very high laser fluences (typically above $10^{10}\,\mathrm{W/cm^2}$), or when high irradiances are reached using short pulses, strong photo-ionization can lead to the formation of a plasma on the sample surface [41]. Free electrons strongly absorb the incoming laser irradiation and shield the sample from further energy deposition. Such an optical breakdown leads to major disintegration of the analyte and should thus be avoided for the analysis of organic compounds.

Prompt desorption and ionization within the first about 10 ns of laser incidence is indicative of an ablative process in which a global thermal equilibrium is not reached, and in which the final ion species result from gas-phase reactions in the dense initial material cloud. A shock-wave driven ablation process explains the high initial kinetic energies observed for micro-focused, short-pulse LDI, and also the production of large molecule-clusters and their size distribution [41]. Ions can even be observed when the laser is not striking the sample

directly, but is incident from the backside of the metal support [43]. Because ablation and in-plume ionization require much lower analyte temperatures than thermal evaporation and ionization, lower fragmentation rates and a higher mass limit can be observed in this regime.

New interest in LDI was sparked with the observation of direct desorption ionization on porous silicon surfaces (DIOS) using a simple N_2 laser which is used on most commercial mass spectrometers [30]. Two roles of the silicon surface have been postulated [31]: first, silicon's high optical absorption at 337 nm leads to efficient energy deposition, and second, the high surface roughness traps and isolates the analyte molecules so that energy can be easily transferred. The technique has large potential for rapid biomarker identification when the surface is chemically modified to specifically bind to the analyte, a method called surface enhanced laser desorption ionization (SELDI) [44]. Surface modification similar to that of chromatographic stationary phases facilitates sample concentration and cleanup as the analyte is immobilized by the substrate's functional groups. Less complex and more sensitive spectra are produced by washing off spurious salts, detergents, buffers, and unbound organic molecules before MS analysis. Such surface modifications could also be interesting for analysis by infrared laser desorption ionization (IR-LDI).

Indeed, although UV lasers, particularly the N_2 laser, are most commonly used for laser-based MS due to their low cost and good reliability, the first laser-generated molecular ions of large organic compounds were demonstrated using IR-LDI [45]. More recent studies explored silicon and other transparent substrates for IR-LDI in an effort to elucidate the primary ionization pathways of DIOS and as a potential application of IR-LDI to SELDI substrates and showed desorption and ionization of proteins with molecular masses up to 17 kDa [46–48]. It has been suggested that solvent-desorption plays a significant role in the success of IR-LDI [20, 46–49]. In this model, the O−H, N−H, or C−H vibrational modes of residual solvents absorb incoming mid-IR radiation, leading to evaporation of the small molecules and similar desorption and ionization processes as in FAB or MALDI as described in section 2.2 below. In another study [50], most of the infrared absorption was found to be caused by the analyte, leading to the fragmentation of a portion of these molecules which would then act as a sacrificial matrix to produce intact molecular ions of the remaining analyte. This mechanism was in fact proposed for the UV irradiation of amino acids even before the demonstration of MALDI [37] and was what lead Hillenkamp and Karas to develop their technique.

2.2 Matrix Assisted Laser Desorption Ionization (MALDI)

In MALDI, the (usually aqueous) analyte solution is mixed with a light-absorbing, organic matrix compound in a molar matrix-to-analyte ratio of typically above 1000:1. A small droplet of the mixture is applied to a metal surface and left to dry, which leads to the formation of matrix crystals into which the analyte molecules are embedded. Guidelines for the selection or design of suitable matrix compounds have for example been compiled by R. Cramer [51]. Generally, matrices should possess sufficiently high absorption at the irradiation laser wavelength, should be soluble in an analyte-compatible solvent and co-crystallize with the analyte molecules, and should act as proton donors or acceptors (depending on the desired polarity of the ions). Their volatility should be low enough to ensure stability in the vacuum of a mass analyzer, but not too low to hinder desorption. Extensive reviews of the proposed mechanisms governing MALDI can be found in an issue of *Chemical Reviews* from 2003 [13,14,52,53], with updates by the same authors in 2006 [15] and 2014 [54,55], in addition to the historical perspective already mentioned [8]. Several models have been suggested to describe the ionization process:

1. the coupled photophysical and chemical dynamics model (gas phase model),
2. the cluster ionization model (lucky survivors model), and
3. several thermal models (polar fluid, thermal proton transfer).

The complexity of MALDI stems from the fact that desorption and ionization are two distinct but strongly coupled processes which need to be simultaneously optimized. As hinted in section 2.1, desorption is a term historically motivated from a picture of thermal evaporation of individual molecules. Most MALDI experiments are, however, performed in an ablative regime, in which rapid energy deposition causes the sample to undergo an explosive phase transition [52]. A simple model to describe the number of molecules N ejected in such an ablation event per unit surface area as a function of laser fluence F is given by

$$N = nL \ln\left[\frac{F}{L(\Delta E - CT_0)}\right], \tag{2.3}$$

where n is the molecular number density of the sample, L is the laser penetration depth, ΔE is the internal energy required for ablation, C is the sample's heat capacity and T_0 the initial sample temperature [52]. The logarithmic function reflects the experimentally observed fluence threshold which is a parameter often drawn upon to understand the driving processes of desorption and ionization.

A key prerequisite in MALDI is that the absorption of laser irradiation is predominantly due to the matrix. This is why lasers operating in the near-UV (N_2 laser at 337 nm,

frequency-tripled Nd:YAG laser at 355 nm) or mid-IR (Er:YAG at 2.94 µm, Er:YSGG at 2.79 µm, tunable OPO sources) wavelength regimes, where matrix absorption is considerably higher than that of most biomolecules, have been more successful than laser sources operating at shorter wavelengths (such as excimer and frequency-quadrupled Nd:YAG lasers emitting at 308, 266, and 248 nm) [13]. How the absorbed energy leads to analyte ionization is, however, described differently in each of the aforementioned models.

In the coupled photophysical and chemical dynamics model (CPCD) proposed by R. Knochenmuss [12, 15, 56–65], initial charge separation is achieved by single-photon excitation of the matrix into an excited state and subsequent exciton pooling in the dense ablation plume. Because the ionization potentials of typical matrices are considerably higher than the photon energy of near-UV lasers, requiring two- or even three-photon processes for direct photo-ionization, the energy pooling step described by this model is critical at the low laser fluence commonly employed [58, 66]. The experimentally observed ion yields point towards the existence of highly mobile excitations (called excitons) which are transferred between excited-state and ground-state molecules if several such excitations are to combine.

Charge transfer to the analyte is assumed to be a secondary step, meaning that analyte ions form only after evaporation, which is why the CPCD model is also sometimes referred to as the gas-phase proton-transfer model. Similarly to chemical ionization (CI), charge is preferentially transferred to the most energetically favorable product, and the reaction rates can be approximated assuming local thermal equilibrium and using gas-phase properties of the involved molecules. Secondary reactions producing analyte ions include matrix adduct formation and proton transfer between matrix and analyte. Temperature and density distributions have been computed via a set of coupled rate equations [56, 57, 60, 63], and by using molecular dynamics simulations which employed a breathing sphere model for the internal degrees of freedom of the reactants [59, 61, 62]. With respect to detail and usability, the CPCD model is presently the most successful description of the UV-MALDI process, although it is not applicable to IR-MALDI in which the initial electronic excitation is absent.

In the cluster ionization model [11, 14, 67–69], preformed analyte ions are incorporated into matrix crystals during sample preparation, but stay closely associated with their respective counterions. This notion derives from the fact that most peptides and proteins are protonated when in solution phase at pH values typically used for MALDI preparations. Initial charge separation in this model results from statistical charging of droplets and clusters ejected in the explosive ablation process, similar to the mechanism behind ESI, and is thus wavelength-independent (given sufficient optical absorption). It was historically termed the ”lucky survivors”-model to emphasize how charged analyte ions are released by a lack of neutralizing counterions and by statistically evading neutralization by photoe-

lectrons or electrons from the metallic target [67]. To also explain MALDI mass spectra of positively pre-charged species taken with negative extraction voltage, counterion neutralization and analyte deprotonation by pre-charged matrix molecules, which are created by charge disproportionation / autoprotolysis, i.e. the proton transfer reaction $2\,\mathrm{M} \longrightarrow [\mathrm{M} + \mathrm{H}]^+ + [\mathrm{M} - \mathrm{H}]^-$, and subsequent separation during ablation, was included in the model [14]. Evidence for cluster generation in MALDI has been given in form of flight time measurements which showed delayed ion formation for static [70] and delayed ion extraction [68, 71], in form of chemical background noise in MALDI mass spectra [72], and can be drawn from droplet patterns of ejecta captured on a plate [73]. However, it remains an open question why ESI produces mainly multiply charged ions, whereas MALDI ions are typically singly charged. Increased neutralization rates by photoelectrons for multiply charged clusters [14], a balance of hard and soft desolvation of clusters [68, 69, 71], and a dependency of cluster desolvation rates on cluster size and internal temperature [74] have been proposed to explain the charge state distribution. There are indications that a higher laser fluence favors the CPCD mechanism, but that the cluster model becomes increasingly relevant with increasing molecular weight [11].

Thermal ionization models [15,75] are based on the observation that spectra produced from IR and UV-MALDI of the same matrix are very similar [76]. Primary ions can be generated in the quasi thermal equilibrium of the early plume from ground-state autoprotolysis of the matrix [76, 77], from thermal ionization of excited matrix molecules [78, 79], or from a proton transfer reaction between matrix and analyte molecules [75, 80–82]. Matrix autoprotolysis has been estimated to have a very low reaction rate for typical MALDI plume temperatures given its large energy barrier [83]. In the polar fluid model [76, 77], this barrier is lowered by charge screening through polar solvent or matrix in the dense plume environment. Whether the Coulomb-interaction between associated ion pairs can be lowered sufficiently to be the dominant ionization mechanism is still being discussed [55, 84–86], as polarizabilities are strongly reduced at the high temperatures expected in the ablation plume. It has been noted, however, that solvent polarizability could increase ionization rates in other models such as the CPCD model as a secondary effect, and that water has one of the highest polarizabilities among common matrices and solvents [15]. An explicit application of the model to IR-LDI of aqueous solutions has not yet been demonstrated. The polar fluid model has however been expanded to make quantitative predictions of the ion yield and ion-to-neutral ratio in MALDI experiments [75, 80–82].

2.3 More about Infrared (IR-) MALDI

Although MALDI is, as noted in the beginning of this chapter, a method particularly well suited for the desorption and ionization of large biomolecules, most MALDI applications are rather concerned with peptides, lipids and oligomers with masses in the few kDa regime. The well-established bottom-up approach of proteomics stipulates enzymatic or chemical digestion of larger proteins into well defined subunits before mass spectrometric analysis. This and the high cost of suitable IR laser sources might explain why IR-MALDI, despite it showing several improvements over UV-MALDI for the analysis of large proteins [16,22,76,87,88], has so far not been of major commercial interest. On the other hand, a top-down approach for protein identification could alleviate some of the current problems of MS-based proteomics, such as incomplete sequence coverage due to a loss of peptides, ambiguities in peptide assignment to their parent protein, and the resulting loss of information about protein degradation, sequence variation, and post-translational modifications [19]. Such an approach requires particularly soft desorption and ionization.

Several differences between UV- and IR-MALDI have been observed under vacuum conditions. Due to the lower optical absorption of typical IR matrices, the laser penetration depth is larger and about 100 – 1000 times more material is removed per laser shot at a comparable ion yield. Accumulating only a few spectra for each sample location – instead of several tens to hundreds in UV-MALDI – results in a loss of sensitivity. Limits of detection in the low femtomole instead of the mid to low attomole regime have been demonstrated [22]. The increase in sample consumption also leads to an increase in shot-to-shot fluctuations as ions originate from different distances to the extraction electrode, an issue which is further exacerbated by the need to change the location on the sample frequently, especially when samples are inhomogeneous. This leads to a loss of mass resolution in time-of-flight instruments. Thin-film sample preparation to avoid inhomogeneities [88] or the use of liquid matrices are known to reduce shot-to-shot fluctuations [89].

An analysis of the charge state distribution and of the formation of adducts and oligomers can help to identify unknown analytes, characterize the conformation of proteins, and give insights into the ionization mechanism. Although most comparisons of IR and UV-MALDI in TOF instruments show very similar spectra, a slightly increased appearance of higher charge-states has been noted for IR irradiation when using the same sample and a matrix suitable for both wavelengths [76]. Significant charging up to M^{13+} has been observed for large proteins in caffeic acid, but not for other matrices, for which multiple charging is usually limited to three or four [90]. For glycerol as a matrix, strong oligomer peaks are often visible in the spectrum, and the maximum of the weight distribution can

be shifted by adjusting the extraction field or pH conditions [22, 91, 92]. Formation of hetero-oligomers in IR-MALDI from succinic acid has been stated to be indicative of softer ablation conditions [76]. While in contrast to the UV case, photochemical matrix adducts are usually absent from IR-MALDI spectra because the matrix molecules don't undergo strong electronic excitation, increased cationization by alkali salts is considered to be the reason for the typically observed high-mass tail [76, 87].

The mean initial ion velocity of peptides in the 1 kDa mass range has been shown to be slightly higher in IR-MALDI compared to the UV [93] resulting in a decrease in mass resolution under static extraction field conditions [22]. However, a resolution similar to that found in UV-MALDI can be reached with delayed ion extraction [22, 87, 92]. A reflectron design which compensates for the initial energy spread can further increase the mass resolution. The Hillenkamp group showed improved performance for IR-MALDI in this respect for analytes with molecular masses exceeding 50 kDa [22, 92]. Ions produced by IR-MALDI typically sustain less internal energy than those from UV-MALDI, resulting in a reduced amount of metastable fragmentation during their flight through the analyzer. This post-source decay can severely limit the sensitivity of reflectron-time-of-flight (reTOF) devices for UV-MALDI of large molecules. While analytes with molecular masses up to 150 kDa and their clusters have been measured with slightly reduced metastable fragmentation in IR-MALDI from solid matrices (typically IgG monoclonal antibody in succinic acid at 3 µm wavelength or in fumaric acid at 10 µm wavelength) [22, 76, 92], no obvious differences between IR and UV-MALDI were found for these samples regarding the usable mass range or mass resolution, and choice of matrix rather than wavelength has been considered to be the larger influence on metastable fragmentation [88]. Much better results were achieved by using liquid matrices such as glycerol, with which analyte ions well above 500 kDa could be detected [22, 89, 92]. This is very similar to Tanaka's approach of soft laser desorption (SLD), but because glycerol readily absorbs in the IR, an additional matrix substance is not necessary.

Most investigations of IR-MALDI and IR-LDI deal with the wavelength regions around 2 to 4 µm and 10.6 µm due to both the availability of suitable laser sources and the infrared absorption spectra of typical matrix compounds. Figure 2.2 displays the characteristic vibrational bands of the most relevant functional groups absorbing in the mid-IR. Water, featuring abundant O−H bonds, presents itself as a natural matrix choice for bioanalytics: it is inherently a part of the sample so that analytes can be probed in their natural environment, and helps to preserve their native conformation and any noncovalent superunits which might be lost in the highly non-physiological environment formed by other matrices. Several studies have investigated the use of water ice as an IR-matrix for application in conventional

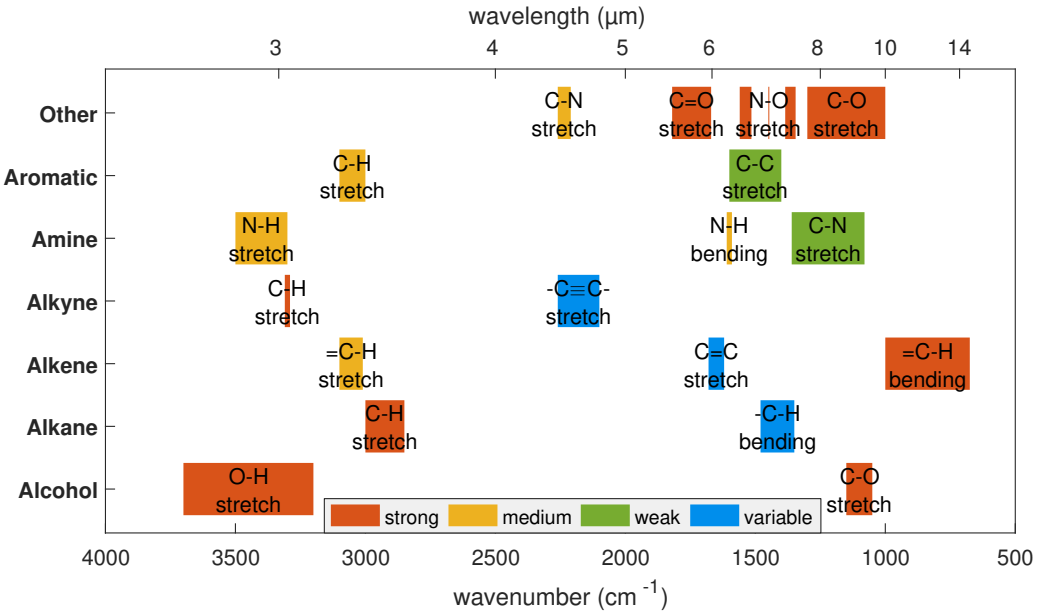

Figure 2.2: Characteristic absorption bands of the most relevant functional groups.[1]

time-of-flight (TOF) [20, 21] and orthogonal injection instruments [94, 95], but have so far not proven very successful. For TOF instruments, the presence of a thick ice layer [20] or a high water content in mixtures of glycerol and water [96] actually seemed to inhibit ion formation. This is rather surprising as water exhibits several properties which should make it a better matrix than glycerol: water is a highly polar molecule with a dielectric constant of 79 compared to 43 for glycerol, which should aid charge separation and ion stabilization according to the polar fluid model. With an absorbance of $12\,000\,\mathrm{cm}^{-1}$ [97] versus $2700\,\mathrm{cm}^{-1}$ [96] at 2.94 µm wavelength, the mid-IR absorption band of water is stronger (compare fig. 2.3), which should lead to higher energy densities in the early stages of ablation. A reason might by that while the evaporation enthalpy of water at standard conditions ($44\,\mathrm{kJ\,mol}^{-1}$) is lower than that of glycerol ($92\,\mathrm{kJ\,mol}^{-1}$), water has to be cooled to be stable under vacuum conditions and the sublimation enthalpy for water ice at 80 K is higher ($149\,\mathrm{kJ\,mol}^{-1}$) than that of glycerol at room temperature. Both the optical absorption and the enthalpy difference should, in accordance with the simple ablation model presented in eq. (2.3), influence the threshold of ablation.

The influence of the pulse duration on MALDI ion formation has been studied extensively both experimentally and in simulations [54, 98]. Energy conversion of excited vibrational states into heat is especially efficient for water, facilitating an exceptionally fast initiation of

[1] Based on data compiled by J. Hansen, University of Puget Sound, WA, USA
http://www2.ups.edu/faculty/hanson/Spectroscopy/IR/IRfrequencies.html

the phase transition into the gas phase, as will be discussed in section 2.4. A number of time scales are known to determine the dominant photoexcitation and ablation mechanisms. Thermal confinement conditions are achieved when heat diffusion only causes negligible dissipation of energy during the laser pulse over the length scale of the ablation volume. If the deposited energy can then not be sufficiently dissipated by evaporation, the irradiated material becomes superheated, a metastable state characterized by an increased boiling rate due to the high temperature. With enough energy being deposited, such that the critical temperature, the spinodal limit, is reached, which for water is about 300 °C at atmospheric pressure, the system undergoes spontaneous decomposition into a mixture of vapor and liquid phase material, which leads to a sudden jump in pressure and induces ablation. It has been estimated that the volumetric energy density necessary to heat water from room temperature to the spinodal limit is only about half of that required for classical vaporization [98]. This form of explosive boiling is called a phase explosion.

For UV-MALDI, where optical penetration depths are typically around 30 to 200 nm, the thermal diffusion time can be estimated to be about 10 ns [13], only slightly above the pulse duration of typical UV lasers. For IR-MALDI on the other hand, where optical penetration depths are much longer, namely around 0.5 to 10 µm, the thermal diffusion time is around 1 µs, and the regime of thermal confinement can thus be reached with much longer pulses.

Conditions of stress confinement can be achieved for even shorter pulse durations, for which energy transport by both thermal diffusion and by acoustic pressure waves is negligible. This leads to a buildup of substantial hydrodynamic pressure and the generation of bipolar stress waves which, once the material's cohesive forces are exceeded, lead to spallation, i.e. mechanical breakup of the material. Relatively large chunks of the sample can be ejected in this way without substantial evaporation, indicating an exceptionally cold ablation process, as has been shown in the molecular dynamics work by L. Zhigilei [52]. The amount of resulting vaporized or fully desolvated material can be influenced by raising the laser fluence further above the threshold of ablation. Counter-intuitively, larger laser fluences can lead to smaller final internal temperatures of the analyte molecules, as a more violent phase explosion will cause faster evaporative cooling of the ejected droplets and clusters. Higher initial pressures, as they are caused by stress confinement, also lead to lower translational plume temperatures, i.e. a more directed material emission away from the sample surface. The shockwave propagation time (or characteristic time scale of stress confinement) has been estimated to be around 17 to 50 ps for UV-MALDI [13], and is around 1 ns for IR-MALDI. It is noteworthy that the plume expansion kinetics are limited by the time it takes for thermalization of the deposited energy. Fluorescence studies have shown that excited singlet state lifetimes of typical UV-MALDI matrices are of the order of 0.2 to 1 ns [13], meaning

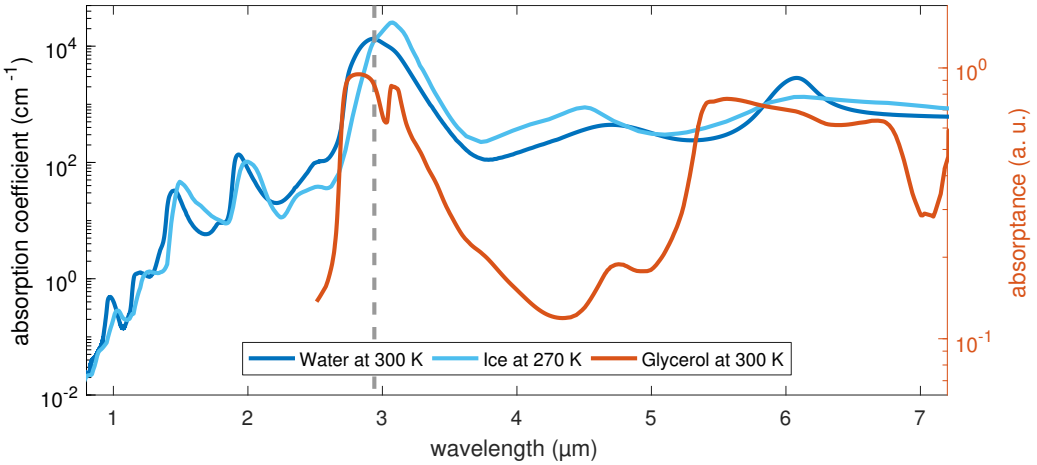

Figure 2.3: Absorption of water, ice, and glycerol. The dashed line marks the maximum of the water absorption band at 2.94 μm. The glycerol absorption spectrum is normalized (right ordinate).[2]

that heating rates for these materials will always be above the stress confinement regime [15]. This might explain why no large differences have been observed between spectra produced from fs or ps UV-MALDI compared to those from ns pulses [99, 100].

Shorter pulses can, however, lead to a change in the photoexcitation mechanism. A change from a ladder-switching to a ladder-climbing process for the primary ionization of 2,5-dihydroxybenzoic acid (DHB) has been postulated to cause significantly less matrix fragmentation because multiphoton ionization can forestall the slower fragmentation pathway [101]. Nonlinear excitation with ultrashort pulses can also be used to desorb matrix-free samples or samples with otherwise transparent matrices [13]. On the other hand, a significantly reduced upper mass limit has been reported for femtosecond UV-MALDI and increased photo-dissociation can be expected due to non-linear absorption by the analyte [102]. In general, energy deposition under nonlinear absorption conditions is more sample-dependent due to the more complex nonlinear absorption spectra.

2.4 Desorption by Impulsive Vibrational Excitation (DIVE)

Combining the resonant excitation of a native matrix material with the efficiency of ablation of short pulses under stress confinement conditions could be key for many applications involving laser ablation of thermo-labile materials. Targeting the water O−H stretching

[2] Based on the following data:
Appl. Spectrosc. 50, 1047 - 1057 (1996) https://sites.ualberta.ca/~jbertie/JBDownload.HTM
J. Geophys. Res., 113, D14220 (2008) http://www.atmos.washington.edu/ice_optical_constants/
Spectral Database for Organic Compounds (SDBS) https://sdbs.db.aist.go.jp

vibration for such impulsive energy deposition is especially promising because the water vibrational states are strongly coupled through its hydrogen bond network. As discussed by K. Franjic and R. J. D. Miller [17,103], the laser energy is quickly redistributed and complete thermalization of an initial O−H excitation is reached within only a few picoseconds, such that the phase transition can begin with minimal delay. Emphasizing the importance of this regime, Franjic and Miller coined the term desorption by impulsive vibrational excitation (DIVE) for the excitation of water with picosecond pulses at 2.94 µm wavelength. Under these conditions, efficient energy redistribution into thermal modes can be ensured by keeping the irradiance low enough to avoid nonlinear optical excitation of higher-lying molecular states, while at the same time depositing enough energy for ablation.

DIVE has special relevance for laser surgery, where the high efficiency of energy conversion from light into motion of the surface layer helps to avoid the build-up of residual heat in the sample, thus leading to smaller damage regions around the cut and potentially to faster healing rates [103–106]. An in-depth review of the mechanisms of tissue ablation including the stress confinement regime has been composed by A. Vogel and V. Venugopalan [98]. Buildup of sufficient hydrodynamic pressure is even more important in this case than for typical MALDI samples, because the tissue's extracellular matrix poses a strong barrier against evaporation and ablation. The tensile forces created under stress confinement can help to weaken these structures so that ablation can proceed at lower temperatures than what would be necessary with longer pulses.

Tissue ablation under DIVE conditions has been shown to preserve molecular integrity to the point that whole viruses could be ablated and transferred to a plant leaf where they resumed to be active [107]. Extraction of tissues for subsequent off-line analysis has been demonstrated to result in continued enzyme activity [108] and lower amounts of laser-induced protein degradation as compared to mechanical homogenization [109] or extraction with microsecond IR-pulses from an Er:YAG laser [110]. DIVE has also been used for on-line MS coupling, namely for direct ablation from a water droplet containing analytes [111] and in combination with ESI postionization for MS imaging [112]. In both off-line and on-line experiments, the material is extracted as a fine mist containing mostly droplets and solid chunks of tissue. Such cold ejecta can also be generated from laser-tissue interaction outside the DIVE regime, and can e.g. be observed for microsecond Er:YAG laser-extraction [110]. However, if the irradiated tissue volume is not fully extracted or significant energy diffuses away from the spot of excitation, residual heat or photochemical residues accumulate and lead to sample degradation, spoiling the material for the next ablation event. These results suggest that DIVE ablation offers significant advantages for ablation under ambient conditions [113]. Recent molecular dynamics (MD) simulations

promote that desolvation and charge separation induced by DIVE ablation can also generate ions directly from aqueous samples in vacuo [114]. The efficiency of DIVE under vacuum conditions will be investigated as part of this thesis.

2.5 Atmospherically Coupled Techniques

Proteomics workflows typically involve at least one separation step such as liquid chromatography (LC) or electrophoresis prior to mass spectrometric analysis to remove impurities, reduce sample complexity, and prevent ion suppression between different species [19]. In liquid chromatography, the sample is dissolved in a solvent mixture, referred to as the mobile phase, and pumped through a column filled with an adsorbent, the stationary phase. Separation between different analyte species in the sample is based on their solubility and the interaction with the adsorbent. Depending on their size, structure, and functional groups, the analytes have different retention times so that different fractions can be collected or probed one by one. In a similar fashion, in thin-layer chromatography (TLC) separation is achieved by dropping analyte and solvent onto a spongy surface and letting them diffuse laterally. Following a different approach, ionic species can be separated as a function of their mobility and charge by having them migrate through a viscous or porous medium in a homogeneous electric field, such as in polyacrylamide gel electrophoresis (PAGE) and capillary electrophoresis (CE).

Combinations of several of these separation steps might be desirable depending on the complexity of the sample. They can be performed either off-line, by collecting fractions of the separation effluent or cutting bands out of a gel, or on-line by directly introducing the liquid or gel into the mass spectrometer [115]. While coupling liquid phase techniques (LC, CE) to ESI is rather straight-forward, only few investigations have treated their on-line coupling to laser ablation, as this typically requires more complex and expensive instrumentation in terms of the laser, additional pumps, etc. Off-line coupling of MALDI-MS offers several advantages over ESI such as greater tolerance for sample impurities, reduced spectral complexity due to mainly singly charged ions, and compatibility with simple and inexpensive time-of-flight (TOF) mass spectrometers. However, this requires the efficient separation and handling of small sample volumes, the rather time-consuming MALDI sample preparation, and the laborious insertion into the vacuum of a mass analyzer.

Simpler sample introduction and higher throughput can be achieved when the sample is vaporized at atmospheric pressure, and the vacuum requirements of MALDI were overcome by simply replacing the ESI source of a commercial mass spectrometer with a laser ablation setup, a technique called atmospheric pressure (AP-) MALDI [116]. However, performing

MALDI of large biomolecules on atmospherically coupled mass analyzers with higher mass resolution and precision, such as Fourier transform ion cyclotron resonance (FT-ICR) or Orbitrap mass spectrometers, becomes possible only when the analyte ions are multiply charged, as these instruments provide a much smaller working m/z range than TOF instruments. This issue was tackled by D. C. Muddiman and coworkers who introduced matrix assisted laser desorption electrospray ionization (MALDESI), in which multiple charging similar to that observed in ESI is achieved by capturing the ejected material in the droplets of an electrospray [117].

Even with these improvements, there is a large demand for further simplification of the sample preparation process, and a multitude of techniques has been developed for the analysis of specimens in their native state [18]. IR-lasers can be advantageously used in such ambient MS approaches due to their soft ablation and the sizable amount of material that is sampled per shot, which allows to access deeper sample layers. Several studies have investigated direct IR laser desorption from solutions similar to those used in liquid chromatography without any additional post-ionization [111, 118–125]. Again, the exact mechanism leading to ionization is unclear, since in contrast to ESI, predominantly singly charged ions have been reported for the analysis of small peptides from water [118, 125]. Other studies found that higher charge states similar to those observed in ESI can be produced under certain conditions [123] or for larger molecules [120]. A recent study using a PIRL for AP-LDI showed a high charge state distribution even for the small peptide angiotensin I [111]. This suggests that droplet generation and desolvation are crucial in the ion-generation process.

IR-ablation can be especially useful to sample deeper layers of tissues, gel preparations, or TLC plates. However, poor collection efficiency of the ablation plume and a low ion yield can reduce the applicability of the technique to real-life problems. In this respect, continuous-flow solvent capture is a promising approach for simplifying the workflow of laser-based MS [126–128]. Apart from ESI, atmospheric pressure chemical ionization (APCI) and inductively coupled plasma ionization (ICP) are commonly used to increase the ion yield of AP laser desorption, although they are generally not suitable for large biomolecules due to the harsh ionization conditions. Low-polarity and nonpolar compounds which are typically difficult to detect in ESI have been successfully ionized in laser ablation atmospheric pressure photoionization (LAAPPI), which uses a jet of hot solvent vapor and irradiation by a UV discharge lamp [129, 130], and in laser-induced postionization [131].

Other than in proteomics, in life sciences such as forensics and clinical diagnostics, not all recorded ions have to be identified, and determining the concentration of certain biomarkers such as specific lipids is often satisfactory. To be practicable in a clinical environment,

spatial separation of the material sampling and the mass spectrometric detection is desired. Several potential techniques for the in-vivo extraction of tissue and on-line coupling to an atmospheric ion source have been demonstrated. In the commercially developed intelligent knife (iKnife) system, tissue is vaporized by using an electric scalpel which strongly heats the surrounding material in a radiofrequency field [132, 133]. The resulting aerosol or smoke is aspirated using a Venturi gas jet pump and transported through a long tube towards the mass analyzer. The ionization method is also known as rapid evaporative ionization mass spectrometry (REIMS), and ion production has been attributed to droplet desolvation similar to that known from spraying techniques such as ESI with no significant contribution from the plasma arch of the electrosurgical device [132]. Softer evaporation conditions and smaller sampling volumes are achieved by IR laser ablation. In remote-LAESI (laser ablation electrospray ionization), the ablated aerosol is pushed through a transport tube by a steady flow of nitrogen gas and intercepted with an electrospray plume for ionization [134, 135]. Different regions of plant leaves could be distinguished based on the content of small metabolites and lipids. Finally, sufficient ions to distinguish several lipids, fatty acids, and diacylglycerols were produced by directly coupling the aerosol generated by IR-LDI into an ion-trap MS in a system called SpiderMass [136, 137]. Principal components analysis of the acquired spectra was used to discern volunteers based on their gender after direct sampling from their finger tips, demonstrating the large potential of AP-IR-LDI for in-situ tissue analysis.

As discussed in the previous sections, methods based on IR laser desorption should also be capable of producing vaporized proteins. However, a so far unsolved problem is that without prior separation of the different classes of biomolecules (lipids, peptides, proteins), only those that have the strongest charge affinity will be ionized, meaning that mostly lipids will be detected. While this can be at least partially mitigated by the introduction of washing steps, e.g. rinsing the sample surface with 70 to 80 % cold ethanol, a technique commonly used for the analysis of tissues [3], the use of more aggressive postionization steps seems to be so far indispensable for the analysis of proteins from complex mixtures.

2.6 Mass Spectrometry Imaging (MSI)

Mass spectrometry imaging (MSI) can be used to unveil spatial correlations between different molecular compounds within tissues or cells. This is essential to form an understanding of fundamental cellular processes, i.e. to discover the ”molecular map of the cell”, to perform pharmacokinetics with microscopic spatial resolution, and for probing biochemical heterogeneity on a single-cell level. While secondary ion mass spectrometry (SIMS) struggles

to extend its mass range much above 1 kDa, albeit at high spatial resolution in the 100 nm range [138], vacuum-MALDI and related ambient techniques have proven to be capable of producing analyte ions with molecular masses in the tens of kDa and with a spatial resolution down to 1 µm [139, 140]. MSI is most often performed in the microprobe mode, in which a small laser focus is rastered over the sample surface to produce a single mass spectrum from each position. The minimum achievable focus size is limited by the laser's wavelength λ, its beam quality M, and the numerical aperture NA of the focusing optics, and scales with $\propto M^2\lambda/NA$. To overcome this diffraction limit, some efforts have been made to develop near-field MSI, with recent results showing 250 nm spatial resolution at a mass of 221 Da [141]. Alternatively, in the microscope mode, a stigmatic ion image of the larger laser focus is projected onto a position sensitive detector using suitable ion optics, an approach used in the TRIFT [142] and MULTUM [143] instruments.

A number of reviews summarize the latest developments in this rapidly evolving field of research [3–6]. MSI is a label-free technique with high sensitivity and specificity and allows for the discovery of a wide range of biomolecules either directly from the tissue surface, or in combination with some of the aforementioned separation techniques. It is often performed in a multi-modal approach in which several techniques are combined in an order from least to most invasive, beginning with secondary ion mass spectrometry (SIMS), followed by washing and matrix deposition for matrix-enhanced SIMS, MALDI-TOF-MS, and AP-MALDI, and is typically followed by histological staining [3, 9]. Because rapid and reproducible matrix deposition continues to be a major hurdle in MALDI, and because matrix crystal size and surface diffusion resulting from solvent application practically limit the achievable mass resolution, IR-LDI MSI using endogenous water as a matrix is currently heavily researched [142, 144–146]. The use of IR lasers additionally benefits quantitation, as the large optical penetration depth usually leads to complete ablation of a sampled position, thus providing reproducible ablation volumes. Complete sample ablation also provides the possibility to improve spatial resolution through oversampling: by merely moving the laser focus by a fraction of its diameter between acquisitions, lateral resolution has been increased by factors of ≈ 4, although at lower sensitivity due to the reduction in ablated volume [5]. In addition, matrix-free desorption facilitates relatively simple switching between positive and negative polarity ion extraction, whereas only few MALDI matrices offer this option. Alternating the polarity between each sampled position yields more information about the imaged surface [6]. However, while the working mass range of UV-MALDI MSI reaches up to about 30 kDa, with some studies even showing detection of 100 kDa proteins [5], this performance is currently unmet by IR-LDI from tissue.

Chapter 3

Time-Resolved Imaging of Laser Ablation Plumes

This chapter is concerned with the investigation of PIRL ablation at atmospheric pressure by digital interference microscopy. It is based on two publications that came out as part of the research presented here [1, 2], but presents additional experiments and insights. Several people contributed considerably to the success of this project. The idea to implement this particular interferometry method was conceived by S. Kruber, who supervised K. Strahlendorff in setting up the initial version of the experiment as part of her master thesis. F. Tellkamp, head of our scientific support unit, supplied the LabView software framework and several modules for device communication. B. Reber implemented the Abel inversion algorithm in MATLAB as part of his internship. The micro-array chips were manufactured by Sercan Keskin. Our engineer J. Gonschior designed the sample holder for the chips, and D. Eggert measured the volume of the micro-droplets. Finally, A. Mostafa helped to modify the setup and perform preliminary experiments on these samples during his research stay.

The complexity of the laser ablation event and its convolution with the ion formation processes observed in LDI and MALDI requires the application of a variety of different techniques to form a coherent picture of the underlying physics. The influence of thermal and stress confinement on the ablation characteristics are of particular interest, as they are expected to bring about significant changes in the degree of vaporization, droplet generation, and plume velocity. As has been described in chapter 2, stress confinement conditions are expected to facilitate material ejection by purely mechanical forces and without significant vaporization in the low fluence regime, a process called spallation. At higher fluences, the material ejection is thought to be driven by a phase explosion similar to what is found for non-stress-confined conditions, but – because less energy is lost to mechanical relaxation – with higher pressures and an accordingly faster and more forward-peaked ejection and more efficient evaporative cooling.

A number of studies have investigated the wavelength and pulse length dependence on the material ejection. For example, larger laser fluences were shown to produce more homogeneous material depositions containing smaller particles in an experiment in which particles were produced under vacuum conditions and captured on a trapping plate [73]. In studies investigating the ablation process under atmospheric pressure, the photoacoustic stress waves produced during IR laser ablation from tissue [147] and from both DHB and glycerol [148] have been captured using piezoeletric sensors mounted below the sample. Increased material ejection was observed above a certain threshold fluence and ascribed to the onset of explosive boiling, i.e. a phase explosion. In yet another approach, the size distribution of droplets emitted from glycerol after IR irradiation with 5 ns laser pulses was investigated by the group of K. K. Murray at different wavelengths between 2.6 to 3.8 µm and laser fluences between 0.1 to 0.6 J/cm^2 using light scattering [149] and aerodynamic particle sizing [150]. The derived ablation threshold was shown to be very close to the ion detection threshold observed in other experiments. More particles were generally produced at larger fluences, and the average particle size was shown to be around 1 µm and to decrease with increasing fluence and absorptivity. At the largest absorptivity, which was controlled by adjusting the laser wavelength to the absorption maximum of glycerol, the particle diameter dropped sharply. While the authors discussed this observation in terms of a transition from a stress confined to a merely thermally confined regime, corresponding to an increase in laser penetration depth, the smaller average particle diameter could also be explained by an increase in vaporization due to the higher energy density throughout the ablation volume. Similar studies have also been performed for UV-MALDI by the same group [151,152]. There, a bimodal distribution of particle diameters was observed and attributed to the formation of a fine mist by sputtering of melted matrix and agglomeration of smaller evaporated particles and clusters on the one hand, and coarse particle ejection through matrix melting and spallation on the other hand. However, each of these approaches covers only part of the ablation event and cannot paint a complete picture of the underlying physics.

Photographic imaging methods have gained considerable popularity for the investigation of the ablation dynamics as their results are more directly accessible. Under laser breakdown conditions where plasma generation is a dominant process, fast photography of the spontaneous emission has been applied to the characterization of ablation plumes. This allowed for the study of the plasma shape as a function of fluence [153], spot size [154], and ambient pressure [155]. However, for the lower pulse energies commonly employed for soft ablation of biological samples in MALDI and related techniques, there is no strong optical emission. The addition of fluorescent markers to the sample has been used to provide information on the differences in angular spread of analyte and matrix molecules. A ”plume sharpening effect”,

describing a more forward-peaked expansion of heavier proteins compared to the matrix molecules, was reported for UV-MALDI [156], and significant variation of the expansion was observed between subsequent shots on the same sample location [157].

Most commonly, shadowgraphy, dark-field microscopy or Schlieren photography are used to image laser ablation plumes. These label-free methods show contrast based on changes in the refractive index and are thus suitable for the characterization of gas-phase material with low opacity. A comparison of different Schlieren techniques with very high image quality was performed by A. Vogel and coworkers [158]. However, these images give rise to certain ambiguities in interpretation as the recorded brightness is a measure of the refractive index gradient mixed with contributions from scattering and possibly fluorescence. In addition, many time resolved microscopy approaches require temporally incoherent illumination to avoid interference artifacts. Commonly, a multimode fiber is used to reduce temporal coherence of the illuminating laser pulse (e.g. in ref. [158]). This goes along with attenuation and temporal broadening of the pulse, and, depending on the source, very long fibers can be necessary to achieve sufficient incoherence. Alternatively, shorter fibers can be used if their mode-mixing properties are continuously changed, e.g. by shaking the fiber, or in combination with a rotating diffuser. Interference speckles can then be reduced by averaging a number of acquisitions, as has been shown recently for the optimization of the laser post-ionization of MALDI plumes [159].

On the contrary, holographic recording methods show contrast directly proportional to the object's optical path length and thus contain quantitative information about the three-dimensional refractive index distribution of the illuminated object [160]. They are therefore often used in biomedical [161] and solid-state applications [162] where otherwise transparent objects need to be imaged with high precision and sensitivity. Holography works very well with coherent laser sources and is thus ideally suited for nanosecond time resolved imaging. High optical contrast is achieved without the necessity of blocking portions of the laser beam, as is for example done in dark-field and Schlieren imaging where consequently very strong illumination is required. In addition, by using a double exposure scheme, noisy background can be subtracted while maintaining the absolute refractive index information.

Common to all holographic methods is the use of a reference wave front which is combined with the object wave front to obtain both amplitude and phase information of the light field. Having the additional phase information can often facilitate further improvements of the image quality and information content. In an extension of digital holography, extended-focus-imaging, recorded holograms can be digitally refocused to not only correct for a shifted or tilted focal plane, but to create a stack of refocused amplitude images at different distances from the real focal plane of the microscope objective, and to ultimately create a

three-dimensional representation of the object in question [163–165]. However, for successful application of this technique, the object needs to be opaque or its refractive index distribution needs to be known so that the topology can be inferred from the initial phase map. For this reason, it has so far only been applied to nontransparent or simple transparent objects with a constant refractive index, and not to complex refractive index distributions such as those found for laser ablation plumes. Three-dimensional representations of holographically recorded objects have also been acquired using tomography [166], but this requires recording the object from different projection angles, which is challenging given the turbulent nature and fast evolution of the hydrodynamics observed here.

In this chapter, time-resolved digital interference microscopy (DIM, also called holographic interference contrast microscopy) is employed to investigate the PIRL ablation of liquid water and glycerol under DIVE conditions. The first section is concerned with the plume expansion of the PIRL ablation from a large water droplet. In the second section, a new PIRL with higher pulse energy is employed. Plumes from water and glycerol are compared, and making use of the laser's high pulse energy, the role of spatial confinement against the substrate is investigated for the complete ablation of small droplets with only a single shot. Finally, the PIRL's suitability for laser-triggered sample delivery of micrometer sized particles is tested by ablating polystyrene beads from such picoliter volume droplets.

3.1 Digital Interference Microscopy

In digital interference microscopy (DIM), phase-contrast is achieved by converting the optical phase shift caused by an object into deviations from a pattern of interference fringes in the image. Digital image processing can then retrieve this phase information. The method is similar to digital holographic microscopy, in which a hologram is recorded instead of a focused image (i.e. the detector is placed outside of the objective's image plane), which is then digitally propagated into focus, and phase contrast microscopy, in which the phase difference between the object and reference wave is directly converted to intensity variations in the image without further image processing.

The high contrast for otherwise transparent objects makes such interferometry-based microscopy a method of choice for the characterization of ablation plumes. Both digital holography [167, 168] and DIM [169] have been used to study the free electron density distribution of breakdown plasmas created during the ablation of solid targets. However, absolute density calculations in this case are difficult unless several wavelengths are used or the free electron density is large enough ($>2 \times 10^{19}\,\mathrm{cm}^{-3}$) that the neutral density contribution to the refractive index can be neglected [170]. This will be further discussed

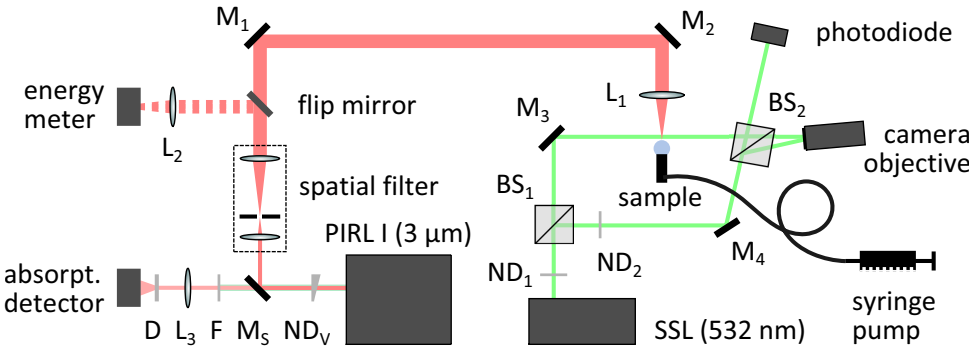

Figure 3.1: Beam paths for the picosecond infrared laser (PIRL I) used for ablation and the illuminating solid state laser (SSL). L_{1-3}: Calciumfluoride lenses, M_{1-4}: silver mirrors, BS_{1-2}: beam splitters, D: diffuser, F: bandpass filter, M_S: beam splitting mirror, ND_{1-2}: neutral density filters, ND_V: variable neutral density filter.

in section 3.2.3. But, under the assumption that the emanating shock-front is entirely composed of (neutral) ambient air [171] and that the plume is rotationally symmetric, the method can be used to compute a density map of the primary shock front generated during laser ablation under atmospheric pressure [169, 172, 173].

3.1.1 Description of the Microscope Setup

Various configurations and image reconstruction methods are known for DIM [160]. The imaging setup used here was simplified in comparison to what is found in the literature to only include a single long working distance microscope objective while still yielding sufficient spatial resolution. Recording the hologram in the microscope objective's image plane makes it particularly easy to monitor the sample and to perform any adjustments to the optics without the need for on-line image processing. The setup is schematically depicted in fig. 3.1: a diode-pumped passively Q-switched solid state laser (FDSS 532-Q, CryLas GmbH, Berlin, Germany) was used to produce green light pulses with a duration of 1.4 ns, short enough to prevent motion blurring within one image acquisition. The beam was split in an off-axis Mach-Zehnder configuration into a collimated object beam illuminating the sample, and a reference beam traveling a similar distance through open space. Both beams were recombined under an angle (at BS_2 in fig. 3.1) and a long working distance microscope objective with variable magnification (Optem Fusion, Qioptiq, Waltham, USA) was placed so that a sharp image of the object (the water splash following a laser ablation event) was formed on the monochrome CCD detector (DMK 23U274, The Imaging Source, Bremen, Germany, 1600 × 1200 pixels, 4.4 µm × 4.4 µm pixel size). Because both beams traversed the same objective, their wavefronts were intrinsically curvature matched (except for lens-aberrations). The narrow spectrum of the solid state illumination laser (SSL)

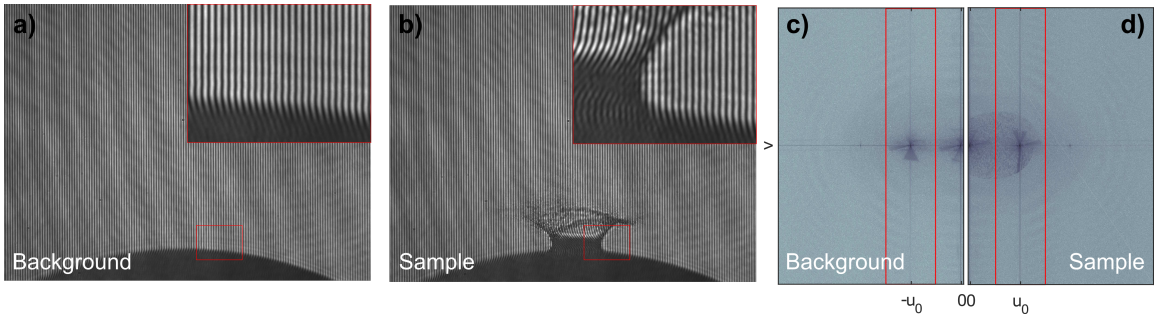

Figure 3.2: Method for background subtraction and phase reconstruction: a background (a) and a sample image (b) are taken before and after PIRL incidence, respectively. Insets show how the interference fringes curve due to differences in optical path length. c,d) Individually filtering both images in the Fourier domain yields the optical phase and amplitude of each image. The phases can then be subtracted to remove background noise.

ensured that its coherence length was sufficient for proper interference at the detector even with only roughly matched optical distances in the interferometer arms.

3.1.2 Phase Reconstruction

When no sample was introduced, the interference between the object and reference beam ideally produced a pattern of parallel and equidistant fringes on the detector. By changing the angle between the beams, the spacing and orientation of the fringe pattern could be adjusted. Introducing a sample into the object beam caused a change in curvature of the interference fringes. This is illustrated in the inset of fig. 3.2b, which shows a zoomed-in portion of an image where the straight fringes on the sides become distorted in the region of the ablation plume. The final image was reconstructed using the angular spectrum method [160, 174] and involved filtering the recorded intensity with a simple rectangular window in the Fourier-Domain. This shall be outlined in the following. The goal is to determine the phase shift

$$\varphi = \frac{2\pi}{\lambda} \int \Delta n(s)\, \mathrm{d}s \tag{3.1}$$

caused by a refractive index difference Δn along the light path S in the object beam with respect to the reference beam. Any remaining wavefront curvature not associated with the object can then be removed from the reconstructed phase by using a double exposure scheme [175, 176] in which an image of the unperturbed water surface is taken fractions of a second before the actual image of the laser impact. This background phase is then subtracted. Minimizing the delay between both acquisitions is beneficial to suppress movement of the water surface and changes in background phase (e.g. by convection).

The interferogram $I(x, y)$ measured in the detector plane is formed by the optical fields

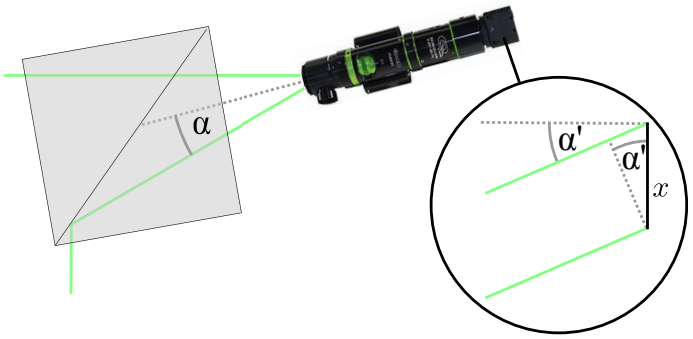

Figure 3.3: Sketch of the beam recombination angle α. Left: object and reference beam are recombined at a beamsplitter in front of the microscope objective. Right: the angle between them leads to a linear phase shift on the detector.

of the reference wave $R(x, y)$ and the object wave $O(x, y)$, and reads

$$I = |R|^2 + |O|^2 + R^*O + RO^* \,, \tag{3.2}$$

where the * denotes the complex conjugate. While the first two expressions in eq. (3.2) are known as the auto-correlation (or DC) term, the phase information is contained in the two latter expressions (AC terms), which describe the real and the twin image. If the object and reference beam, as illustrated in fig. 3.3, each have an angle α with respect to the microscope axis, which transforms into an angle α' towards the detector plane normal after passing through the microscope optics, the fields can be expressed as

$$R(x, y) = |R(x, y)| \exp\left[-i\left(\Omega_R(x, y) + \tfrac{1}{2}u_0 x\right)\right] \tag{3.3}$$

$$O(x, y) = |O(x, y)| \exp\left[-i\left(\Omega_O(x, y) - \tfrac{1}{2}u_0 x + \varphi(x, y)\right)\right] \,. \tag{3.4}$$

Here, u_0 depends on α' as discussed below, Ω_R, Ω_O are the phase shifts due to various optical aberrations or wavefront errors which can affect the object and the reference beam differently, and φ is the additional phase introduced by the sample. The phase shift resulting from the angle α' in the xz-plane is proportional to the distance x along the detector surface, and is modulated with a spatial frequency $u_0 = 2k \sin(\alpha)/M$, where $k = 2\pi/\lambda$ is the wavenumber of the illumination laser and M is the magnification of the microscope objective. This causes the fringe pattern

$$I(x, y) = |O(x, y)|^2 + |R(x, y)|^2 + 2A(x, y) \cos\left(\Delta\Omega(x, y) + \varphi(x, y) - u_0 x\right) , \tag{3.5}$$

where the abberations have been merged into a term $\Delta\Omega = \Omega_O - \Omega_R$. The angular dependency

of the modulation frequency can be quickly verified by realizing that the phase shift of each beam with respect to the detector normal is given by $k\sin(\alpha')$ (see again fig. 3.3), and by using the optical invariant $xn\sin(\alpha) = x'n'\sin(\alpha')$. Here, $n = n'$ is the refractive index of air, and x and x' are the object and image size, respectively. From this it follows that $\sin(\alpha') = \sin(\alpha)/M$ with $M = x'/x$. The resulting periodic intensity modulation along x in the plane of the recombination angle α can be split into a real and an imaginary part:

$$I(x,y) = I_0(x,y) + G(x,y) + G^*(x,y)\,, \tag{3.6}$$

where $A = |O||R|$ and $I_0 = |O|^2 + |R|^2$ are real, and $G = A\exp[-i(\Delta\Omega + \varphi - u_0 x)]$ is complex. Because of the off-axis configuration, the real and twin image can be separated from the DC term in the Fourier domain, where the real image's spectrum

$$\mathcal{F}_{u,v}(G) = \mathcal{F}_{u,v}\left(A\exp\left[-i\left(\Delta\Omega + \varphi\right)\right]\exp\left[iu_0 x\right]\right) \tag{3.7}$$

$$= \mathcal{F}_{u-u_0,v}\left(A\exp\left[-i\left(\Delta\Omega + \varphi\right)\right]\right) \tag{3.8}$$

is shifted by the fringe pattern's spatial frequency u_0. Under the assumption that this separation is large enough to fully separate the DC and AC terms, a simple rectangular Fourier window $H(u,v)$, which reduces the bandwidth to $u \in [\frac{1}{2}u_0, \frac{3}{2}u_0]$, retains only the real image information. By discarding everything else, the spectrum is centered according to $(u - u_0) \to u$. Figure 3.2c and d show typical spectra (logarithmic color scale) for the background and sample image with the Fourier window marked in red. In the implementation used here, the spatial frequency u_0 is determined automatically by the image processing script which picks the correct peak in the Fourier spectrum. After an inverse Fourier transform, the filtered intensity is

$$\bar{I} = \mathcal{F}^{-1}_{x,y}\left(H(u,v)\mathcal{F}_{u,v}\left(I(x,y)\right)\right) \tag{3.9}$$

$$= A(x,y)\exp\left[-i\left(\Delta\Omega(x,y) + \varphi(x,y)\right)\right]\,. \tag{3.10}$$

Thus, the object wave amplitude $|O|$ and phase shift φ can be determined as

$$|O| = |\bar{I}|/|R|\ \text{, and} \tag{3.11}$$

$$\varphi_{\mathrm{S}} = \varphi + \Delta\Omega(x,y) = \arctan\left(\frac{\mathrm{Im}(\bar{I})}{\mathrm{Re}(\bar{I})}\right)\,, \tag{3.12}$$

except for the reference wave amplitude $|R|$ and the aberration term $\Delta\Omega$. To compensate for image aberrations and detector defects, a background image I_{B} which shows the unperturbed

water surface is taken shortly before the laser desorption event for every sample image I_S. Two example images I_B and I_S are shown in fig. 3.2a and b. The background image contains the same reference wave R but an object wave O_B with a vanishing object phase $\varphi = 0$. The resulting background phase $\varphi_\mathrm{B} = \Delta\Omega(x, y)$ can then be subtracted from the sample phase φ_S to yield only the desired phase information [177]. The same is done for the reconstructed amplitude, such that the desired quantities are given by

$$\Delta|O| = |O_S| - |O_B| = \frac{1}{|R|}\left(|\bar{I}_S| - |\bar{I}_B|\right) \text{ , and} \tag{3.13}$$

$$\Delta\varphi = \varphi_S - \varphi_B \,, \tag{3.14}$$

where the reference amplitude is assumed to be $|R| = 1$. A two-dimensional phase unwrapping algorithm is applied to $\Delta\varphi$ to remove any 2π discontinuities from the reconstructed phase [178], and the phase is offset so that it is zero in the unperturbed regions in the top edge of the image.

The spatial resolution of the technique differs between the directions parallel and perpendicular to the interference fringes. In the former, the resolution is equal to that of the microscope objective (2.9 µm at maximum magnification setting), whereas in the latter it is determined by the interplay of magnification, pixel size and recombination angle α. Because both object and reference beam were chosen to traverse the same objective lens, the microscope objective's acceptance angle $\theta = \arcsin(\mathrm{NA})$ (with $\mathrm{NA} = 0.12$) limited the maximum recombination angle to $\alpha \leq \theta$. This in turn restricted the achievable spatial resolution: band-pass filtering in the Fourier domain removes all spatial frequencies larger than $u_\mathrm{max} = u_0/2$, where u_0 is the spatial frequency of the unperturbed fringe pattern. This reduces the resolution of the resulting phase map to be on the order of

$$\delta x = \frac{1}{u_\mathrm{max}} = \frac{M}{k \sin\alpha}, \tag{3.15}$$

which is the object size covered by two fringe periods $\Delta x = 1/u_0$. The largest α was achieved by aligning both beams symmetrically with respect to the objective, resulting in a fringe spacing of about 6 pixels or a $\delta x = 6\,\mu\mathrm{m}$. Usually a slightly larger fringe spacing of 7 to 8 pixels was chosen for better illumination, and a resolution of about $\delta x \approx 7.5\,\mu\mathrm{m}$ at a magnification of $M = 8.8$ was verified by imaging a resolution target (Thorlabs 1951 USAF Test Target). Signal quality was also limited by noise, which was in part due to an imperfect separation of the DC and AC spectra, and in part caused by changes in optical path length between the background and sample image, e.g. by vibrations or convection. As a measure of phase accuracy, the noise level was determined by calculating the standard deviation of

an unperturbed area of different background-subtracted phase images (compare ref. [179]), which yielded values of $\sigma < 0.018 \approx \pi/170$.

3.2 Picosecond Infrared Laser Desorption of a Water Surface

The experiments presented in this section aim to characterize the ablation dynamics under DIVE conditions. They include the determination of the ablation threshold, an estimate of the plume velocity as a function of fluence, and a comparison of the observed dynamics to similar IR-LDI experiments, in particular those performed by the group of A. Vogel with an Er:YAG laser with 70 ns pulse duration [180], and those recently published by our group in Toronto with a PIRL with a pulse duration of 100 ps [17, 112]. The sample geometry used here was very similar to that in the experiments performed by Y. Lu, in which the PIRL ablation plume generated from a small droplet was aspirated directly into an ion-trap mass analyzer [111]. The section also serves to demonstrate the imaging method's effectiveness for retrieving refractive index and density reconstructions of laser ablation plumes. To this end, a reconstruction of the shock front density from the recorded projections of the optical density was first achieved by using an implementation of the Abel-inversion and combining it with the Gladstone-Dale law as presented in section 3.2.4. As a comparison, the shock front density was also estimated from the plume expansion velocity. The time evolution of the primary shock front radii was fit using the Taylor-Sedov point explosion model [181–183] with a variable exponent, a model which is often applied to the plume expansion in laser ablation when the observed propagation distances are similar to the laser spot diameter [184–186]. As will be shown, the two methods give remarkably similar results except for the first 200 ns of plume expansion.

3.2.1 Laser Desorption and Pulse Energy Monitoring

Laser ablation was performed on a droplet of distilled water on top of a 100 µm inner diameter capillary. A stable, curved water surface was maintained by slowly replenishing the water using a syringe pump (New Era Pump Systems NE-1002X with Hamilton 25 µL #702). The surface position was held within 30 µm using feedback from the camera image to ensure stable focus conditions. Care had to be taken to not introduce any air bubbles into the system when loading the syringe.

The laser used here was the PIRL I (PIRL-APLQ-3000, Attodyne Inc., Canada), which emitted 10 ps pulses at 2.94 µm wavelength. The beam was spatially filtered and slightly expanded in a telescope assembly. A 50 mm focal length CaF_2 lens (L_1 in fig. 3.1) was used

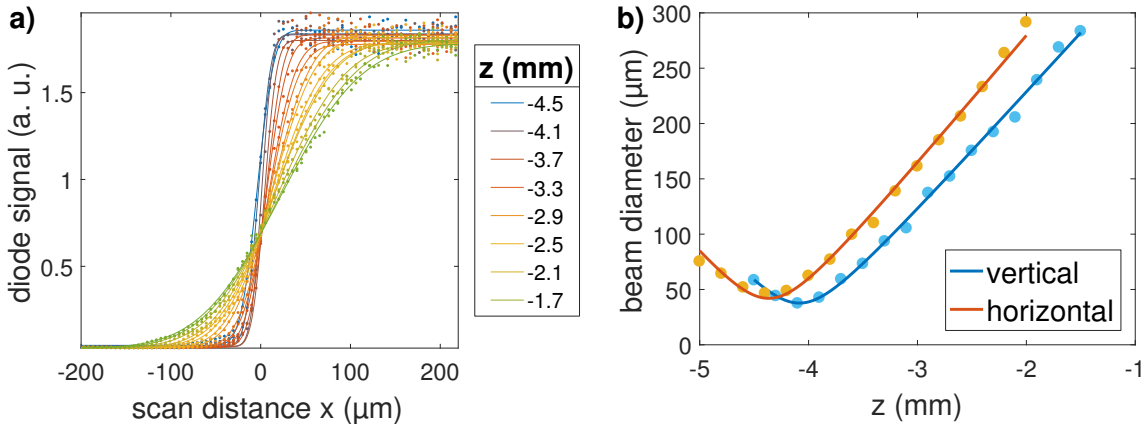

Figure 3.4: Knife edge measurements of the focus beam diameter. a) Scans at different distances z along the beam axis. b) Resulting beam diameter for each scan and the corresponding fits for the vertical (parallel) and horizontal (perpendicular) direction (with respect to the illumination laser beam axis).

to focus the light onto the sample under normal incidence, yielding a near-Gaussian, slightly elliptical spot with $1/e^2$ diameters of (43 ± 7) µm perpendicular and (38 ± 5) µm parallel to the illumination laser axis as determined by knife edge measurements. These measurements were performed with the same lens but at a position in the PIRL beam shortly before the last mirror. A razor blade was scanned through the beam using a set of translation stages, and the transmitted light was collected on an amplified photodetector (Thorlabs PDA20H). Figure 3.4a shows the photodetector's output voltage for scans of a knife edge along the direction parallel to the illumination laser beam. An equivalent dataset was recorded in perpendicular direction (not shown). The beam waists were extracted with a fit of the form

$$P = P_0 + \frac{P_{\max}}{2}\left[1 \pm \operatorname{erf}\left(\sqrt{2}\,\frac{x - x_0}{w}\right)\right], \tag{3.16}$$

where P is the diode voltage, w the Gaussian beam waist radius, and the $1/e^2$ diameters are given by $2w$. The diameters were then plotted as a function of the distance along the PIRL beam axis, as is shown in fig. 3.4b. Another fit of the form

$$w = w_0\sqrt{1 + \left(\frac{z - z_0}{z_R}\right)^2}, \tag{3.17}$$

where z_R is the Rayleigh length, yielded the minimum focus diameters stated above, and values of $M^2 = \pi w_0^2/\lambda z_R$ of 1.3 and 1.1 in perpendicular and parallel direction, respectively. The asymmetry stemmed from the PIRL's difference-frequency generation stage, which produced a beam profile resembling two individual but overlapping Gaussian profiles.

The peak fluence F in the focus center, a value stated throughout this chapter, was calculated according to

$$F = \frac{2E}{\pi w_a w_b}\,, \tag{3.18}$$

where E is the pulse energy, and w_a, w_b are the $1/e^2$ focus radii. The fluence was varied between $(0.16 \pm 0.06)\,\mathrm{J\,cm^{-2}}$ and $(4.7 \pm 1.0)\,\mathrm{J\,cm^{-2}}$ (corresponding to pulse energies between $(1.0 \pm 0.3)\,\mu\mathrm{J}$ and $(30.0 \pm 0.8)\,\mu\mathrm{J}$) using a variable neutral density filter at the laser output ($\mathrm{ND_V}$ in fig. 3.1). The stated standard errors stem from the power calibration procedure and the spot size uncertainty.

The PIRL pulse energy was monitored for each recorded image to reduce the influence of pulse energy fluctuations on data analysis. An absorptive detector (Thorlabs PDA20H-EC) was placed behind a 99:1 beam-splitting mirror ($\mathrm{M_S}$ in fig. 3.1) to cause only minimal losses to the main beam. This mirror was also dichroic in order to eliminate any residual pump light coming out of the PIRL's difference-frequency generation stage from the main beam which was used for ablation. In the transmitted beam which was used for pulse monitoring, a bandpass filter (F) blocked this light with wavelengths below 3 µm. Instead of being directly measured on the absorptive detector, the transmitted beam was focused onto a diffuser (D) in order to create a more homogeneous illumination, reducing the effect of shifts in beam position and angle. Before each measurement, the diode signal was calibrated to an energy meter (Coherent LabMax Top) by inserting a flip mirror into the beam at a position after the telescope assembly. The pulse energy fluctuations and the resulting diode signal were recorded for 1000 shots to yield a linear relationship between the two. The energy meter was itself calibrated to the output of a power meter (Thorlabs S314C) temporarily inserted after the focusing lens ($\mathrm{L_1}$), which measured the fraction of the light reaching the sample.

Timing synchronization of the illuminating SSL pulse and the camera shutter relative to the ablating PIRL was implemented with a picosecond-precision delay generator (SRS DG645). The laser was set to run continuously, firing at a repetition rate of 1 kHz, but the oscillator beam was blocked before entering the amplifier stage by a fast shutter (Uniblitz LS2-S2Z1-NL) placed inside the laser setup. The delay generator was set to trigger on the PIRL's trigger output to open the shutter to let a single pulse pass. Due to the long delay of the shutter, the passing pulse was the one following the one that triggered the delay generator. To account for the resulting timing jitter between the PIRL and the SSL, the exact delay between the two pulses was determined by capturing stray light from the PIRL's optical parametric amplifier (OPA) pump pulse (at 1 µm) and the part of the SSL reference beam that was transmitted at the second beam splitter ($\mathrm{BS_2}$) on separate fast photodiodes. The signals were recorded on an oscilloscope (Agilent DSO-X 3024A) and

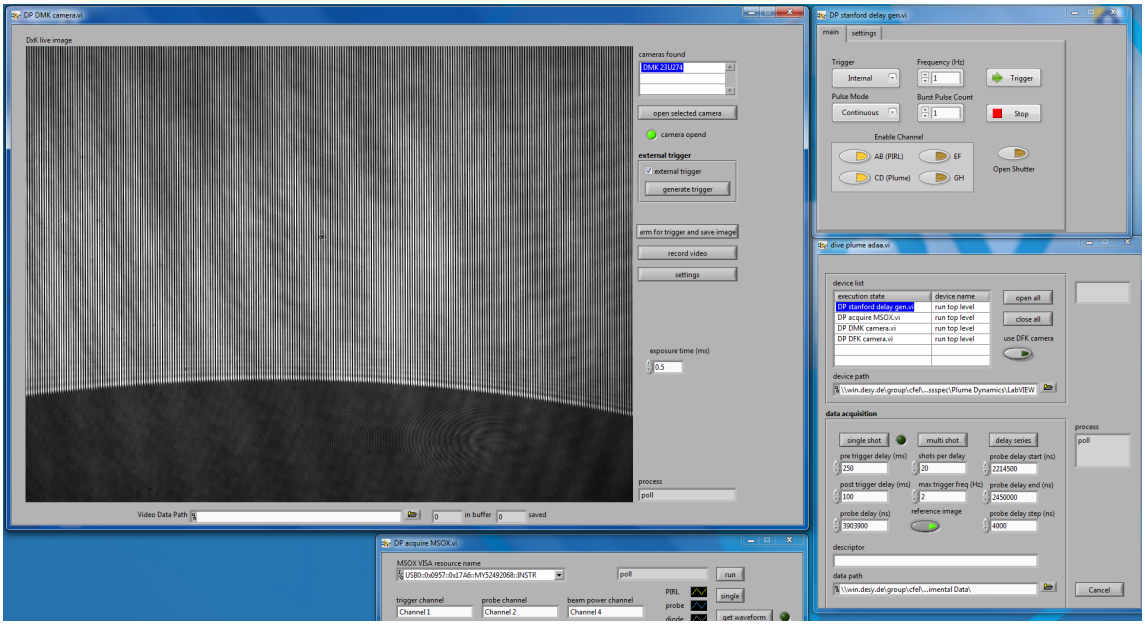

Figure 3.5: LabView user interface for the image acquisition. The module *DP DMK Camera* controlled the camera, the module *DP stanford delay gen* the delay generator (which triggered the shutter, camera and microchip laser), the module *DP acquire MSOX* read out the oscilloscope, and the module *dive plume adaa* was used as a master module to take several images at the same delay value or scan through a range of delay values. It also automatically recorded a background image before each ablation event.

saved on a computer using LabVIEW, yielding a timing precision on the order of the signal rise times (<2 ns). This mode of operation was chosen over directly triggering the camera and microchip laser from the PIRL pulse because these devices required about 100 µs lead time.

The software user interface implemented for the experiment is shown in fig. 3.5. It followed a modular design for each connected device, and a master module allowed for scanning through different settings. This way, devices could be switched out easily, and software modules could be re-used in other experiments.

3.2.2 Plume Dynamics

The description of the observed dynamics largely follows the one found in ref. [2]. Images of the plume expansion were acquired for laser peak fluences between 0.16 to 4.7 J cm^{-2}. FFT-filtering and background-subtraction were performed on each image pair to yield both the reconstructed amplitude and phase. The analysis of the collected phase images revealed three different ablation regimes, which is illustrated in fig. 3.6. At laser fluences below $F = 0.5\,\mathrm{J\,cm^{-2}}$ (3 µJ pulse energy), no disturbance of the water surface was observed. At

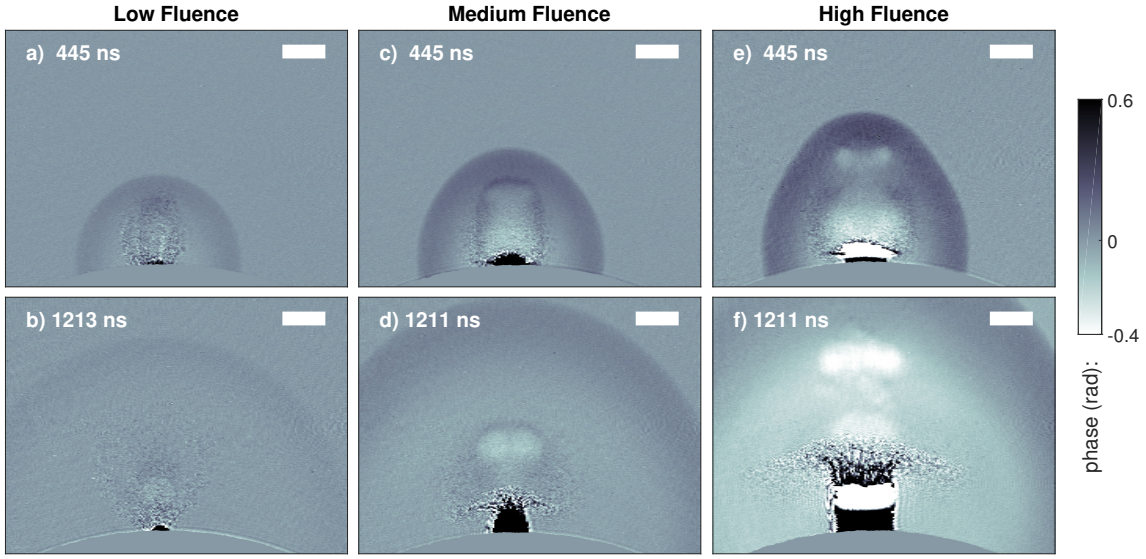

Figure 3.6: Reconstructed phase images showing different ablation regimes for low ($1\,\mathrm{J\,cm^{-2}}$), intermediate ($2\,\mathrm{J\,cm^{-2}}$), and high ($>3\,\mathrm{J\,cm^{-2}}$) laser fluence. Time stamps are relative to the time of laser incidence, scale bars indicate 100 µm.

fluences slightly above this ablation threshold, a hemispherical shock wave was observed to emanate from the location of laser impact at the water surface (fig. 3.6a and b). In accordance with previous studies, [186, 187] this primary shock wave (PSW) was identified as an acoustic wave resulting from a sudden compression of the ambient air as the heated water began to expand. Further inside the plume, a denser region containing the target material could be distinguished, the border of which was the contact front (CF). For low fluences, the region condensed into a cloud of water vapor and small droplets within the first 100 ns. At intermediate fluences (fig. 3.6c and d), the plume consisted of fewer droplets and instead showed a stronger contact front, indicating that a larger fraction of the ejected material reached the evaporation enthalpy. The plume expansion at the highest employed fluences (fig. 3.6e and f) was characterized by a turbulent propagation of the central part of the contact front. The higher the laser fluence, the larger was the ratio of initial velocities in normal and lateral direction, which did not only lead to a forward peaked propagation of the CF, but for high fluences also produced a PSW shape which was elongated along the propagation direction. For all fluences, a recoil-induced displacement of liquid water slowly expanded outwards directly above the water surface. It should be noted that the phase jumps in the regions of liquid water in fig. 3.6e and f are due to insufficient light transmission and/or a phase gradient that exceeded the system's resolution, and is thus an artifact of the imaging method. At later times (>1 µs, see fig. 3.6b, d, and f), a low-density region was observed inside the vapor/droplet cloud, constituting a rarefaction wave following the explosive ablation.

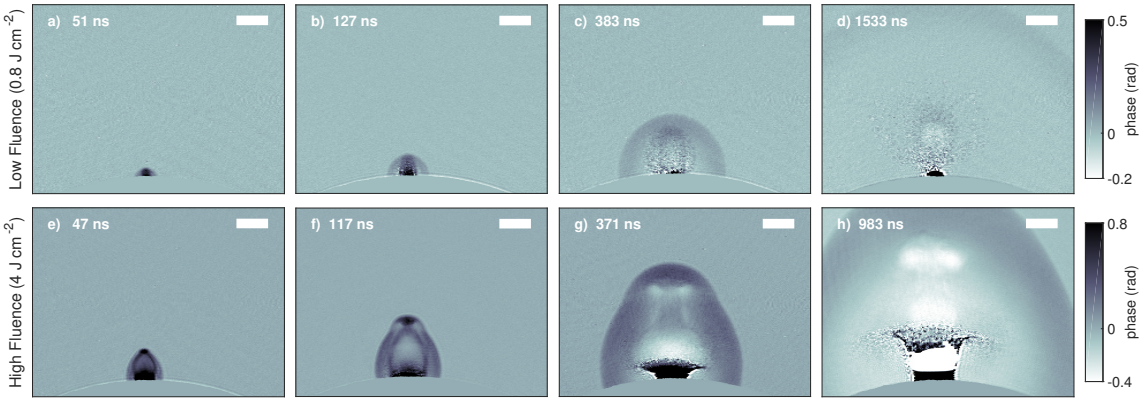

Figure 3.7: Reconstructed phase images of the early stage plume expansion for the low (a-d, 0.8 J cm^{-2} / 5 µJ) and high (e-h, 3.9 J cm^{-2} / 25 µJ) fluence regime. Time stamps are relative to the time of laser incidence, scale bars indicate 100 µm.

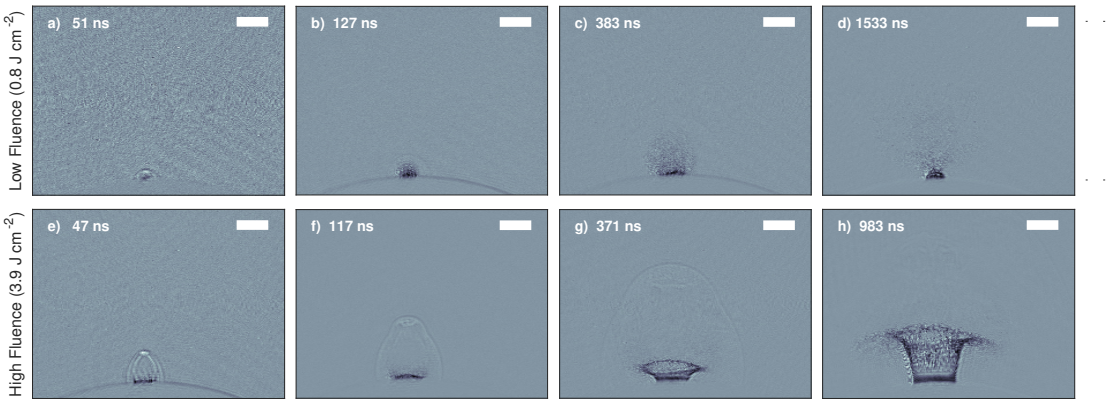

Figure 3.8: Reconstructed amplitude images of the early stage plume expansion for the low (a-d, 0.8 J cm^{-2} / 5 µJ) and high (e-h, 3.9 J cm^{-2} / 25 µJ) fluence regime. Time stamps are relative to the time of laser incidence, scale bars indicate 100 µm.

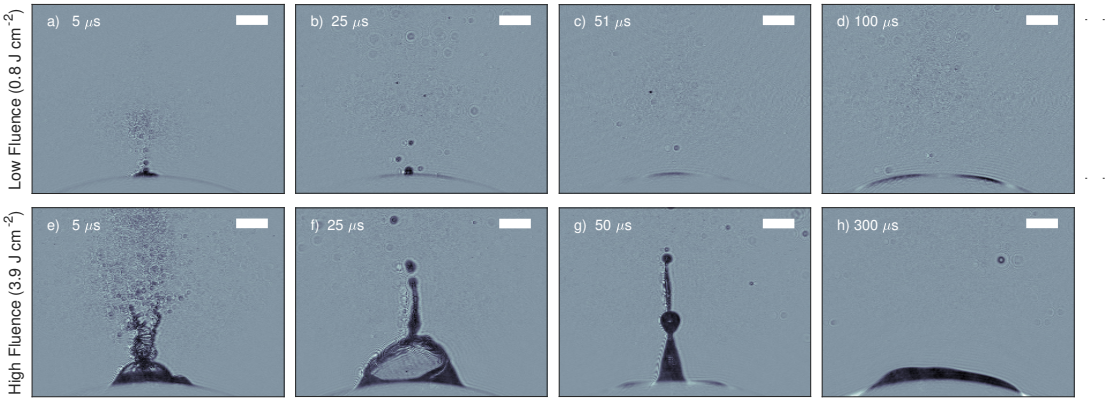

Figure 3.9: Reconstructed amplitude images of the plume expansion at later times for the low (a-d, $0.8\,\mathrm{J\,cm^{-2}}$ / $5\,\mu\mathrm{J}$) and high (e-h, $3.9\,\mathrm{J\,cm^{-2}}$ / $25\,\mu\mathrm{J}$) fluence regime. Time stamps are relative to the time of laser incidence, scale bars indicate $100\,\mu\mathrm{m}$.

Figure 3.7 and fig. 3.8 show the time evolution of the expansion for high and low fluence by means of the reconstructed phase and amplitude data, respectively. While for low fluences a high (optical) density region at the top of the plume, i.e. between PSW and CF, dissipated quickly, this region was well visible and not separating from the PSW front for the first few hundred ns for intermediate fluences. Its rapid movement typically created two ring-vortices and a turbulent updraft of water vapor in its wake. For the highest fluences the high-density region protruded outwards, distorting the PSW's shape and making it more elliptical in nature. The threshold for the formation of this plume shape was observed to fluctuate around 2.5 to $3.6\,\mathrm{J\,cm^{-2}}$. In the reconstructed amplitude images, the contrast of the gas-phase portions of the plume was lower than for the phase images. However, they serve well to identify the liquid-phase portions of the plume. A region of faint positive amplitude change was visible behind each shock front due to a strong lensing effect produced by the variation in refractive index, similar to what is observed in shadowgraphy. This was especially pronounced for the high density region at the top of the plume.

Figure 3.9 shows the ablation dynamics on a longer, microsecond timescale for the high ($\approx 3.90\,\mathrm{J\,cm^{-2}}$ / $25\,\mu\mathrm{J}$) and low ($\approx 0.78\,\mathrm{J\,cm^{-2}}$ / $5\,\mu\mathrm{J}$) laser fluence regime. At these delays, the primary shock front was no longer in the field of view, and the dynamics were fully comprised of droplet and water surface movement. An accurate phase determination was difficult for liquid material, as is evidenced by the aforementioned artifacts in fig. 3.6e and f and also in 3.7h. Therefore, only the reconstructed amplitudes (i.e. the background-subtracted absolute value of the FFT filtered interference pattern) are shown here. For high fluence, the initial water column that is visible at $1\,\mu\mathrm{s}$ in fig. 3.7h contracted due to under-pressure and surface tension as it propagated away from the water surface, and it

moved slower than the surrounding cloud of droplets. A second cavitation bubble formed at its base, as shown in fig. 3.9e, similarly contracting to form another liquid water column. At around 300 µs no further expulsion of material was observed, although the water surface still showed slight oscillations. For low fluence, the amount of ejected material was much smaller, and thus less recoil occurred. The water column was less pronounced or even absent and the desorption event subsided much faster (50 µs at 5 µJ).

Some amount of blurring due to out-of-focus portions of the plume was expected given that the microscope objective's depth of field was only around 40 µm. This was especially noticeable for ejected droplets visible at later time delays, which showed distinct diffraction rings. The spatial resolution for the outermost part of the plume, however, was not significantly altered because, due to its spherical shape, the plume front did not extend far beyond the focal plane in these regions. Spatial resolution was thus mainly affected in the center of the ablation plumes where the extension perpendicular to the focal plane was large.

The experiments presented in this section were conducted with a smaller laser focus (40 µm) and a smaller field of view (800 µm × 600 µm) than most comparable studies. Because less material was removed per shot, recoil ejection was reduced and the duration of the ablation event was much shorter. For example, for the IR ablation of water with 70 ns Er:YAG pulses at 2.8 J cm^{-2} peak fluence with a 1 mm focal diameter, the authors observed material ejection up until almost one second [188]. On the other hand, the initial material ejection observed here using the PIRL proceeded on a faster time scale than previous studies. As described by Apitz *et al.* [188], a fine mist of droplets is produced by a phase explosion of the superheated surface layer. Because in the present work, the energy was deposited impulsively under DIVE conditions, the process happened more rapidly, so that the PSW and the front of the droplet cloud were initially not distinguishable in the acquired images. The propagation of gas-phase material became apparent for intermediate fluences for which a clear contact front formed. Such a contact front can only develop once the volumetric energy density of the superheated liquid is sufficiently close to the vaporization enthalpy under ambient conditions for a significant amount of vapor to form.

Studies employing shorter pulse durations in the low nanosecond regime, i.e. at near stress confinement conditions, have mostly reproduced the findings of Apitz *et al.* [188], with the most prominent features being the turbulence and subsequent jet emission in the high-fluence range [189] and a non-turbulent emission comprised mostly of droplets at low fluences [190, 191]. However, none of the cited studies demonstrated the forward peaked ejection of a high density region fast enough to disturb the PSW front, although a reason might be that the low contrast of the published images makes it impossible to resolve the primary shock-wave. This unfortunately hampers a direct comparison of the

PSW's protrusion observed in the present study. On the other hand, the observations made here are very similar to the results of a dark-field study of DIVE with 100 ps pulse duration (compared to 10 ps in the present study) at fluences between 0.22 and 0.83 J cm^{-2} and 200 µm spot diameter which was conducted by Franjic *et al.* [17], demonstrating that the high-density region is an effect generally observed for PIRL ablation of water and not an artifact of the particular implementation of the technique.

3.2.3 Plasma Threshold

The cause for the observed differences compared to nanosecond ablation are not necessarily clear, but might be due to the higher laser irradiance. A similar but more pronounced fast expansion of the central plume, which tends to form a triangular primary shock front, is seen for the laser ablation of metals with femtosecond pulses because of the optical breakdown of the ambient air in the focal region and the formation of a plasma filament [192]. For longer pulses, plasma formation due to multiphoton absorption becomes less significant, but a plasma can still form due to cascading ionization if sufficient seed charges are created. We calculated a maximum peak irradiance of 5×10^{11} W cm^{-2} at the center of the laser focus, which would be sufficient to initiate avalanche ionization and to ultimately lead to plasma formation at visible and near-infrared wavelengths [98], but not necessarily at mid-IR wavelengths where the photon energies are small.

To check the influence of avalanche ionization, the model described by Noack and Vogel [193] was implemented in Matlab and the parameters adjusted to those used in the present experiments. It consists of a set of rate equations for multiphoton ionization, cascade ionization, electron diffusion and electron recombination. Figure 3.10 shows a reproduction of the results shown by that study, demonstrating that the implementation was correct. The solid lines plot the simulated free electron density as a function of time (normalized to the pulse duration) for different pulse durations and wavelengths. The free electron density initially grows slowly by multiphoton ionization, essentially tracking the temporal profile of the laser pulse. However, avalanche ionization sets in as soon as the first electron is generated in the focal volume, resulting in a much stronger growth of the free electron population once a threshold is reached. This limit is hard-coded into the algorithm which only considers avalanche ionization once there is a 50 % probability of encountering an electron in the laser focal volume. The results without avalanche ionization are plotted as dashed orange lines, whereas the full simulation produces the blue curves.

The critical electron density characteristic of an optical breakdown can be estimated to be around 10^{18} to 10^{20} cm^{-3}, and a value of 10^{20} cm^{-3} was used by Noack and Vogel. They note

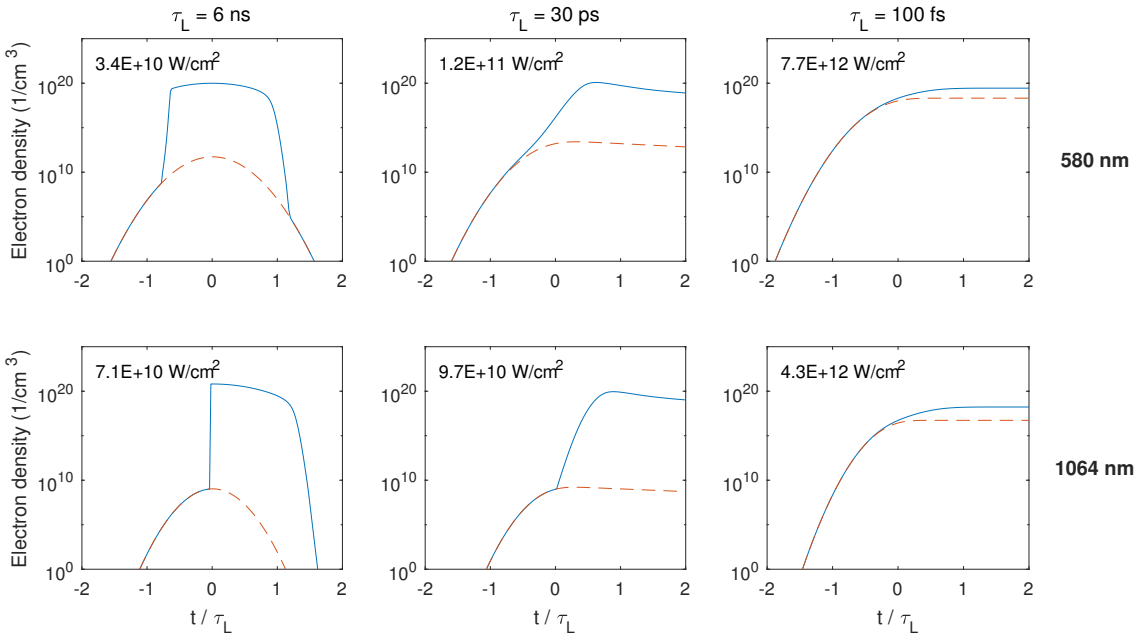

Figure 3.10: Evolution of the free electron density at breakdown threshold for different pulse durations (left to right) and wavelengths (top to bottom) reproduced from Noack and Vogel [193]. The respective threshold irradiance is indicated in the top left of each panel. The concentration due to multiphoton absorption alone is plotted as a dashed orange line. The time axis is normalized to the laser pulse duration τ_L.

that while multiphoton ionization dominates at high photon energies, the avalanche ionization rate increases towards longer wavelengths, ultimately causing lower threshold irradiances for the irradiation with 1064 nm. The interplay between multiphoton and avalanche ionization is also strongly affected by the pulse duration: while for 100 fs pulses, the free electron yield is almost entirely due to multiphoton ionization (the red and blue curves almost overlap in the right column of fig. 3.10), this pathway becomes less significant for longer pulses with similar pulse energy and, consequently, lower peak irradiance. Instead, avalanche ionization becomes stronger the longer the electrons are accelerated in the optical electric field. However, for long pulses, creation of the initial electron to start off the avalanche can be the limiting factor for ionization. For this reason, an initial free electron population which emulates impurities can be introduced into the simulation to better accommodate experimental results [193, 194].

Figure 3.11 shows the results for PIRL irradiation of a water surface. In a), the irradiation parameters are set to those of PIRL I in the experiment described here. The settings for b) reflect the conditions used by Franjic and Miller [17]. This is summarized in table 3.1. For PIRL I, the blue curve shows the free electron density evolution at threshold irradiance, which corresponds to 30.5 µJ, slightly higher than the largest pulse energy used in the

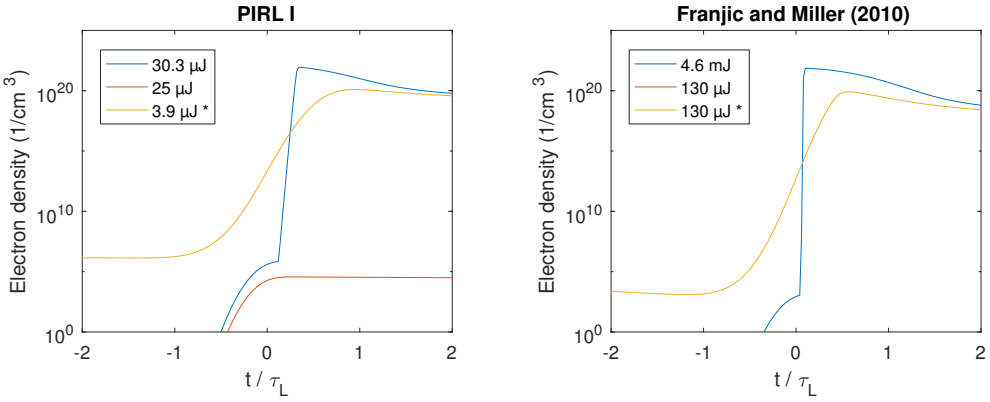

(a) **(b)**

Figure 3.11: Evolution of the free electron density for a) PIRL I ($\tau_L = 10\,\mathrm{ps}$) and b) the laser parameters used by Franjic and Miller [17] ($\tau_L = 105\,\mathrm{ps}$). The blue curve is the result for the threshold irradiance, the orange curve for the high fluence regime found in the experiment, and for the yellow curve (and indicated by a *) an initial free electron density equal to one electron within the laser focal volume was included. The yellow curve in a) is at threshold (maximum free electron density $\varrho_{e,\max} = 1 \times 10^{20}\,\mathrm{cm}^{-3}$), whereas in b), the free electron density reaches $\varrho_{e,\max} = 7 \times 10^{19}\,\mathrm{cm}^{-3}$. The orange curve in b) lies below 1 and is thus not visible.

Symbol	PIRL I	F. & M.	Description
λ	2940 nm	2940 nm	Laser wavelength
τ_L	10 ps	105 ps	Laser pulse duration
ω_0	20 µm	100 µm	Laser Gaussian beam radius
n	1.274	1.274	Water refractive index
ΔE	6.5 eV		Water effective band gap
η_{rec}	$2 \times 10^{-9}\,\mathrm{cm}^3/\mathrm{s}$		Electron recombination rate
τ_C	1 fs		Time between electron-heavy particle collisions

Table 3.1: Relevant parameters used for the computation of the plasma threshold according to [193]. The center left column contains the settings reflecting the experiments conducted here, the center right column those for the experiments performed by Franjic and Miller.

experiment. The red curve illustrates that there is no significant generation of free electrons at a typical value for the high-fluence regime. However, if an initial free electron density corresponding to one electron within the laser focal volume $\pi\omega_0^2 z_R$ is introduced (where $z_R = \pi\omega_0^2/(\lambda/n)$ is the Rayleigh length), the plasma threshold appears at a much lower pulse energy of only 3.9 µJ. This is even below the ablation threshold, and thus unlikely to be a real effect. While an initial free electron density is known to be important to simulate the plasma threshold for wavelengths up to the near-IR [194], it in that case emulates impurities which considerably lower the effective band-gap / ionization potential of the surrounding medium. However, the relevance of these impurities decreases with increasing wavelengths because only a decreasing fraction of them will have a sufficiently low ionization potential to be overcome by IR photons, and it can be assumed that mid-IR radiation is not energetic enough to justify a significant initial free electron density in the simulation.

A similar effect is observed for the parameters reflecting the experiments of Franjic and Miller. The blue curve in fig. 3.11b again shows the free electron density evolution at threshold irradiance without an initial free electron density. Because multiphoton ionization is inefficient for the long pulse duration, the irradiance threshold is considerably higher than what was used in the experiments. This is why the electron density for the maximum experimental pulse energy, plotted in red, stays far below the shown axis limits. The situation again changes when an initial free electron density is introduced. In this case, the yellow curve shows a maximum at $7 \times 10^{19}\,\mathrm{cm}^{-3}$, only slightly below the (somewhat ill-defined) plasma threshold of $10^{20}\,\mathrm{cm}^{-3}$. As was pointed out, the introduction of such an initial value seems questionable, but plasma generation by avalanche ionization can not be fully ruled out. Thermal ionization could for example be a relevant pathway for initial free electron production.

Laser breakdown under ambient conditions for long pulse durations can also be discussed in the framework of laser absorption waves [195]. Similar plume shapes have been observed for the near-IR ablation of metals and polymers with nanosecond lasers and attributed to a laser-supported detonation or laser-supported combustion wave, in which the initial part of the laser pulse creates free charges, for example by thermal ionization behind the emerging supersonic shock wave, which then absorb the later parts of the pulse [196, 197]. However, these models predict the generation of a hot plasma, and no plasma spark was observed by eye even for kilohertz operation of the laser system, just as no plasma spark was observed in a previous study [198] with similar ablation conditions (2.92 µm wavelength, 19 ps pulse duration, 30 µm spot diameter) even at a higher peak irradiance of $3.4 \times 10^{12}\,\mathrm{W\,cm}^{-2}$ (peak fluence of $65\,\mathrm{J\,cm}^{-2}$). Although thermal ionization of the leading portion of the plume is possible in the present study, we do not observe a significant contribution of the free

charge density to the shock front's optical density. If present, free electrons give a negative contribution of approximately $-N_e/2N_c$ to the refractive index, where N_e is the electron density and $N_c \approx 4 \times 10^{21}\,\mathrm{cm}^{-3}$ is the critical density corresponding to a plasma frequency equal to the illumination laser frequency [169, 170]. A significant reduction of the phase shift corresponding to a 10 % change in refractivity should be observed in the experiment for densities above $2 \times 10^{17}\,\mathrm{cm}^{-3}$. The protrusion of the PSW is seen as an optically dense region, indicating that the density of free electrons is far below the critical value for plasma generation of $N_e \approx 10^{18}$–$10^{21}\,\mathrm{cm}^{-3}$ for all recorded images [193].

3.2.4 Three-Dimensional Reconstruction and Density Maps

The phase images $\varphi(x, y)$ obtained using DIM permit the recovery of the refractive index distribution and ultimately the density distribution in the object beam. However, because the images acquired in DIM represent a two-dimensional projection of a three-dimensional object, the recovery of the 3D distribution is non-trivial. One way to approach the loss of depth-information is to assume a cylindrical symmetry of the object. This is well-justified in the case of laser-ablation plumes from a surface with the same symmetry, such as the locally flat droplet surface observed in the experiments described here. With the y-axis being the axis of symmetry, one can thus write

$$\varphi(x, y) = \frac{4\pi}{\lambda} \int_{|x|}^{\infty} \frac{r\,\Delta n(r, y)}{\sqrt{r^2 - x^2}}\,\mathrm{d}r\,. \tag{3.19}$$

The inversion of eq. (3.19) is a well known problem referred to as the inverse Abel transformation. The Gaussian basis-set expansion method [199], which is commonly employed to analyze velocity map imaging data, was chosen as the inversion algorithm. It is designed to reproduce the sharpest features, have a large dynamic range, and handle noise well without introducing spurious artifacts. The corresponding section of the pyabel python package [200] was implemented in Matlab and thoroughly tested against the original algorithm before use.

The Gladstone-Dale relation $(n - 1)/\rho = R$, where R is the specific refractivity, was used to determine the density in the primary shock front from its refractive index [201]. The relative density of the compressed ambient air can be calculated as

$$\frac{\rho(x, y)}{\rho_0} = 1 + \frac{\Delta n(x, y)}{n_0 - 1}\,. \tag{3.20}$$

The ambient refractivity $(n_0 - 1) = 277 \times 10^{-6}$ was determined based on the updated Edlén equation [202] and values of air pressure, temperature, humidity and CO_2 content on the day

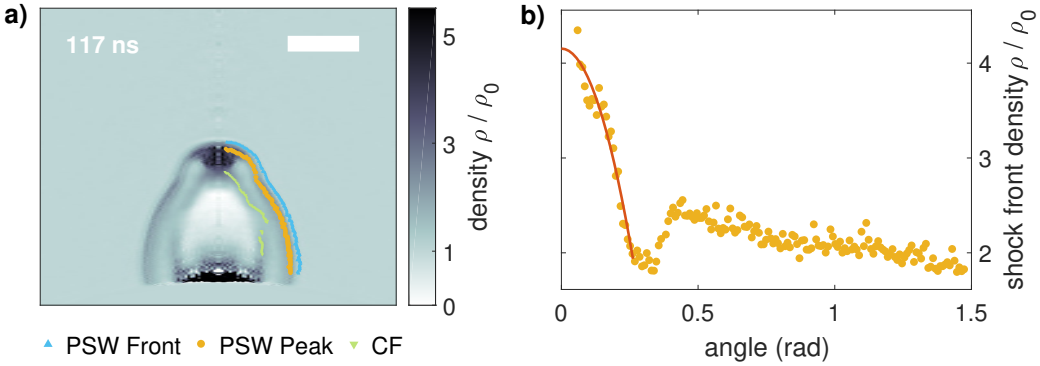

Figure 3.12: Density reconstruction of the PSW in units of the ambient air density ρ_0. a) Density reconstruction of data shown in fig. 3.7f. The image is symmetric. The right side shows the positions of the start of the PSW (blue), the peak of the PSW (orange), and the start of the CF (green) as identified by a Matlab script. b) Density at peak of the PSW as a function of angle from the surface normal. A quadratic, symmetric fit is applied to extrapolate the density at zero angle (orange line).

of the experiment. The Gladstone-Dale relation stays (approximately) valid independent of temperature unless significant electronic excitation or molecular dissociation of the gas appear, so that the interferometric determination of the density can be performed for shock front temperatures as high as 5000 K or Mach numbers of 22 [203].

Fig. 3.12 shows a density map based on the data shown in fig. 3.7f. In order to reduce noise, the left and right side of each phase image was averaged and slightly smoothed using a 5 µm × 18 µm Wiener filter before the Abel inversion was performed. The density map is thus symmetric. The contrast between high- and low-density regions inside the plume is considerably better than in the projected phase image, which simplifies subsequent image processing. Three distinct regions of the plume were identified for each recorded image using a custom Matlab image processing script. The regions are marked in the right half of fig. 3.12a. The rising front of the PSW was found by simple thresholding along radial paths pointing towards the point of laser incidence (blue). Based on this position, the peak of the PSW could be located (orange). Identifying the CF by thresholding was difficult due to its complex shape, which was often granular and ill-defined. It was thus only performed in near-normal direction and for a limited time range. The density along the PSW front (orange curve) is shown in fig. 3.12b as a function of angle from the surface normal. The pressure in the normal direction was found to be very high, which can be attributed to the overlap between the PSW front with the high density region separating from the contact front. To the side of this region (angle ≈ 0.4 rad), the pressure dropped by a factor of two as the lateral velocity of the bulge was much lower, leading to a much fainter pileup of ambient air. The pressure rise for larger angles resembled the PSW front of the hemispherical shock,

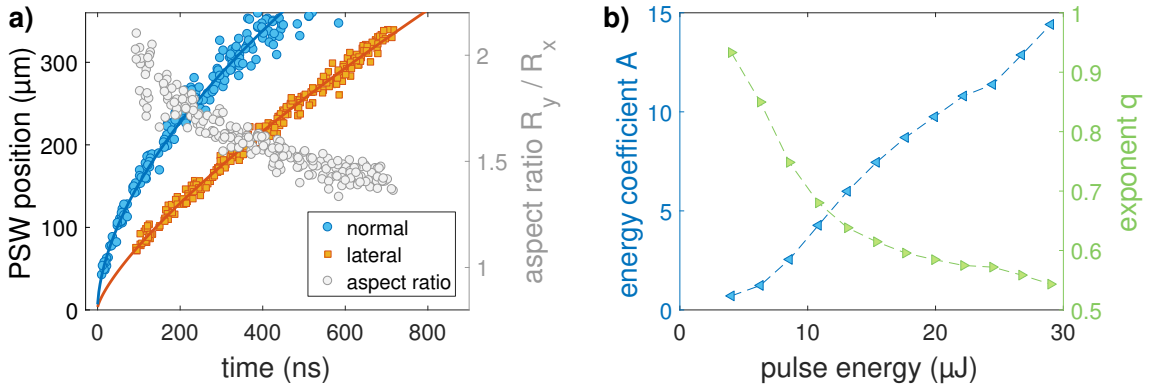

Figure 3.13: Fitting the PSW expansion with the Taylor-Sedov model. a) Fit for both normal and lateral expansion direction at 22 µJ pulse energy. The aspect ratio between the normal and lateral extent of the shockwave is plotted in grey. b) Fit coefficients A (triangles pointing left, blue), and q (triangles pointing right, green) as a function of pulse energy.

which again expanded with high velocity in the normal direction. The overlaid curve in fig. 3.12b is a quadratic fit to extrapolate the density in the normal direction, which could not be directly obtained because of the center-line noise resulting from the Abel-inversion. A quadratic fit was chosen as an approximation of the real angular density profile, which reflected the forward peaked elliptic expansion velocity profile.

3.2.5 Blast-Wave Model

Taylor-Sedov (TS) blast wave theory [181] is commonly employed to model the plume expansion and extract a conversion efficiency from laser pulse energy to shock-wave-energy [187, 189, 204]. It models the radius of a (hemi-)spherical shock wave as a function of time under the assumption that the blast energy is deposited instantaneously and in a point source, that the mass of the swept up air is much greater than that of the ablated material, and that the shock front pressure p_s is much higher than the ambient pressure ($p_s/p_0 > 10$). In an extension of the model to arbitrary dimensionalities, namely planar, cylindrical and spherical shock waves ($\nu = 1, 2, 3$ respectively) [183], the shock front radius R may be written as

$$R(t) = \xi_\nu \left(\frac{E_0}{\rho_0}\right)^{\frac{1}{\nu+2}} t^{\frac{2}{\nu+2}}, \tag{3.21}$$

where ξ_ν is a constant depending only on the specific heat ratio γ and the dimensionality ν, E_0 is the released energy, ρ_0 is the ambient density, and t is the time. The PSW front radii were extracted from the density maps using the Matlab image processing script mentioned previously. The rising front (blue curve in fig. 3.12a) was used as a position marker as it was

identified most reliably and showed no significant difference to the PSW peak position. The CF position will not be further discussed for now as it could only be reliably extracted for the high fluence regime. The primary shock front positions in normal and lateral directions with respect to the center point on the water surface were fitted with the TS model in the form $R(t) = A(t - t_0)^q$, with two fit parameters A and q for each dataset and a global offset in delay time t_0 determined by a cumulative fit of the PSW positions in normal direction. Figure 3.13a shows an exemplary fit for a pulse energy of 22 µJ. High pressure gradients across the water surface caused a fast initial expansion in normal direction, while at later times the expansion was almost spherical, as is indicated by the decrease of the aspect ratio over time plotted on the right ordinate of fig. 3.13a. The results of the TS model for different fluences for the expansion in normal direction are shown in fig. 3.13b. The energy coefficient A showed a linear increase with fluence and was thus, in conflict with the earlier observations, not an indication of a transition in ablation mechanism. The fitted exponent q decreased from an almost linear plume expansion $R \propto t$ at low fluences to an expansion with cylindrical shock-wave-character ($\nu = 0.5$) at high fluences. Although the coefficient A did not show any transition, the data for q indicated two regimes. For low pulse energies, the exponent decreased strongly with rising pulse energy, while the slope was much less for energies above ≈15 µJ, which was close to the energy at which a significant PSW protrusion became visible. The results for the lateral expansion (not shown) conveyed similar trends for A and q, but were more noisy and less distinctive.

Because the exponent q was used as a fit parameter, the coefficient A held no quantitative information and the mechanical energy E_0 released in the shock could not be determined [186]. The adaption of the exponent was necessary, however, because the laser ablation plume changed its shape from planar to elongated along the surface normal, and only became spherical at later times, which did not fulfill the requirements of the TS model. Nonetheless, the adapted model fitted the shock front positions very well, and thus served to extract the instantaneous shock front velocities. These are shown in fig. 3.14a for different pulse energies and compared to the speed of sound marked by a red line. The plume front strongly decelerated in the first few hundred ns and reached Mach 1 at around 1 µs for all fluences shown. Because of the strong deceleration, it was difficult to assign an initial velocity, which would critically depend on the measurement's time resolution.

Using the velocity data, the temperature T_s of the compressed background gas could be estimated by using the Rankine-Hugoniot jump conditions and by treating air as an ideal

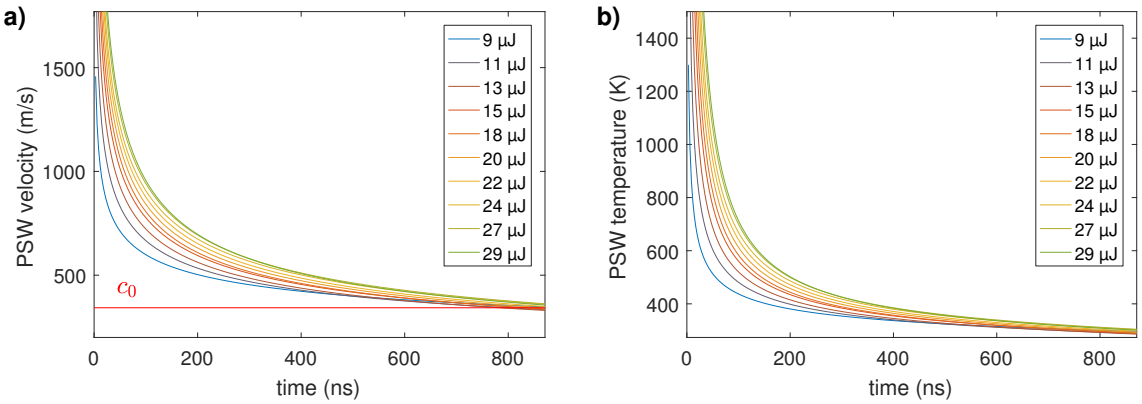

Figure 3.14: Shock front velocity analysis via the Taylor sedov model. a) PSW velocities in normal direction resulting from the Taylor-Sedov fits for different pulse energies. The red line indicates the speed of sound in ambient air c_0. b) Derived temperature values according to eq. (3.22).

gas with constant heat capacity [205]. It scales with the shock wave velocity u_s as

$$\frac{T_s}{T_0} = \frac{(M_s^2 + 5)\,(7M_s^2 - 1)}{36M_s^2}\,, \tag{3.22}$$

where T_0 is the ambient temperature, $M_s = (u_s/c_0)$ is the shock wave's Mach number, c_0 is the speed of sound in the ambient air, and $\gamma = 1.4$ is the ratio of the constant volume and constant pressure heat capacity for an ideal gas. The estimated shock front temperatures are shown in fig. 3.14b. After 100 ns, corresponding to the images shown in fig. 3.7b and f, the values for the high and low fluence regime ($0.8\,\mathrm{J\,cm^{-2}}$ / $3.9\,\mathrm{J\,cm^{-2}}$) read 680 K and 380 K, respectively.

3.2.6 Comparison of the two Methods and Conclusion

Knowledge of the shock front velocity u_s also facilitates the calculation of the shock front density ρ_s [205], making it possible to compare this data to the values obtained through Abel inversion of the phase information. Again assuming an ideal and calorically perfect gas, the velocity dependence of the density reads

$$\frac{\rho_s}{\rho_0} = \frac{6M_s^2}{5 + M_s^2}\,. \tag{3.23}$$

The resulting evolution of the PSW front density is shown in fig. 3.15 as a series of line plots for different pulse energies. For delay times >200 ns, they overlap very well with the results from the density maps, plotted as scatter plots for a high and a low pulse energy. For shorter delays, the density maps show very high values up to 10 times the ambient

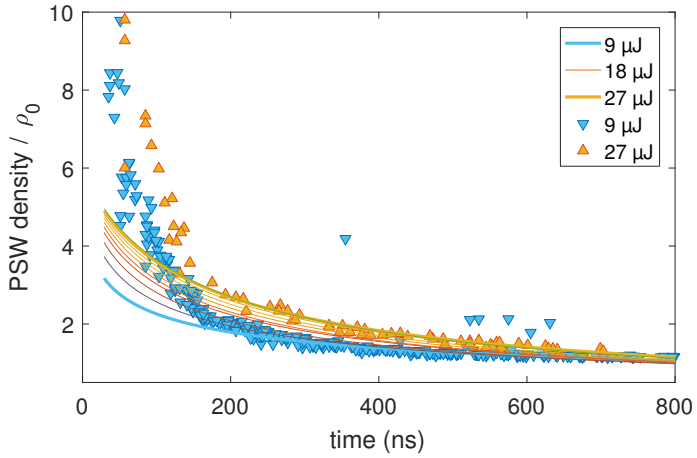

Figure 3.15: To compare the two calculations, lines show the PSW density evolution computed from the shock front velocities in fig. 3.14a, while markers show the centerline density extrapolated from the density reconstructions as shown in fig. 3.12.

density, violating the prediction of the shock-wave model that in the high pressure limit, the maximum shock front density is $(\gamma + 1)/(\gamma - 1) = 6$ times the ambient density for $\gamma = 1.4$ (ideal gas). This indicates that either the specific heat ratio γ deviated significantly from its ideal value for the conditions found at the shock front, or that there was an admixture of ablated water vapor at high density. The latter was very likely the case given that the PSW front and CF had not yet separated for early times.

To summarize, this section demonstrated that DIM can be used to take high contrast images of the shock front expansion following laser ablation. The observed material emission was strongly peaked in the forward direction and was led by a hot and expanding vapor cloud, as was reported in a previous study on DIVE with slightly longer pulses. For large fluences, this vapor cloud took several hundred ns to cool down and it moved fast enough to cause a significant distortion of the primary shock front. Although the significantly faster expansion in the center of the plume indicated a threshold behavior, the reconstructed refractive index field confirmed that even at the highest employed fluence, no significant density of free charges was present after several tens of nanoseconds after laser incidence. Thus, optical breakdown did not contribute to the plume kinetics during expansion, and accordingly no plasma spark was observed. However, an initial contribution from avalanche ionization could not be fully ruled out.

The retrieved phase maps have been used to estimate the shock front density, and a close correspondence with the values obtained through fitting the plume expansion with a shock wave model was verified. The phase maps could alternatively yield the shock front velocity with a single image acquisition: rearranging eq. (3.23) and using ρ_s from the Abel inversion gives an expression for the Mach number.

3.3 Ablation with Initial Spatial Confinement

Microfluidic devices provide the means to integrate various analysis steps into a single platform, to reduce the required sample and reagent volumes, and to increase analysis speed by multiplexing and automation. Silicon, glass, and polymer-based microsystems have become simple and cheap to manufacture, which paves the way for the widespread application of lab-on-a-chip devices to analytical and biochemistry. However, coupling these devices to conventional macro-scale systems for transport and detection can be challenging. Mass spectrometry constitutes an analysis technique sensitive enough to deal with the small analyte quantities, and recent developments and applications of the coupling of microfluidics to MS have been reviewed in refs. [206, 207]. In combination with MALDI-MS, microfluidics have so far mainly been used for the sample preparation steps such as protein digestion and fraction collection from separations. Here, MALDI offers advantages over ESI in terms of reduced cross contamination between fractions and the capacity to analyze small volumes without dilution. Compartmentalizing the preparation steps within an array of micro-droplets on a well plate or patterned substrate surface has proven to be both simple and efficient for multiplexed acquisition of reaction kinetics and for high-throughput screening applications [208]. For example, the fractions produced by nanoflow liquid chromatography (nano-LC) were collected in a micro-array at a high sampling rate of 1 Hz over 45 min and subsequently analyzed by MALDI-MS [209]. A high temporal resolution of the chromatography step and the flexibility of using different matrices for different fractions were highlighted as attractive benefits. Deposition of nanoliter volumes in such micro-arrays has also been used to reduce the spot-to-spot inhomogeneity of MALDI sample preparations [210] and was shown to facilitate quantification of heavy metal contents in blood samples by coupling laser ablation and inductively coupled plasma (ICP-) MS [211].

Naturally, being able to forgo the use of a matrix altogether would be desirable. One approach in this direction is desorption ionization on silicon (DIOS), which has for example been implemented into a lab-on-a-chip device in form of a patterned silicon nanowire surface [212]. DIOS, however, requires that the sample dries out before analysis, and the method is only suitable for small biomolecules. Coupling of micro-arrays to PIRL-DIVE, on the other hand, could potentially reduce the complexity of sample preparation while at the same time permitting the analysis of larger peptides and proteins. It would also facilitate the combination of online monitoring of liquid fractions separated on a microwell array with a subsequent off-line analysis by MALDI. Moreover, the ability to ablate the entire liquid sample volume in a single shot could provide new ablation conditions in which both the lateral spatial confinement and the solid backside support influence the plume dynamics.

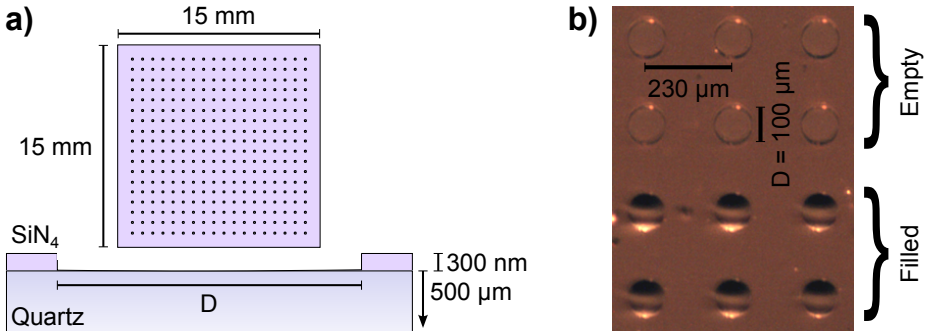

Figure 3.16: Picoliter well chip geometry. a) The top part illustrates the macroscopic dimensions of the chip, the lower part is a sketch of a single well with diameter D etched into the 300 nm thick silicon nitride coating (not to scale). b) A camera view from below the chip is used to position the well structures in focus. The image shows that here the upper rows are empty, while the bottom rows are loaded with glycerol.

This section presents the investigation of the PIRL ablation of picoliter droplets from self-aliquoting micro-arrays by DIM. The arrays were produced by first coating 500 µm thick fused silica wafers with 300 nm of silicon nitride (Si_2N_4) by plasma-enhanced chemical vapor deposition. UV-lithography and reactive ion etching were then used to partially remove the Si_2N_4 to produce hydrophilic well structures with diameters of $D = 100$, 50, and 20 µm in the otherwise hydrophobic surface coating, as is illustrated in fig. 3.16a. The annotated camera view of the sample in fig. 3.16b shows how the wells were spaced 230 µm apart (center-to-center) to allow individual targeting by the laser spot. The wafer was diced into 15 mm × 15 mm chips with a margin of about 500 µm around the well pattern. Wetting of the wells was achieved by dipping a plastic capillary into a larger droplet of glycerol on the surface of the chip, and the chip was then moved slowly (in steps of about 20 µm) along a line of well features while keeping in contact with the capillary tip. Pumping the glycerol through the capillary for continuous sample deposition turned out to not work due to the high viscosity of the liquid, although further investigations with respect to capillary diameter and pumping rate have so far not been conducted. Because the well features were more strongly hydrophilic, the glycerol would stick to them and thus automatically form uniform aliquots at each array position. With a bit of practice, almost all wells could be uniformly filled until the dragged droplet became too small. Imperfectly wetted features could be easily identified by looking at a microscope image of the chip from below and were avoided for the plume imaging. As demonstrated in fig. 3.16b, good contrast between filled and empty features and a homogeneous deposition with little residual liquid between wells was achieved.

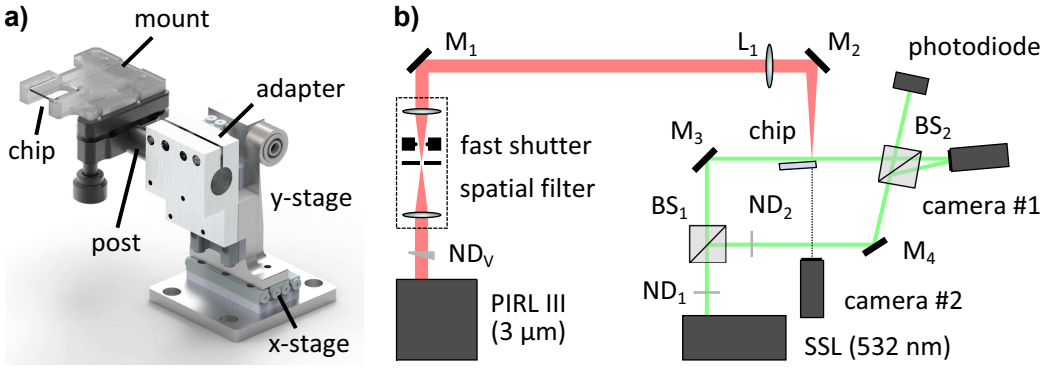

Figure 3.17: Experimental setup for PIRL III. a) Design of the sample holder. The mount held the 15 mm × 15 mm fused silica chips in place and was fixed onto a Thorlabs kinematic prism mount. A custom adapter connected to the stage assembly (z-stage not shown) and clamped around a Thorlabs aluminum post which was fixed to the prism mount. b) A fast shutter was placed in the spatial filter assembly and the beam was focused onto the sample with a lower numerical aperture. The capillary and syringe pump used previously were replaced by the motorized sample holder shown in panel a. A second camera was introduced to monitor the sample position.

While it would be desirable to also study the desorption of aqueous solutions localized to the well pattern, this proved to be challenging with the current setup as the water aliquots would evaporate within a few hundred milliseconds. Previous studies on similar micro-well arrays used a humidity cell to reduce the evaporation rate [213] or dynamically wetted individual wells shortly before laser ablation [111]. However, both approaches would have been difficult to combine with the current imaging setup, so glycerol was chosen as a less volatile solvent.

3.3.1 Changes to the Microscopy Setup

To accommodate flat samples instead of a capillary-held droplet, the imaging setup was modified in several ways. A sample mount was designed and 3D printed to hold the 15 × 15 mm chips without obstructing the camera view and laser path, as can be seen in fig. 3.17a. It was itself mounted onto a Thorlabs kinematic prism mount (KM100B/M) instead of the original mounting plate to allow for simple adjustment of the sample tilt. An adapter was made from aluminum to connect to a set of three translation stages (SLC Series, SmarAct, Germany) and designed so that the assembly would meet the target weight of the stages in combination with a Thorlabs anodized aluminum post. The translation stages were computer controlled and thus facilitated the automated scanning of the sample. This is an important feature for thin-film or micro-volume samples as only few shots can be acquired for each position. To simplify scanning of the features on the micro-well chips, a

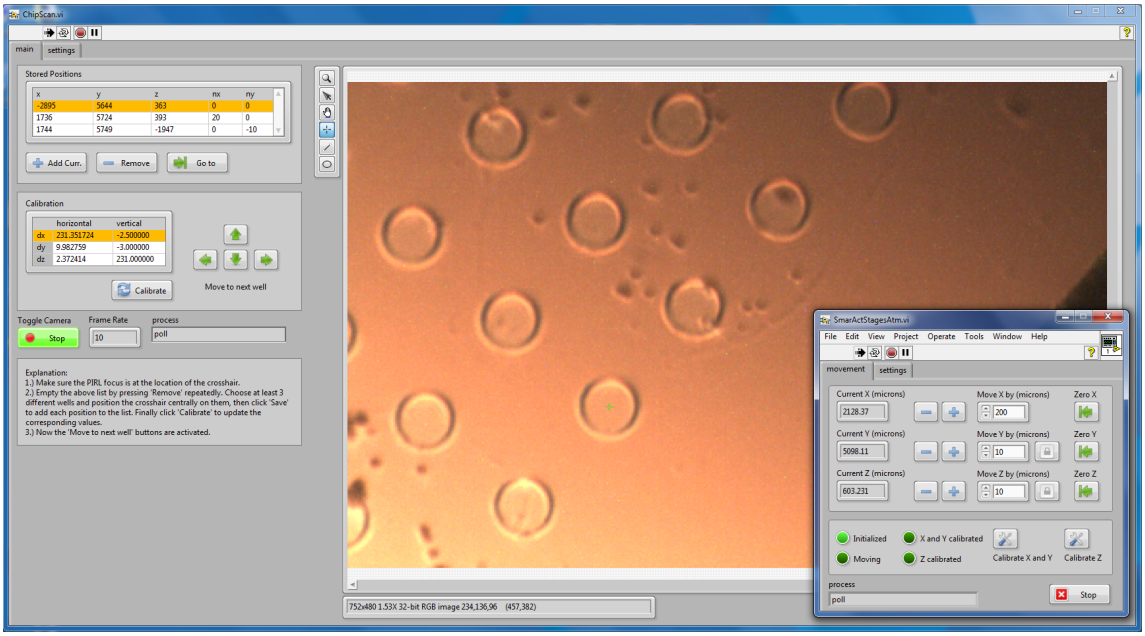

Figure 3.18: LabView user interface for targeting individual well structures. The module *SmarActStagesAtm* controlled the piezo stages that positioned the sample, while the module *ChipScan* was used to calibrate the distances in the xz-plane and the vertical shift along y by taking three or more reference positions.

script to calibrate the distance between adjacent wells and to automatically compensate for shifts in vertical sample position, produced by slight tilts of the chip, was implemented in LabView. A second camera was incorporated into the setup to monitor the sample from below, such that calibration in the horizontal xz-plane, where z is directed along the illumination laser beam, could be performed using this camera view, and calibration in the xy-plane was performed according to the main camera. An image of the control software can be seen in fig. 3.18. Correct illumination of the well-chips was crucial to be able to distinguish the well features from the unmodified surface. The best results were achieved with a diffuse illumination by pointing a high power LED lamp at a white surface (a sheet of paper) positioned right next to the PIRL focusing lens. The chip was held at a small angle around the x-axis, with the edge of the chip facing the main camera being slightly further up than the edge facing away, to avoid out-of-focus contributions from the substrate and clipping of the illumination laser beam. Without this tilt, strong horizontal stripes would show up on the interference image.

Representing the second big change compared to the previous section, the new PIRL III (PIRL-III-ND, Light Matter Interaction Inc., Canada) was used for the experiments presented here, and a sketch of the adjusted setup can be found in fig. 3.17b. This laser had significantly more pulse energy (up to 1.35 mJ) and a longer pulse duration ((400 ± 50) ps) than the

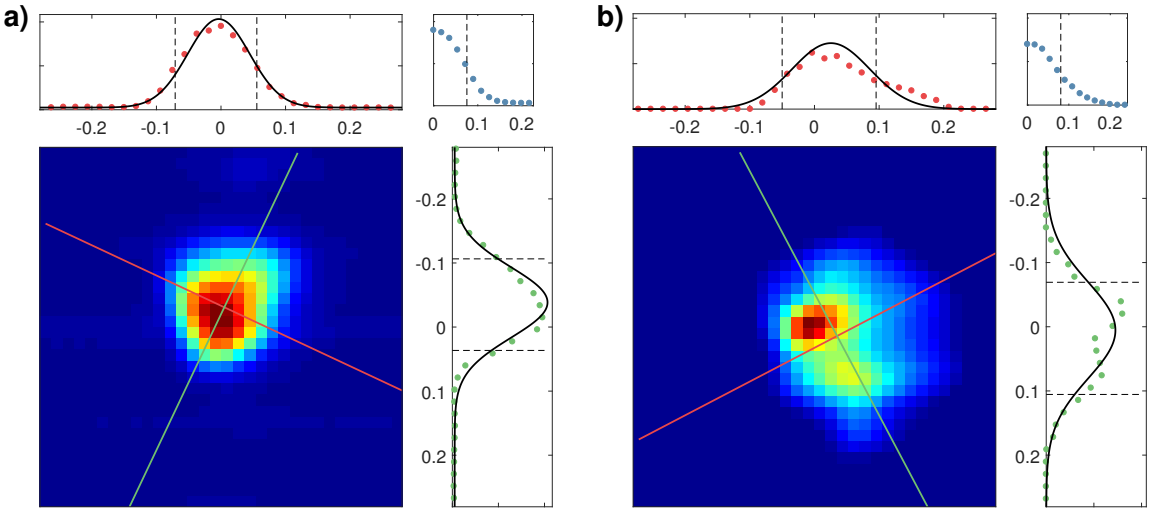

Figure 3.19: PIRL III beam profile in the focus of a $F = 150\,\text{mm}$ lens. a) Using a $200\,\mu\text{m}$ pinhole spatial filter to clean up the beam. b) Without spatial filtering. The profiles on the top and right side are shown along the red and green line drawn on top of the beam profile image, respectively. The top right shows an integrated radial profile. The annotated distances are in mm, one pixel of the WinCam beam profiler corresponds to $17\,\mu\text{m}$.

PIRL I, which was necessary to be able to ablate full micro-volumes from the chips. According to the specifications, the emission spectrum was centered at 2917 nm with a full width half maximum (FWHM) of 28 nm. A $F = 500\,\mu\text{m}$ lens was used right at the PIRL III output to prevent excessive divergence of the beam, and the telescope / spatial filter assembly was set to unity magnification by using two plano convex lenses with $F = 100\,\text{mm}$, which were adjusted to yield a collimated output beam. Triggering was implemented very similar to what was described for PIRL I: the PIRL III was set to continuous operation and its trigger output was used to trigger the delay generator. A shutter with a larger aperture was used for these experiments and placed within the spatial filter / telescope assembly right after the pinhole. The delay generator would trigger the shutter control (VCM-D1, UniBlitz, USA) and microchip laser (FDSS 532-Q, CryLas GmbH, Berlin, Germany). Because the trigger output had a large delay and jittered considerably with respect to the actual output pulse, a fast photodiode (Thorlabs DET10) was inserted into the laser enclosure right behind the final mirror, and the delay between the PIRL and the microchip laser pulse determined on an oscilloscope.

It was found that merely recording the average output power of the laser was sufficient and pulse to pulse fluctuations were not taken into account for the data analysis in this section. The shot-to-shot pulse energy was still monitored, but now, in lieu of a good position for a beam-splitting mirror, by pointing the photo-diode at the back-side of the shutter to collect stray light. This method was not as reliable as using a direct beam, as the shutter operation

changed the amount of stray light reaching the detector. Nonetheless it was used to monitor trends in the beam power which appeared due to warm-up of the system. Rough estimates were achieved by calibrating the average diode reading to that of a power meter placed in front of the focusing lens. Single shot mode had to be used for the diode readout during calibration to fix the influence of the shutter movement on the amount of detected stray light.

The larger pulse energy of the PIRL III as compared to the PIRL I facilitated the choice of a larger focus diameter. This also allowed positioning of the focusing lens considerably further away from the sample, which greatly simplified alignment and increased the Rayleigh range. A lens with a focal length of $F = 150\,\mathrm{mm}$ was chosen and placed before the last mirror in the setup, which approximately matched the focus FWHM to the largest well diameter to be introduced in the experiment. Figure 3.19 shows the beam profile in the focus as measured by a WinCamD beam profiler (DataRay Inc., USA). In fig. 3.19a, a 200 µm pinhole was used to spatially filter the beam, similar to the setup described in section 3.2.1. This way, an almost Gaussian beam profile with $1/e^2$ diameters of 243 µm × 215 µm was achieved. However, the pinhole tended to be damaged when large fluences were used due to the high laser fluence in the focus of the telescope assembly. Figure 3.19b shows the focus beam profile when no spatial filter was used. In this case, a strongly asymmetric double peak was formed, and the plume images showed significant distortions based on the irregular intensity distribution. The experiments presented in section 3.3.2 were performed with the profile shown in fig. 3.19a. The stated fluences were calculated according to eq. (3.18) and correspond to the pulse energy transmitted to the sample position.

3.3.2 Plume Dynamics from Picoliter Wells

The ablation dynamics observed for the irradiation of a water surface with the PIRL III were very similar to those shown for PIRL I. Figure 3.20a and b show the plume for a fluence of $0.3\,\mathrm{J/cm^2}$ (top) and $0.8\,\mathrm{J/cm^2}$ (bottom) for a static water droplet placed on a fused silica surface. As for previous images, the number in the top left denotes the time delay with respect to the PIRL pulse, and the scale bar in the top right indicates 100 µm in the object space. Although a larger spot diameter and longer pulse duration were employed here, the dynamics looked very similar to what was shown in fig. 3.6a,c,e. The ablation threshold, however, was observed to be below $0.08\,\mathrm{J/cm^2}$ and thus markedly lower than for the experiments with PIRL I. Furthermore, the larger focus size and increased amount of ablated material generated an even more pronounced bulge of the primary shock wave (PSW), and this bulge took a longer time to dissipate.

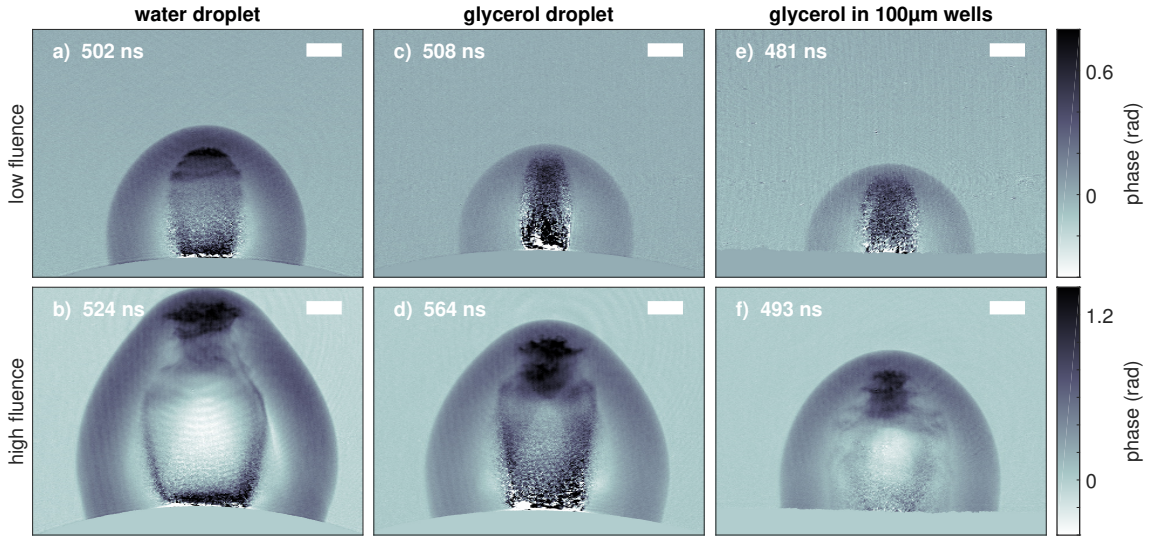

Figure 3.20: Reconstructed phase images of the early stage plume expansion for the ablation from a water droplet (a,b), a glycerol droplet (c,d), and from self-localized glycerol volumes (e,f). A lower laser fluence of $0.3\,\mathrm{J\,cm^{-2}}$ ($60\,\mu\mathrm{J}$) was used for the top row, a higher one of $0.8\,\mathrm{J\,cm^{-2}}$ ($170\,\mu\mathrm{J}$) for the lower one. Time stamps are relative to the time of laser incidence, scale bars indicate $100\,\mu\mathrm{m}$.

The laser fluence and delay values were kept roughly the same for the other panels of fig. 3.20, with the upper row corresponding to the low and the bottom row to the high fluence regime. For glycerol, which was also dropped onto the fused silica substrate, the ablation threshold was higher than for water, namely slightly below $0.15\,\mathrm{J\,cm^{-1}}$. Because a smaller part of the focus beam profile was above threshold at the same fluence, this caused a smaller lateral extent of the recoil splash, as can be seen in fig. 3.20c and d.

Figure 3.20e and f show the dynamics after ablation of a volume of glycerol self-localized in one of the shallow wells with $D = 100\,\mu\mathrm{m}$ diameter of a micro-array. Two distinct features were apparent for the ablation from well structures: on the one hand, the shockwave was slower and the PSW bulge was not as pronounced when compared to the ablation of droplets of water and glycerol at the same fluence. On the other hand, the recoil splash was much smaller in fig. 3.20e and even absent in f, indicating that the well volumes could be fully depleted in a single shot. In addition, in the latter case, i.e. in the high fluence regime, the amount of ejected droplets was strongly reduced. Notably, this meant that by changing the employed laser fluence, the plume composition could be switched from being mainly comprised of droplets to being fully vaporized.

Just as presented in section 3.2.5, the plume expansion was fit by a Taylor-Sedov model with variable exponent. This time, the plume origin on the liquid surface, the contact front (CF) and the PSW in normal direction were selected by hand, as only a lower number

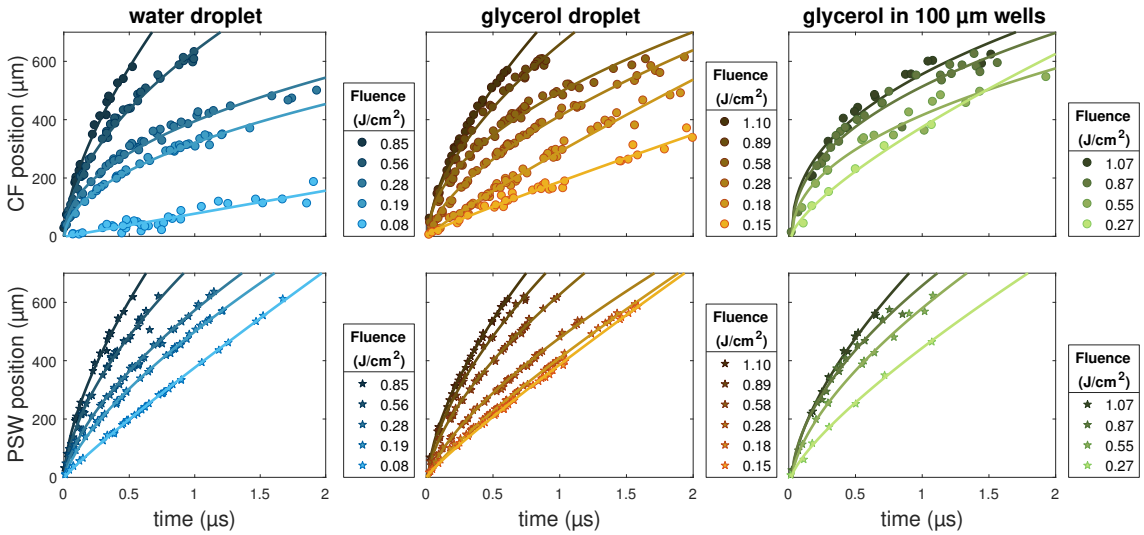

Figure 3.21: The Taylor-Sedov model fit applied to the transient shockwave positions of the contact front (CF, top) and primary shock front (PSW, bottom) for the ablation from a water droplet (left column), a glycerol droplet (center), and from self-localized glycerol volumes on the micro-array (right).

of images had to be processed. The CF boundary could be identified more reliably by hand than with the algorithm, although with some degree of subjectivity. Figure 3.21 shows the data and fit results for a water droplet, for a glycerol droplet, and for glycerol volumes self localized in the chip features. The top row shows the CF data and the bottom row the PSW data. At equal fluence, both the PSW and the CF expanded slower for glycerol than for water during the first few hundred ns, indicating that the initial dynamics scaled with the ablation threshold, i.e. that they depended on the amount of material that reached the critical energy density for vaporization. For later times and at low fluences, however, the expansion of the CF seemed to slow down more quickly for water (compare curves at 0.18 and 0.28 J/cm^2). This effect was interestingly not observed at higher fluences, where the PSW and CF from water were moving faster. The sudden jump in expansion velocity from the water surface between 0.56 J cm^{-1} and 0.85 J cm^{-1} coincided with the appearance of the PSW distortion. The fits for the ablation from the micro wells were less accurate, and especially the curve for the lowest laser fluence was of insufficient quality. Still, they aid in illustrating the slower expansion velocity for smaller sample volumes. The extracted parameters displayed in fig. 3.22 indicated the same trends. Larger values of A were determined for a faster initial expansion, whereas larger values of q reflected a slower dissipation of the forward momentum. Note how the curves for glycerol mirror the ones for water but are shifted towards higher fluences.

The snapshots of the ablation from micro wells taken at constant time delays of 0.5 µs and

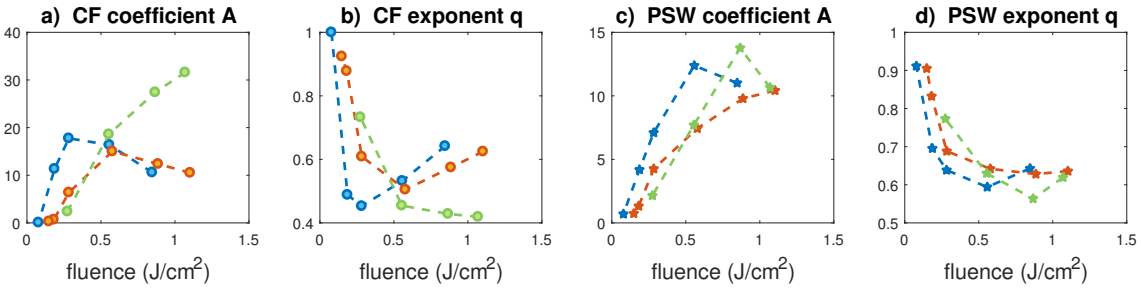

Figure 3.22: Fit coefficients A and q as a function of laser fluence for the ablation from water (blue curve), glycerol (blue curve), and picoliter volumes of glycerol (green curve). Panel a and b show results for the contact front (CF), c and d show those for the primary shock front (PSW).

5 µs for different laser fluences in fig. 3.23 demonstrate how the recoil splash usually found for the ablation from larger sample volumes can be reduced and even completely avoided for micro-volumes when the employed laser fluence is sufficiently large. These images were recorded with a larger (300 µm diameter) pinhole in the spatial filter which gave a slightly larger focus spot with beam waist diameters of 265 µm × 236 µm. Panels e and f are taken close to the ablation threshold and show a faint PSW at early times and a liquid fountain after several microseconds, similar to what has been observed for the ablation from larger sample volumes. At intermediate volumes, shown in panels c,h,d,i, the material is mainly ejected in form of droplets, but because almost all the material localized in the micro well is depleted, the usual recoil splash is absent from these images. At the highest fluences in panels a and b, the ablated material is (almost) fully vaporized.

Not all of the pulse energy was utilized for the phase transition. A volume of 9.5 pL was determined for individual droplets of water loaded in the micro-array by confocal microscopy. Experiments were performed in a humidity chamber so the water would not evaporate. The fraction $\mathrm{erf}\left(\sqrt{2}D/w\right)^2 \approx 0.33$ of the pulse energy of 410 µJ hitting the $D = 100$ µm diameter well would, however, suffice to bring an amount of about 110 pL into the gas phase, which is about 10 times this volume. Some losses of optical energy can be expected because with glycerol's absorption coefficient of about 2700 cm^{-1}, only about 40 % of the irradiation will be absorbed in a 2 µm thick film. Clearly, this cannot account for all of the observed discrepancy. Moreover, the question remains why the measured ablation threshold differs so significantly for PIRL I (0.5 $\mathrm{J\,cm}^{-2}$) and PIRL III (0.1 $\mathrm{J\,cm}^{-2}$), while the latter is very similar to the threshold of 0.2 $\mathrm{J\,cm}^{-2}$ measured by Franjic and Miller [17]. One possible reason could be an inaccuracy of the determined fluence values. The PIRL focus beam profile tends to be highly inhomogeneous and thus difficult to characterize with an analysis based on Gaussian beams.

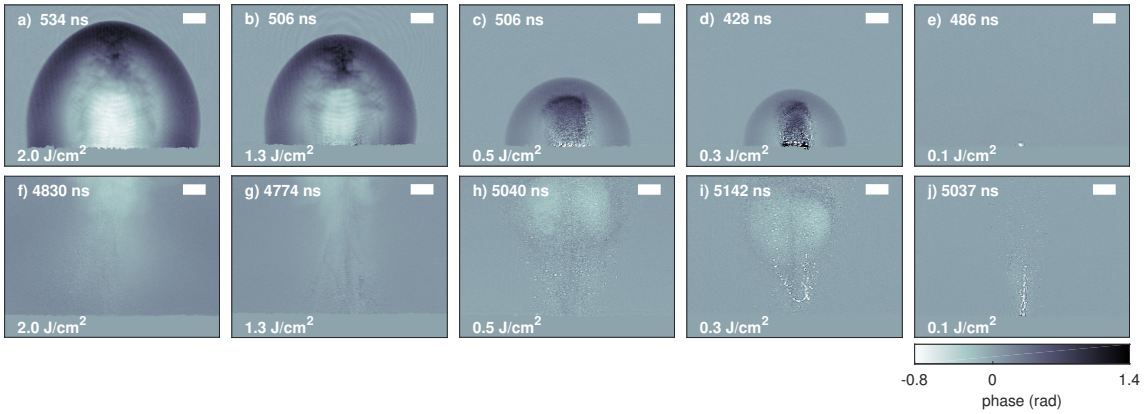

Figure 3.23: Ablation from self localized glycerol droplets in 100 μm diameter wells at different time delays (top 0.5 μs to bottom 5 μs) and laser fluences (left to right, 500 μJ to 20 μJ pulse energy). Scale bars in the top right indicate 100 µm.

The differences could also be a real effect, however, as the three experiments (PIRL I, Franjic and Miller, PIRL III) differ significantly in the employed spot size (≈50, 100, and 200 µm) and pulse duration (≈10, 100, and 400 ps). A spot size effect on the detection threshold is known for MALDI, where the ion yield at constant fluence is typically higher for larger spots, although the origins of this effect are still unclear [54]. For the ablation observed by DIM, a larger threshold can be expected because more material is vaporized per shot, leading to a larger pressure buildup and to more material being displaced. In addition, high irradiance and fluence values can have nonlinear effects on the absorption spectrum. At very high irradiances, spectral bleaching can occur, such that a population inversion makes the transition from the vibrational ground state to the first excited state inefficient. The transition from the first to the second excited state typically requires slightly less energy because of the anharmonicity of the atomic potential, leading to a shift of the peak absorption towards longer wavelengths. This could lead to a larger optical penetration depth for shorter pulse durations, especially when the time scale of energy deposition is comparable to the lifetime of the excited state (200 fs for water), and thus reduce the energy density in the ablation volume. For 100 ps pulses, however, a different effect has been observed to be more significant for the ablation of water: because an increase in temperature weakens the hydrogen bond network, which in turn strengthens the water O−H bonds, the absorption peak shifts towards shorter wavelengths (larger photon energies) [17, 214]. A 10 % reduction in optical density was shown for a 5 µm thick water film at 2.94 µm wavelength and a fluence of 2 J cm^{-2}, but the effect should be stronger for thinner layers due to the exponentially decaying temperature profile with sample depth. The high-fluence regime shown in the experiments here were performed well above the ablation threshold, in particular the plume

expansion shown in fig. 3.23a and f. Although the nonlinear absorption spectrum of glycerol is not known, the high fluence necessary for complete vaporization strongly suggests that the absorption was significantly below the value of 40 % stated earlier.

No obvious changes of the plume dynamics which would point towards an influence of lateral confinement were observed except for a faster dissipation because less material was ablated. It would be of interest to see if confinement in deeper wells and with a negative meniscus would cause a more forward-peaked plume expansion. Micro-arrays for this purpose are being manufactured and will be characterized in the future.

3.3.3 Particle Delivery from Picoliter Wells

Considering the large volumes sampled per shot with IR laser ablation and the low internal energies imparted to the ejected material under DIVE conditions, the technique could potentially be used for soft targeted sample delivery of macroscopic objects such as protein crystals. This approach is especially promising in combination with serial femtosecond crystallography (SFX), in which the sampling rate is currently the main limiting factor to improving resolution and sample throughput. In SFX, a bright, femtosecond X-ray pulse is focused onto a sample crystal, exposing it to such a high photon flux that only a single diffraction pattern can be recorded before the crystal is vaporized. Although this diffraction-before-destruction approach mitigates radiation damage during the acquisition and thus strongly relaxes the requirements on crystal size, the approach instead requires that many diffraction patterns have to be accumulated to be able to solve the molecular structure because each individual crystal is found at a random and a priori unknown orientation.

Crystals are usually fed into the beam in their mother liquor in form of a liquid jet. Because such a jet cannot easily be suspended between pulses without causing significant turbulence, the required sample amounts are typically very large, leading to high financial cost and long lead times for the intricate sample preparation. A number of strategies has been developed to reduce the sample consumption [215]. Fixed targets such as windowed sample supports or microfluidic chips can increase the sample hit rate, which for liquid jets typically lies between 10 to 30 %, by either very reliably loading the sample or by indexing suitable sampling positions prior to the experiment. However, the support structures necessarily introduce some amount of background scattering. PIRL ablation from frozen picoliter volumes of mother-liquor containing the analyte crystals could separate the solid crystals from their liquid environment and thus suppress this background while at the same time facilitating an indexing approach for 100 % hit rate, as has been suggested in ref. [1].

A similar technique, laser induced acoustic desorption (LIAD), in which the laser hits

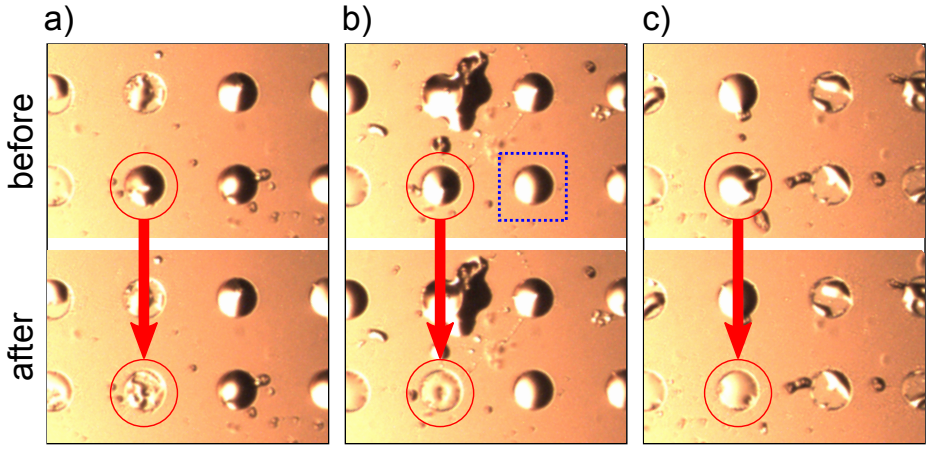

Figure 3.24: Images taken of the micro-array wells before (top) and after (bottom) the ablation event corresponding to the plumes shown in fig. 3.25. The red circles mark the targeted well for each panel. The blue square in b) marks a well which is loaded with glycerol but does not contain a polystyrene particle.

an opaque sample substrate from the backside to create an ablating shockwave, has been proposed for the creation of gas-phase molecular beams and their coupling to large-scale user facilities such as free electron lasers [216]. Large nano-particles have also been desorbed into the vacuum of mass analyzers by using a sacrificial layer as a sample support [217], a technique called laser-induced forward transfer (LIFT). The envisioned advantage of PIRL-DIVE over these approaches lies in the ability to desorb crystals directly in their native environment, in the focusing of the ejectas' angular distribution by using lateral confinement in micro-patterned well structures, and in the evaporative cooling of the ejected particles by the desorbing liquid.

The present section describes a proof of principle study of the PIRL ablation of polystyrene beads self-localized into the previously described well structures on a micro-array chip. Beads with a nominal diameter of (10.0 ± 0.2) µm (72986, Sigma Aldrich) were suspended in distilled water at a concentration of 1 % (v/v) and applied to a suitable position on the micro-array. The water would quickly evaporate, leaving a sparse distribution of beads on the surface. The wells were then re-wetted with glycerol as described in the previous section, with some of the polystyrene beads localized within the well structures. Figure 3.24 shows the region of interest from the view of the monitoring camera located below the sample before and after different ablation events. The blue square annotated in panel b) indicates a well that was loaded with glycerol but did not contain any polystyrene beads. The reflection appeared very smooth and round. In contrast, the wells marked with a red circle in the top row of panels a,b, and c show a more irregular reflection, which indicated that they each contained at least one bead. As can be seen from the bottom row of the figure, ablation with a pulse energy of

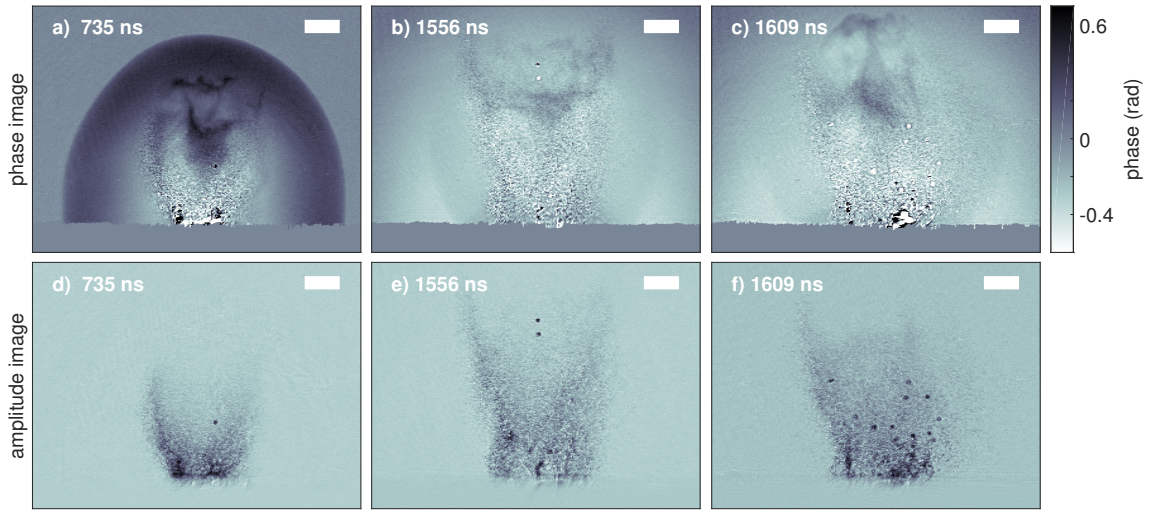

Figure 3.25: Polystyrene particle ejection during PIRL ablation. The top row shows the reconstructed phase, the bottom row the amplitude images for three different ablation events. Ablation was performed at a peak laser fluence of about $1\,\mathrm{J\,cm^{-2}}$. Panels a,d, b,e, and c,d in this figure correspond to panels a, b, and c in fig. 3.24.

$(194 \pm 3)\,\mu\mathrm{J}$ at the sample location removed not all but most of the glycerol in a single shot. The images in fig. 3.24 correspond to the three snapshots of the plume expansion presented in fig. 3.25. The top row of this figure shows the reconstructed phase images, demonstrating the same plume dynamics as in the previous chapter. The beads can be better identified in the amplitude images in the bottom row, however. Panel a) shows the ablation of a single bead, panel b) contains at least two beads, and a large number of particles was ejected in panel c). The number of particles could not be well controlled during deposition because they did not self-localize into the wells during the evaporation of the solvating water. The subsequently applied glycerol, while it did localize itself, did not sufficiently re-solvate or transport the beads to the desired positions. A look at the monitoring camera, however, helped to estimate the number of particles in a given micro droplet (see fig. 3.24).

Notably, particles could be efficiently ejected and would spatially separate from the liquid phase droplets after a few hundred nanoseconds. The beads also produced no pronounced diffraction rings in the images up to several microseconds of propagation, indicating that they stayed roughly within the depth of focus of the microscope objective. This and the observed lateral positions above the well structures imply a reasonably small angular spread of the ejection velocities. The ejection velocity normal to the chip surface was analyzed by recording the positions of all beads with respect to the chip surface for each recorded image at a fluence of roughly $1\,\mathrm{J\,cm^{-2}}$. The position of the bead furthest away from the surface for each image is shown in orange in fig. 3.26. The rest of the bead positions are plotted in

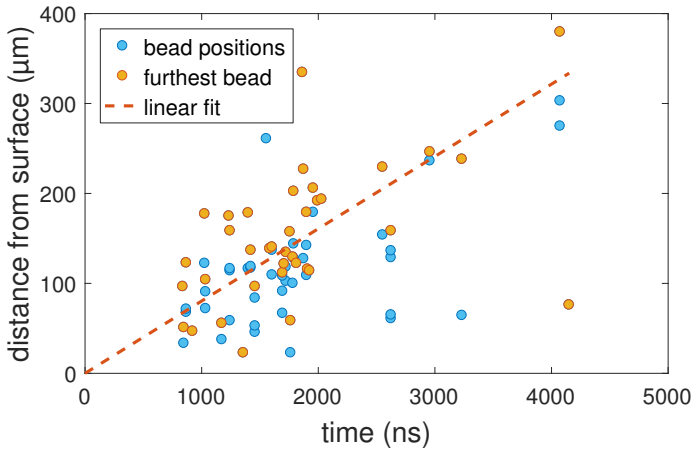

Figure 3.26: Vertical distance of the identified 10 µm polystyrene beads as a function of delay time with respect to the PIRL pulse. The distance of the bead furthest away from the surface is shown in orange for each image, while the positions of all other beads are shown in blue. The dashed line represents a linear fit of the furthest bead positions with zero intercept.

blue. A linear fit of the furthest bead positions with zero axis intercept produced an average velocity of about 80 m s^{-1}, although the actual positions scattered vastly around this value.

3.3.4 Conclusion

While the technique still needs some development to be efficiently used for sample delivery into the micro-focus of a FEL, some important results can be put on record. The lateral position spread of the particles approximately equaled the diameter of the well structures when interrogated close to the surface and could thus potentially be controlled by simply matching the crystal size to the well diameter. As an example, the European XFEL can be operated at 1 to 200 µm beam radius (disregarding the optional nanofocus which can bring the beam waist down to tens of nanometers). A reasonable working range is thus accessible once sample loading into smaller well structures can be realized.

The longitudinal position spread can be predicted to be more severely limiting. The XFEL is in principle capable of firing 27 000 pulses per second. These are organized into micro-bunches, and often only a subset of pulses is actually used. At the maximum intra-bunch repetition rate of 4.5 MHz, the time between pulses amounts to 220 ns. To transfer individual nanocrystals to a position appropriate for the interrogation by the beam, presumably 20 µm from the surface, an initial velocity of about 90 m s^{-1} is required, closely matching the speeds observed here. This means that scanning the micro-array surface with a laser beam row-by-row, while moving the sample via a translation stage between each line, is a scenario well in reach. Higher velocities can be achieved for higher fluences, and can also be expected

if water instead of glycerol is used as the matrix liquid.

However, to be a viable option, the width of the initial velocity distribution needs to be strongly reduced. Smaller well structures with a more precise initial particle position and consequently more predictable amount of surrounding liquid could help to achieve this goal. It would moreover be interesting to see if the angular spread can be reduced by using deeper well structures which form a negative meniscus of the loaded liquid and thus laterally confine the ablation volume within a solid support structure, acting as a guiding barrel for the microparticle ejection.

Finally, while the experiment showed that particles with a diameter suitable for x-ray crystallography could be desorbed, the question whether the method is soft enough for the ablation of protein crystals, which contain a large amount of water, remains to be answered. Promising results in this regard were gathered by collecting the ablated protein crystals in a solvent bead for subsequent off-line analysis [1]. Macroscopic crystal fragments up to 25 µm in size were observed after PIRL ablation and transfer. Further experiments are in order.

3.4 Summary and Outlook

The material expansion during laser ablation is known to largely affect the collection and ionization efficiency in MALDI and other laser-based MS approaches. This chapter demonstrated that time-resolved digital interference microscopy is a viable technique for the characterization of the laser ablation event and that it can capture both the ejected solid or liquid phase material and the acoustic shock front and vapor phase material. The recorded images had high contrast and a competitive spatial resolution to that achieved in previous dark-field and Schlieren photography experiments. For fluences close to the ablation threshold, there seemed to be no significant differences between PIRL ablation and the results for IR laser ablation with longer pulses known in the literature. At high fluences, however, picosecond ablation produced an optically transparent cloud of material with high refractive index which initially traveled faster than the primary shock front and thus distorted the otherwise approximately hemispherical plume expansion into a more forward-peaked shape. While a similar distortion has been observed for the contact front (i.e. the vaporized sample material) in non-stress confined ablation before [188], it had not been further characterized and not been shown to be the cause for a distortion of the primary shock front.

The significance of this material cloud for mass spectrometry is currently not clear. One way to investigate the material ejection more closely would be to switch between an ablation regime in which mostly droplets are ejected and a regime in which all the ejected material

is in the gas phase, and analyze the ejecta by mass spectrometry, e.g. in an ion-trap mass spectrometer such as that used by Y. Lu and coworkers [111]. As has been shown in section 3.3.2, this regime can be reached with the use of the presented micro-array. While water was not used as the sample material in the work presented here because of the timely evaporation of such micro volumes, dynamic wetting with a water droplet suspended from a capillary tip and desorption within few tens of milliseconds is certainly possible as shown by Lu *et al.*

The desorption of micro particles demonstrated in section 3.3.3 showed that laser-assisted delivery of protein crystals into the x-ray beam of a free electron laser could be feasible as the average observed particle velocity is in range for this application. Further instrumental developments are required, however, to reduce the initial velocity spread and improve sample loading. A new generation of micro-arrays with deeper wells, similar to the ones presented in ref. [213], has been designed and is currently being manufactured. The plume dynamics and their effect on micro-particle velocity and angular spread from these structures will hopefully be investigated soon. The new design will certainly still be lacking in usability because the self-localization approach did not work as well as expected for polystyrene particles with 10 µm diameter. This could potentially be resolved by a more intricate design of the chips similar to the one recently developed for serial crystallography [1], in which the crystals are pushed into tapered wells containing a through-hole by temporarily applying a small pressure difference between the upper and lower side of the chip. The well depth would need to be adjusted to allow quick extraction out of the features, and the influence of the through-hole on the plume expansion would have to be investigated.

After having successfully demonstrated the application of DIM to PIRL-DIVE under atmospheric conditions, an extension of the study to the ablation at different pressures, in particular the high vacuum of a time-of-flight mass analyzer, is desirable. Due to the spatial constraints of a vacuum chamber and the additional need for cooling of the analyte liquid, this will be a complex endeavor. The even lower material densities expected for in-vacuo ablation would, however, play to the strengths of DIM because of its high sensitivity to the difference in refractive index between the sample and its environment. If image contrast can be achieved, this would represent a novel approach to determine the initial velocity distribution of ejected neutrals and the influence of droplet generation on the ion yield in MALDI-TOF-MS.

Chapter 4

In-Vacuo Laser Desorption Ionization Time-of-Flight Mass Spectrometry

This chapter explores the suitability of PIRL-DIVE for laser desorption ionization mass spectrometry in the vacuum of a time-of-flight mass analyzer. Setup and calibration of the device and the actual measurements were done in close collaboration with C.L. Pieterse and A. Krutilin. The design of the vacuum chamber was done by J. Gonschior, that of the flight tube and custom ion optics by D. Gitaric. The sample mount, liquid nitrogen cooling, and sample loading mechanism were conceived by the scientific support unit, consisting of F. Tellkamp, H. Schikora, M. Kollewe and J.P. Leimkohl. The sheet resistance of several silicon wafers was verified by T. Matsuyama, who also gave insights into signal decoupling and high frequency noise.

The development of picosecond infrared laser desorption ionization for time-of-flight mass spectrometry is driven by the need for an improved method for spatial mapping of biomolecule concentrations in tissues and cells. This is because the larger the number of sample preparation steps, such as repeated freeze-thaw-cycles, dessication, or the application of a MALDI matrix, the larger is the risk for distortion of the distribution of these molecules. Sample rupture, analyte diffusion, and inhomogeneous incorporation of analytes into MALDI matrix crystals are known problems for high resolution mass spectrometry imaging (MSI) [218]. Direct analysis of frozen tissue sections would thus be desirable. Time-of-flight (TOF) instruments offer the high duty cycle and sensitivity required for this application. In addition, the TOF geometry allows for the implementation of stigmatic ion imaging, which could potentially push the resolution limit down into the sub-cellular regime. This could be especially important for infrared (IR) laser ablation in which the minimum achievable focus spot size is more constrained due to the diffraction-limit compared to techniques employing UV lasers. It was up to this point not clear, however, if the ion yield from PIRL-DIVE would be sufficient to produce mass spectra at such high spatial resolution.

Several studies have investigated LDI from frozen aqueous solutions in vacuum. Williams and coworkers used a dye laser in the visible wavelength regime (589 nm) to ablate frozen DNA molecules and proteins from oxidized copper substrates [219–221]. While the presented spectra of DNA segments with up to 60 nucleotides (30 kDa) looked very clean and showed improvements over the corresponding UV-MALDI spectra including reduced ion fragmentation and mainly singly charged peaks, the authors noted that signal was only seen in a small subset of samples and only at the very rim of the applied layer. Sufficient reproducibility was thus not achieved. They hypothesized that ablation was initiated by heating the copper substrate (employing a laser fluence of about $10\,\mathrm{J/cm^2}$), which could only result in ion signal in case a very thin sample layer was irradiated. A later study of femtosecond UV-LDI of frozen acetonitrile/water solutions with fluences $> 2\,\mathrm{J/cm^2}$, on the other hand, claimed to routinely observe strong ion signal and presented high-quality spectra of peptides with masses up to 5778 Da (insulin) [222]. However, UV laser ablation with such high irradiance can be expected to incur significant photo-damage to heavier molecules.

Berkenkamp et. al. took a different approach and employed an Er:YAG laser at 2.94 µm wavelength and 150 ns pulse duration for IR-LDI from bulk frozen solutions which would not depend on substrate heating [20]. Again, protein signal was only seen sporadically, with poor signal to noise ($S/N \leq 10$), and only on the very edge of the applied sample. Batltz-Knorr et al. observed spectra of similarly poor quality using trains of picosecond IR pulses at 5.9 µm wavelength from a free electron laser with a macro pulse length of 120 ns [21]. Spectra in both IR studies suffered from large amounts of chemical noise from water clusters. The material ejection including the velocity distribution of such clusters was investigated by IR ablation and subsequent UV postionization [223, 224] and it was proposed that heavier clusters (up to 100 molecules) might be preferentially produced in thick samples that show greater inhomogeneity [225].

Two experiments by the Dreisewerd group have so far been successful in generating ions of large biomolecules by in-vacuum IR-LDI from aqueous samples. Pirkl et al. demonstrated the analysis of oligosaccharides, peptides, and proteins up to 150 kDa (IgG monoclonal antibody) in an orthogonal-TOF instrument in which the material was ablated at a background pressure of 1.5 mbar before being injected into the TOF region [94]. Cooling and desolvation by the background gas were proposed to be the reason for an improved sensitivity and mass range compared to previous studies. They showed reduced chemical noise by fragmentation, no significant water cluster ions above 130 Da, and a limit of detection in the femtomole range for the investigated compounds. In addition, the detection of non-covalently bound holo-myoglobin was a clear indication of the method's softness. A subsequent study on the same device backed this claim by showing spectra of intact deprotonated species from

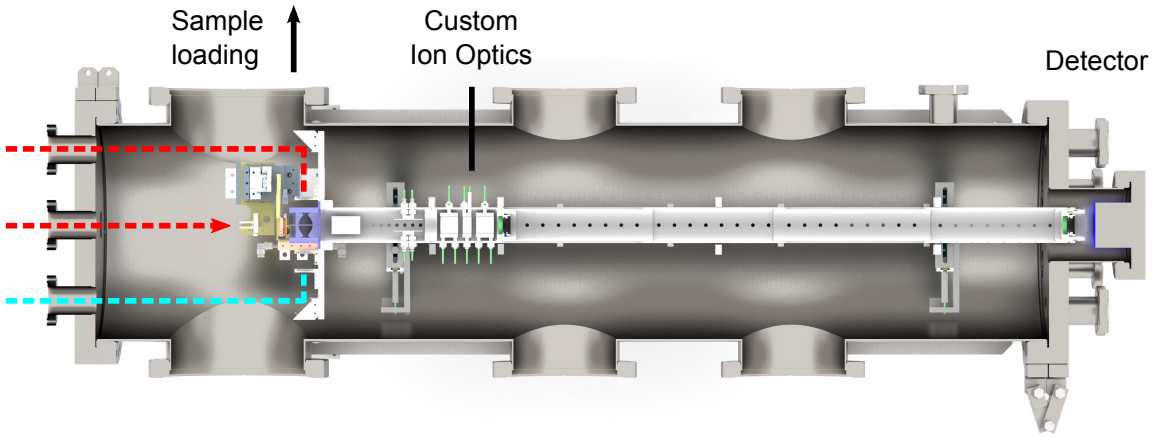

Figure 4.1: CAD rendering of the TOF chamber. The laser beams entered through one of three viewports to the left: the outer ones for front ablation hit one of the mirrors extending from the extraction region (marked in blue but not rendered), the central one was used for back ablation. The sample holder is shown in dark yellow. Electrical contacts for the custom ion optics, including the deflector plates and a second Einzel lens, are marked in green. A metallic flight tube shielded the drift region from stray electromagnetic fields and extended all the way to the detector which is shown in blue.

a family of sulfated polysaccharides in different charge states, with only a minor loss of the labile sulfate groups [95]. The orthogonal TOF geometry does however not permit stigmatic ion imaging and is slightly more complicated than a conventional TOF device. On the other hand, Leisner et al. used IR postionization of the material cloud ablated by an Er:YAG laser (120 ns pulse duration) or OPO (6 ns pulse duration) in a reflectron TOF mass analyzer [226]. While this two-laser system produced high ion yields for the examined molecule cytochrome c (12 360 Da), it can be considered even more complex than an ortho-TOF device, and stigmatic ion imaging would be challenging to implement due to the time-lag between ablation and ionization.

The work here was aimed at implementing PIRL-DIVE in a TOF mass analyzer for spatially resolved imaging of ion distributions in aqueous samples. Optimized laser parameters, in particular the short pulse duration, and an improved sample preparation with parallels to that known from cryo-electron microscopy were envisioned to increase the ion yield with respect to the studies described above. Because the long-term objective was to implement mass spectrometry imaging with high spatial resolution, backside illumination of the sample was supposed to reduce the working distance of the laser focusing optics. The chapter will begin by laying out the design considerations for the mass analyzer.

4.1 Instrumental Design

The instrument was custom-built to allow for a large amount of flexibility, and some of the key challenges shall be outlined within this section. Quick and reliable sample loading was implemented in form of a patented locking mechanism for the sample mount which can unfortunately not be shown in detail here. The requirement of irradiating the sample from the back-side to increase the spatial resolution of the instrument posed very strong restrictions on the design of the sample mount and the sample thickness. To solve initial problems with the back-side ablation, both the front- and back-side geometry were finally implemented. A top-view of the setup is shown in fig. 4.1, in which the three laser paths for the UV laser and the PIRL in front- and backside ablation are illustrated. The ion extraction region was based on the one used in many Bruker instruments and is thus also not shown in detail.

4.1.1 Load Lock and Sample Mount

Sample cooling was critical for the investigation of frozen aqueous films, cells, and tissues. Above a temperature of about 150 K, water ice evaporates rather quickly due to the increase in vapor pressure, which can be estimated to be 6×10^{-8} mbar at 150 K [227]. Evaporation can also be influenced by the deposition method of the ice. Depending on the temperature, pressure, and cooling rate, different ice structures with different physical properties such as density and diffusivity emerge [228]. These properties can also change depending on the conditions after preparation, a process called annealing, which for example leads to recrystallization of amorphous ice at about 160 K. Whether different temperatures during sample preparation have a significant impact on the resulting ion spectra is not clear, and thus this parameter is usually not well controlled. Quite to the contrary, gradual surface evaporation at slightly elevated temperatures has previously been used to modify the ice film thickness or to remove overlayers of condensed low density ice [20]. For the analysis of thin samples, however, such continued evaporation could significantly limit the available measurement time. On the other hand, lower temperatures are believed to increase the ablation threshold because more energy needs to be dedicated to heating the sample to the phase transition temperature, as has been observed for UV-MALDI [229] and sub-ambient IR-LDI [94].

In the implementation used here, the sample mount was cooled to (roughly) the boiling temperature of liquid nitrogen (LN_2) of 77 K. LN_2 from an external dewar was channeled through a copper cold finger / heat reservoir placed close to the sample mount assembly, as can be seen in fig. 4.2. Flexible copper braids (not shown in the image) connected this

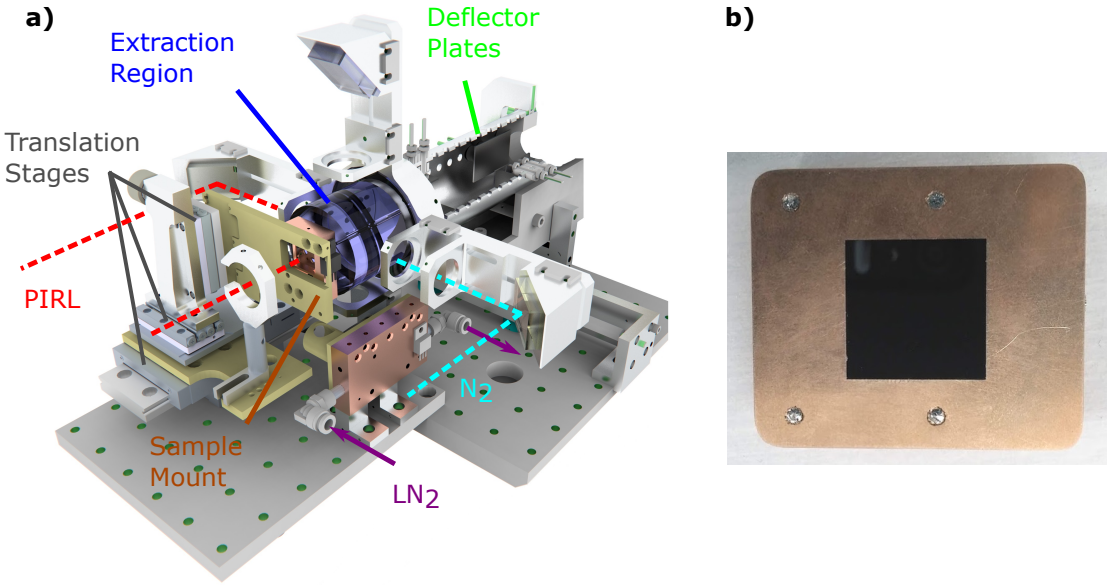

Figure 4.2: a) CAD rendering of the sample mount and extraction region. The laser beam paths for the PIRL in front and back ablation and for the N_2 laser are annotated in red and turquoise, respectively. Mirrors and lenses are mounted on arms extending into four directions from the extraction region. The cold finger located below the sample mount was connected to the mount using copper braids (these are not shown). b) The sample holder could be transferred into the vacuum chamber using a rotary/linear feedthrough arm and locked into place with a docking mechanism. It held the sample substrate, here a silicon chip, firmly in place and exhibited a flat surface so as not to disturb the electric field lines.

part to the sample mount, which thus shared both the same temperature as well as the electric potential. The temperature of the sample holder was measured with an attached thermocouple which was electrically insulated via a sapphire block, although this had to be removed during the actual measurements because electrical breakdown occurred. The cold finger was electrically and thermally insulated from ground by several centimeters of polyether ether ketone (PEEK) tubing which supplied the LN_2, and PEEK feet which held the part in place. This way, all tubing was fixed, reducing the risk of LN_2 leaks.

The sample mount was installed on top of a set of nanometer-precision piezo translation stages (SLC Series, SmarAct, Germany) by means of an insulating PEEK adapter. These stages allowed for accurate positioning compatible with high-resolution MSI. A through-hole about the size of the sample allowed for transmission geometry laser ablation and for easy alignment of the setup along a laser pointer. The sample itself was inserted into a copper holder outside the vacuum chamber, which is shown in fig. 4.2b. For sample transfer, the holder was attached to a magnetically coupled rotary/linear feedthrough (420MDM040-0750, Pfeiffer-Vacuum, Germany) with a PEEK adapter for insulation. The sample holder on

the tip of the feedthrough arm was then inserted into the load-lock and a quick vacuum connection was made via KF-type flanges. These have shown to be very useful for flanges that had to be frequently opened, which was why even the large flanges on the front and back of the TOF chamber were adapted so they could be shut with rubber seals instead of the usual CF-type mechanism. Rubber seals were quicker to fix, they were reusable, and they did not deteriorate the excellent vacuum quality which reached pressures down to 2×10^{-8} mbar. After pump-down, the arm was pushed through towards the sample mount, and a quick-lock mechanism allowed for the transfer and fixation of the holder into the mount by simply turning the feedthrough arm. This resulted in reproducible positioning with guaranteed electrical and thermal contact, while at the same time putting minimal strain on the piezo translation stages. Final sample tilt was determined to be well within $\pm 1°$ by observing the reflection of an alignment laser, positioned at the other end of the flight tube, from a mounted silicon wafer. This method was also used to align the assembly with the flight tube. A slight shift in angle was nonetheless observed when moving from one edge of the sample to the other.

The load lock featured a separate scroll pump, turbomolecular pump, and vacuum gauge so that high vacuum conditions could be reached within under a minute. During sample loading it was purged with nitrogen gas to avoid condensation on the frozen sample surface. One approach to avoid condensation of ambient humidity during sample preparation which was still being tested included a mobile vacuum chamber, or "vacuum suitcase", which allowed the transport of the sample holder from the preparation site to the mass analyzer under high vacuum conditions, including continuous sample cooling. A simpler solution was used for the experiments with cryo-samples presented here: sample preparation was performed directly in front of the load lock and inside a glove bag which was purged with dry nitrogen.

4.1.2 The Ion Source

The ion extraction region not only needed to provide access for the laser and camera optics, it also played a key role in the generation and collection of ions produced by laser desorption ionization. The initial source design was based on a classical Wiley-McLaren geometry [230, 231], consisting of two flat grid electrodes placed at distances of $d_1 \approx 1\,\text{cm}$ and $d_2 \approx 1\,\text{cm}$ from the sample plane, as is shown in fig. 4.3a. Following acceleration in this two-stage extraction region, the ions traversed a $D \approx 1\,\text{m}$ field-free drift region before impinging on the detector. The total flight time $t = t_1 + t_2 + t_D$ through all three regions

can be estimated from the equations of motion as

$$t_1 = \frac{v_1 - v_0}{a_1} \text{ with } v_1 = \sqrt{v_0^2 + 2a_1(d_1 - x_0)} \tag{4.1}$$

$$t_2 = \frac{v_2 - v_1}{a_2} \text{ with } v_2 = \sqrt{v_0^2 + 2a_1(d_1 - x_0) + 2a_2 d_2} \tag{4.2}$$

$$t_D = \frac{D}{v_2}\,, \tag{4.3}$$

where $a_i = -Q\Delta U_i/d_i m$ is the acceleration of an ion with mass m and charge Q in a homogeneous electric field in region i with a voltage difference ΔU_i over a distance d_i. A spread in arrival time is observed because of different initial ion velocities v_0, and variations in the point of ion creation x_0. Initial ion velocities in MALDI have been measured to amount to several hundred meters per second, but are typically below 1000 m/s [93, 231]. A spread in initial ion position can be caused by sample tilt, irregular surface morphology (e.g. large MALDI crystals), or removal of sample with consecutive shots. Especially in IR-MALDI, where the per-shot ablation volume is large, significant distributions of x_0 can be expected even for a single laser pulse. The use of the two-stage extraction region allows for a compensation of this position spread by varying the magnitude of the acceleration potential in the first acceleration region while leaving all other parameters, including the total acceleration potential, constant. Based on the flight distances, the optimum ratio $G^2 = (\Delta U_1 + \Delta U_2)/\Delta U_1$ of the total acceleration voltage to the one in the first region can be estimated numerically (to first order) from the relation

$$0 = -G + \frac{d_2}{d_1}\left(\frac{1-G}{1-G^2}\right) + \frac{D}{2d_1G^2}\,, \tag{4.4}$$

although fine tuning of this value is typically necessary during the experiment. Much better mass resolution can be obtained if, in addition, the initial velocity spread is compensated. This can be achieved by use of a reflectron or ion mirror, in which the ions are reflected eletrostatically: because faster ions penetrate deeper into the decelerating electric potential, they traverse a longer distance than slower ions. When adjusted correctly, the velocity focus, which is the plane at which the fast and slow ions arrive simultaneously, is placed onto the detector. However, because some amount of ions will fragment during their flight through the mass analyzer due to the internal energy they acquired during ionization (i.e. post-source decay of ions in metastable energy states), and because a conventional reflectron introduces additional (lossy) grid electrodes, such a design usually has a lower sensitivity. Alternatively, the ion extraction field in the ion source can be pulsed, a technique known as delayed extraction (DE). There, the ablation plume is allowed to expand for several hundred

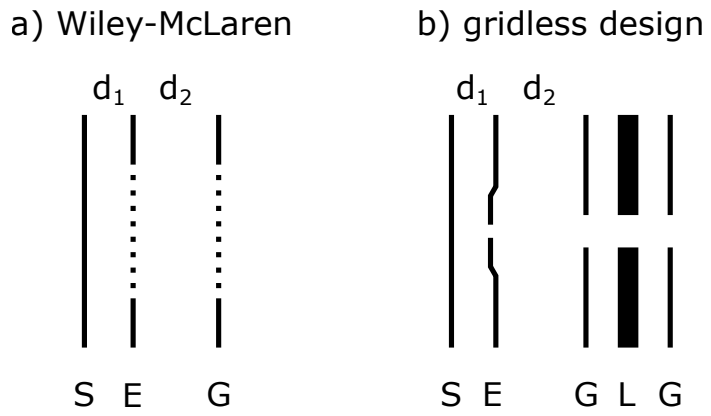

Figure 4.3: a) A two-stage extraction region of the Wiley-McLaren type was used initially to achieve space-focusing. b) It was replaced by a gridless design which introduced less transmission losses and left room for the laser and camera optics. Two extraction regions and an Einzel lens were formed by the sample surface (S), the extraction electrode (E), two grounded apertures (G) and the lens electrode (E).

nanoseconds without an applied field, such that initially faster ions will be accelerated over a shorter distance once the field is switched on, again producing a velocity focus. As an additional benefit, this field-free expansion has been shown to reduce energy loss and fragmentation due to in-plume collisions, which can increase both the ion yield and the mass resolution [231]. As a consequence, the ablation under DE conditions can be performed at higher laser fluences, which would otherwise lead to very dense plumes and significant peak broadening under continuous extraction. However, while the electrostatic focusing performed in the two-stage extraction and reflectron design are mass-independent, delayed extraction only focuses ions in a certain mass range, depending on the delay time and field strengths.

The results presented here were performed in a linear TOF design and under continuous extraction. A flat front surface of the sample holder extending beyond the sample area was desirable to keep the extraction field well defined. Figure 4.2b shows the holder used here. Most notably, there were no protruding screws or indentations on the front side. To achieve this, the coverplate was mounted on top of the 18 mm × 18 mm silicon target by tightening four nuts from the backside of the holder, using four bolts welded to the coverplate.

A simple source design was chosen here to be able to concentrate on the underlying physics of ablation and ionization, without obfuscating results by an unnecessarily high number of parameters. This way, the ion yield for different sample preparations and laser fluences could be determined more directly. However, the simple two-grid extraction region was replaced with a gridless design based on that of the commercial Bruker machines, which is schematically depicted in fig. 4.3b. This had several advantages: a gridless design helped

to avoid losses due to scattering at the electrode, and also focused the ion beam early on so that better collimation could be achieved. Besides the inherent lensing effect of the gridless acceleration, an Einzel lens was included in the design to control the amount of beam collimation. The new design also made sure that proper alignment could be ensured with the help of an alignment laser, i.e. several removable pinholes were included along the flight path. Most importantly, the new design featured access points for two lasers and a camera, so that experiments could also be performed in the more conventional front-ablation geometry.

4.1.3 Laser Coupling and Synchronization

IR-compatible viewports for the vacuum chamber were made either from uncoated CaF_2 (35 mm clear aperture, LaserOptex, Beijing, China) or from uncoated sapphire (24 mm clear aperture, Pfeiffer Vacuum, Germany). All lenses were chosen to be calcium-fluoride (CaF_2), usually anti-reflectance coated to minimize reflection losses. The PIRL pulse energy could be attenuated using a variable neutral density filter mounted on a manual micrometer precision translation stage.

For the conventional front ablation, the laser was focused onto the sample plane at an angle of about 35° through corresponding holes in the extraction electrodes, using a planoconvex lens with 1 ” diameter and $F = 75$ mm. Optimal focus conditions were established by manually moving the lens while observing the plasma created on a metallic target. Back ablation was performed with an identical lens, but a slightly smaller focus was achieved because here the beam hit the target orthogonally. In this geometry, optimization of the lens position along the beam axis was performed during the experiment by moving the z-axis translation stage onto which the lens was mounted until the best ion yield was achieved.

The infrared laser (PIRL-III-ND, Light Matter Interaction Inc., Canada) was controlled via its trigger input (setting ”Pedal ON”) by sending a 980 ms TTL signal (transistor–transistor logic) for each requested laser pulse. The PIRL would fire a single pulse during this window most of the time, except in about 2 % of cases in which no pulse was emitted due to the desynchronization of the TTL signal with the laser's 1 kHz clock. The exact timing of the pulse was determined by capturing stray light passing through the final mirror inside the laser on a fast photodiode, as described for the imaging experiments in the previous chapter. the photodiode then triggered a delay generator (SRS DG645, Stanford Research Systems, USA) which was set to produce a 1 µs TTL signal with zero delay to trigger the digitizer. This way, no mechanical shutter was required, but the trade-off was that the trigger signal was only available some time after the laser pulse occurred, a condition which worked here

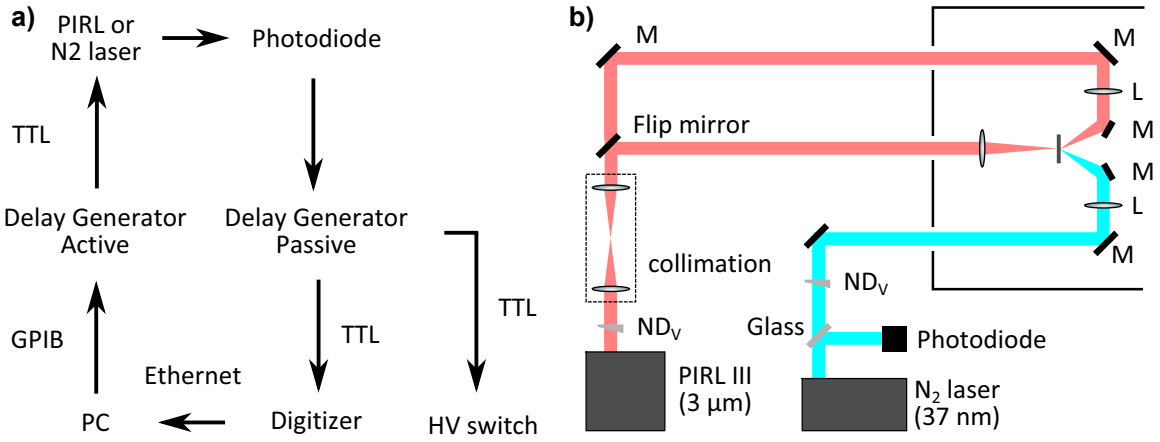

Figure 4.4: Laser coupling and synchronization. a) The lasers were controlled via TTL signals from a first delay generator. A second delay generator was used to distribute the exact timing information of the laser pulse obtained from a fast photodiode. b) Beam paths for front and back ablation using the PIRL or the nitrogen (N_2) laser.

but would not have worked for the plume imaging experiment. The additional delay and jitter introduced between the PIRL's photodiode trigger signal and the delay generator's trigger output was determined to be (106.85 ± 0.15) ns using an oscilloscope, demonstrating that the accuracy of the TOF measurement was not adversely impacted. In contrast, the original PIRL trigger output delivered a TTL pulse with about 112 µs delay, too late to trigger subsequent electronics. Further devices, for example for deflector pulsing, could be triggered from the delay generator if needed. The communication pathways between devices are summarized in fig. 4.4a.

The laser beam path is depicted in fig. 4.4b. Beam divergence was controlled with a $F = 1000$ mm lens at the laser output and a telescope assembly including two $F = 100$ mm lenses. The pinhole which was used for spatial filtering in the plume imaging experiments presented earlier was not used for the results shown in this chapter, mainly because the high laser fluence in the laser focus frequently damaged the pinhole. It was also realized that although a more homogeneous beam profile would make the results more comparable to other labs, it would not necessarily improve the mass spectrometric performance significantly. Indeed, the N_2 laser commonly used for MALDI has a very irregular beam profile, which is also emulated by e.g. the Bruker SmartBeam technology [232]. A flat-top profile would nonetheless be desirable for fundamental studies with a conventional laser spot size in the range of 100 µm. This has previously been achieved for mid-IR laser ablation by guiding the beam through a multi-mode fiber and projecting the image of the output facette onto the sample surface using a telescope assembly in infinite conjugation, which achieved a flat, 175 µm diameter focus at 25 mm working distance [233]. However, attempts to reproduce

this design here failed because the resulting laser fluence did not reach the required value. On the one hand, a very irregular PIRL output beam profile hampered efficient fiber-incoupling: at full laser power and sufficiently small input focus, the fiber facette would be damaged, whereas with larger focus diameters, damage would incur to the surrounding fiber cap or cladding. On the other hand, a large core diameter in combination with a large output numerical aperture of the fiber and the design limitations of the ion source in terms of the minimum focal distance of the focusing lens led to an unreasonably large focus diameter. This was especially significant for the front ablation geometry in which the distance between the focusing lens and the sample plane was limited to above 5 cm. In conclusion, the approach appeared unsuitable for high-resolution ($< 10\,\mu m$) mass spectrometry imaging, given that the large fiber core diameter and numerical aperture inherently limited the achievable minimum focus diameter.

As a reference, UV-MALDI spectra could be acquired with an N_2 laser (MNL 800, Lasertechnik Berlin, Germany) emitting at 337 nm. In this case, the delay generator was also triggered from a fast photodiode (DET10 A/M, Thorlabs) which picked up the reflection from a beam-splitting glass window as seen in fig. 4.4, and which would in turn trigger the digitizer and other devices. The laser could either be controlled by the provided software or by a TTL trigger input similar to that used for the PIRL. Attenuation was again achieved with a variable ND filter. The laser entered the vacuum chamber through a UV fused silica viewport (35 mm clear aperture, Pfeiffer Vacuum, Germany) where it was focused onto the sample plane in frontside ablation using a planoconvex $F = 100$ mm uncoated N-BK7 lens at an angle of about 35°, roughly mirroring the PIRL geometry.

For each laser focus, it was ensured that the ablation crater overlapped with the intersection of the TOF axis and the sample plane. Because the extraction electrode of the Bruker ion source was a pinhole with approximately 1 mm diameter, deviations of already a few hundred micrometer lead to significant losses in ion yield and mass resolution.

4.1.4 Ion Detection

The spectra presented here were acquired with a flange-mounted dual-stage microchannel plate (MCP) detector assembly (Hamamatsu F9890 with F1552-011G), which offered an effective diameter of 27 mm, a minimum pulse width of 350 ps, a gain of $\approx 10^6$, and low ringing noise due to the integrated signal decoupling electronics. A 20 dB preamplifier with 1.8 GHz bandwidth (TA1800B, fastcomtech, Germany) positioned in close proximity to the MCP was used to extract the detector signal. This allowed for the MCP to be operated at lower voltages, which reduced detector saturation and increased detector lifetime. It also

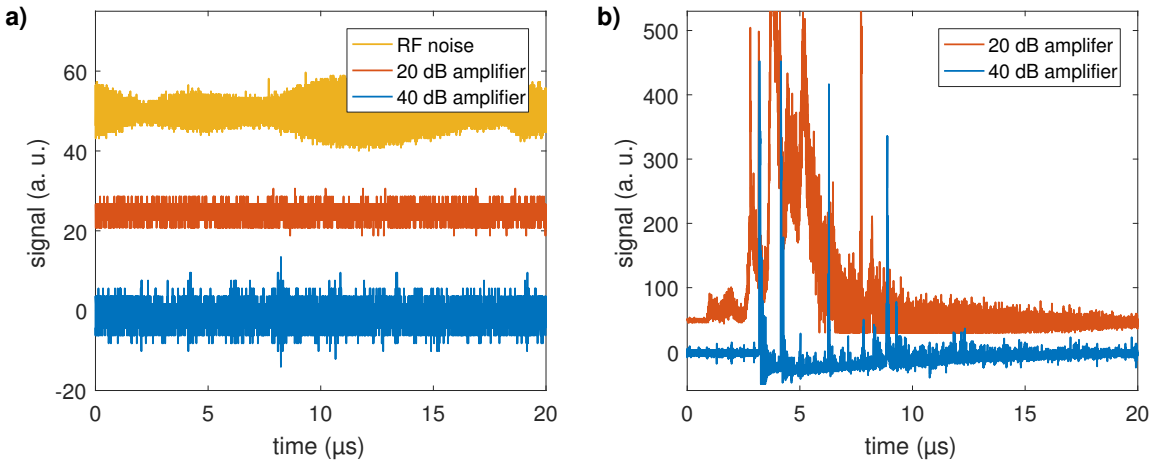

Figure 4.5: Detector response for different amplifications. a) Noise pickup at specific frequencies would be well visible with the 40 dB amplifier, but not at 20 dB. Individual acquisitions would be overshadowed by extensive RF noise. b) Two examples of detector saturation: notice the clipping and baseline-drop.

reduced the detrimental influence of additional capacitance and noise-pickup that the longer cable connection to the digitizer would otherwise have introduced. Spectra were recorded at 1 GHz sampling rate with an 8 −bit digitizer (Acqiris DC211, Agilent, USA). The digitizer offered a higher sampling rate up to 4 GHz at 1 GHz bandwidth in anticipation of a higher mass resolution in future studies.

Figure 4.5a shows three examples of the noise baseline, acquired as single spectra without ion signal. The blue curve was recorded using a 40 dB (×100) amplifier (HSA-Y-1-40, Femto, USA) and shows relatively large (≈ 20 mV) spikes which occurred at a fixed frequency, on top of smaller ripples with ≈ 10 mV amplitude. The ripple disappeared when the MCP power supply was turned off, indicating that this was caused either by instabilities in the HV supply voltage or by detector noise. The larger spikes, however, persisted, and were thus most likely caused by RF ground noise. Both those sources were difficult to tackle, which is why a smaller amplification of 20 dB was chosen instead, with conversely larger MCP voltages. As shown by the orange curve in fig. 4.5, the spikes and ripple were not visible under these conditions, and the noise was mainly determined by the digitizer. However, some spectra were overshadowed by severe trains of RF noise as shown in the yellow curve, most likely due to cellphone signals.

Figure 4.5b shows two examples of saturated spectra recorded with the hardware described here. The largest signals were followed by broad tails, and the oscillatory behavior was well visible for the 40 dB amplifier for which the signal sharply spiked below the baseline. The spectra were also clipped at 480 mV due to the digitizer settings, for which a range from

−20 to 480 mV was chosen to yield a resolution of roughly 2 mV. Severe saturation could in addition distort the signal baseline and diminish subsequent signal amplitudes on a timescale of several 10 µs. Signal depletion by abundant ion species in the low-mass region such as salts or metals was a major hindrance to detecting peptides and proteins in the high-mass region, especially when high laser fluences were used. A mass filter was thus implemented to remove these low-mass ions by deflecting them with a high voltage pulse to a pair of deflection plates positioned roughly 15 cm after the extraction plate. Typically, one plate was kept at ground and pulsed to 500 V for a time window starting with the laser pulse and lasting for several hundred ns by using a high voltage solid state pulser (PVX-4140, Directed Energy Inc., USA). The other plate could be used to steer the ion beam for optimal signal detection.

The MCP was driven by a computer-controlled high precision high voltage supply (EHS 80 40, iseg, Germany) which could automatically ramp the voltage up and down at a specified rate. For the measurements presented here, the front plate, back plate, and anode voltage were set to −2, 1450, and 1700 V, respectively. The ion optics were connected to a power supply with slightly less resolution and more ripple (Ultravolt, USA), but with manual turn knobs which simplified the device calibration. Sample plate, extraction electrode, flight tube, and Einzel lens setting were typically 16, 15.2, 0, and 9 kV, respectively.

4.2 Sample Preparation

The sample preparation procedure was crucial to achieve reproducible ion signal. A variety of different protocols were tested over the course of this work, although only a subset of techniques was used for recording the data presented in section 4.3. Many of the initial experiments were centered around UV-MALDI because this was a known technique that could be used as a reference standard. It also allowed to perform initial device testing and optimization without sample cooling. Frozen samples were only investigated after UV- and IR-MALDI were shown to work as expected.

For all techniques, the analytes angiotensin I human acetate salt hydrate (≥90 % (HPLC), A9650), vitamin B12 (cyanocobalamin, ≥98 %, V2876, Sigma), human insulin, and lysozyme from chicken egg (≥90 %, L6876) were used as obtained from Sigma Aldrich. Angiotensin I was prepared as a 1 mM stock solution and stored at −20 °C. The final analyte solutions were stored at room temperature and were used within a week.

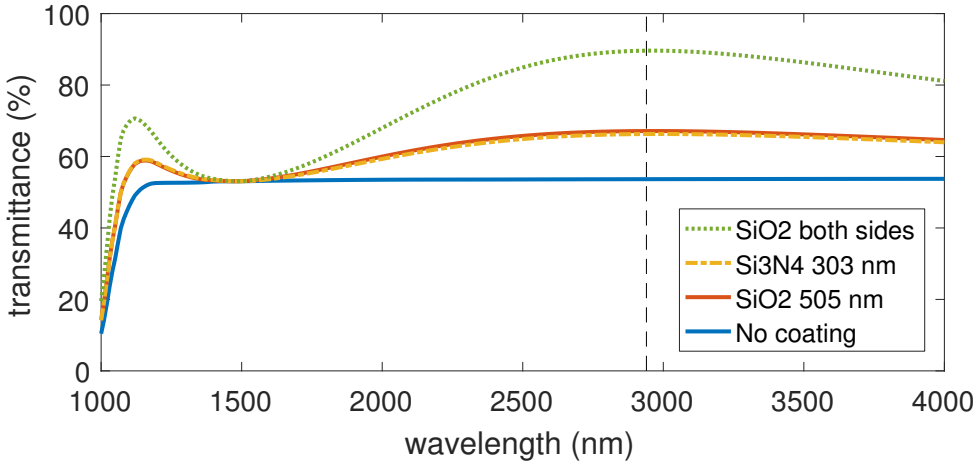

Figure 4.6: Transmission spectra including reflective losses of 500 µm thick silicon wafers calculated using OpenFilters. Coating thicknesses for silicon oxide and silicon nitride are optimized for 2.94 µm, and this wavelength is marked with a grey dashed line.

4.2.1 Transparent Sample Substrates

The instrument allowed for front-side as well as back-side ablation. Hence, a sample substrate had to be identified which was transparent at 3 µm wavelength but also electrically and thermally conductive. Indium tin oxide (ITO) coated fused silica wafers are commonly used in transmission geometry MALDI [139] and mass spectrometry imaging [234], as these are transparent both in the UV and the visible wavelength range. This allows not only for back-side laser ablation, but also for high-resolution light microscopy with backside illumination. ITO slides (06478-AB, 2spi, USA) with a sheet resistance of 70 to 100 Ω/sq were used for some of the presented UV-MALDI experiments.

Unfortunately, ITO is opaque for wavelengths above 2 µm, so a different substrate had to be found for DIVE. Transmission electron microscopy (TEM) grids have been used for MSI before [235], but, especially for thin samples, the metal grids can be expected to lead to field enhancement which locally increases the laser exposure and leads to uneven irradiation conditions. It was also not clear if the field lines close to such a grid were sufficiently homogeneous for efficient ion extraction. Finally, it has been shown that metal surfaces lead to significant low-mass background in IR-LDI [46–48], most likely due to plasma generation or excessive heating of the metal surface. This was also observed for the TEM grids briefly tried here. Ablation from silicon, which is transparent at 3 µm, on the other hand, produced spectra in which this low mass background was strongly reduced or even absent.

The optical transmission of silicon was plotted in fig. 4.6 using the software OpenFilters[1].

[1]Software available at www.polymtl.ca/larfis

Doping	Thickness (µm)	Resistivity (Ω cm)	Transmittance (%)
p-type (Boron)	360	0.001-0.005	0.3
p-type (Boron)	360	0.01-0.05	34
p-type (Boron)	525	0.1-1	47
n-type (Phosphor)	300	0.1-1	54
p-type (Boron)	380	1-10	56
p-type (Boron)	380	20-100	54
Si_3N_4 coated	380	1-10	98

Table 4.1: Resistivities of several doped silicon wafers as stated by the manufacturer, and their optical transmission at 3 µm wavelength measured with the PIRL-III. The coated wafer was p-type (Boron) with 300 nm silicon nitride on each side (conductivity applies only to the silicon substrate).

It is rather wavelength independent over a broad range in the mid-IR, with a transmission of about 54 % for a 500 µm thick wafer in vacuum. Because the losses are mainly caused by reflection at the interface, the transmission can potentially be improved by applying an anti-reflective coating. A straightforward solution would be to deposit about 500 nm of silicon dioxide (SiO_2) or 300 nm silicon nitride (Si_3N_4) to one side of the substrate. This would raise the transmission by about 13 percent. Up to 90 % transmission can be achieved when both sides are coated, but of course this would negatively impact the electrical and thermal conductivity of the substrate.

Better electric conductivity of silicon can be achieved by doping. This has two effects: on the one hand, the introduction of impurities effectively reduces the material's band-gap, slightly shifting the critical wavelength below which the material is strongly absorbing via interband transitions towards longer wavelengths. However, this shift is small and the band-gap for pure silicon corresponds to a wavelength of about 1 µm, so that the absorption for mid-IR wavelengths is not significantly impacted. On the other hand, a smaller bandgap results in a larger population of thermally excited electrons in the conduction band (or holes in the valence band), so that the free-carrier absorption via intraband transitions increases. This increase in optical absorption for each increase in electric conductivity meant that a trade-off between transmission and conductivity had to be achieved. Several samples with resistivities between 0.001 and 100 Ω cm (MicroChemicals, Germany), corresponding to sheet resistances between 0.03 and 3000 Ω/sq, were placed in the PIRL beam to measure their transmittance in normal incidence, as is shown in table 4.1. The measurements had a relative uncertainty of ±5 %. The phosphor-doped wafer with a resistivity of 0.1 to 1 Ω cm (3 to 30 Ω/sq) showed the best conductivity at near-maximum transmission and was chosen as the substrate for the DIVE measurements.

4.2.2 MALDI Samples

MALDI samples were prepared using the standard dried droplet approach [236], in which the analyte solution is mixed 1:1 with a matrix solution before a small volume of the mixture (typically 0.5 to 1 µL) is applied to the substrate and left to dry. For most measurements, 2,5-dihydroxybenzoic acid (DHB) was used as a matrix compound (>99.0 % (HPLC), 85707, Sigma), as it is suitable for MALDI-TOF analysis of a wide variety of peptides and proteins. A 90:10 mixture of 2,5-DHB and 2-hydroxy-5-methoxybenzoic acid (MBA), known as super DHB (sDHB), was used in some experiments and showed improved crystal formation, which led to an increase in signal strength and reproducibility. Matrix solutions were prepared at 20 mg/mL in a mixture of 30 % (v/v) acetonitrile and 70 % water with 0.1 % trifluoracetic acid (TFA).

4.2.3 DIVE Samples

Samples of frozen droplets of the analyte solution were prepared in a glove bag (108D S-20-20H-6, Glas-Col, USA) attached to the load lock of the mass analyzer. A dewar with a small amount of liquid nitrogen was placed inside the glove bag, and the bag was additionally flooded with dry nitrogen gas. This way, the remaining humidity in the bag was lowered to a few percent, as measured by a hygrometer (HT-100, Voltcraft, Germany). Small drops (typically 0.5 to 1 µL) of the sample solution were placed on a substrate already mounted in the sample holder. The holder was then transferred into the glove bag and slowly cooled down by holding it over the LN_2 surface, repeatedly dipping the holder into the nitrogen until the droplets were frozen solid. Direct contact of the droplets with the liquid nitrogen was avoided to prevent contamination and dilution of the sample (e.g. by condensed ambient humidity in the LN_2 dewar). Performing the cooling too quickly often led to cracking of the droplets which would then break off the substrate surface. After the droplets had frozen, the holder was partially submerged until it reached the liquid nitrogen temperature. The sample holder was quickly transferred to the load lock using the linear/rotary feedthrough arm with a KF seal as described above, and the scroll and turbomolecular pumps were turned on immediately.

4.3 Results and Discussion

The results shown in the first part of this section serve to highlight key measurements performed to test and optimize the mass analyzer and laser settings, and to provide reference measurements for the investigation of DIVE from frozen samples. They also lend themselves

to familiarize the reader with the data analysis and presentation throughout this chapter. Measurements of IR-LDI from frozen solutions will be presented in the second section.

Many of the spectra were converted to show the signal amplitude as a function of the mass-to-charge (m/z) ratio. It can be easily seen from eqs. (4.1) to (4.3) that the total flight time of an ion with mass m and charge $Q = ze$ (where e is the electron charge) can be written as

$$t(v_0 = 0) = A\sqrt{\frac{m}{z}} + t_0 \tag{4.5}$$

if the initial velocity v_0 is neglected. The value of A is fully determined by the device distances and voltages. Although a more accurate model including a linear term in m/z to account for the initial velocity [231] was tried out for the mass calibration, it did not significantly improve the results, and the simple model was chosen for all spectra presented here. Depending on the spectrum, a number of known peaks were identified and used as calibration standards. The most common peaks included sodium (Na^+), potassium (K^+), the matrix peaks[2] and the (quasi-) molecular ion. A nonlinear fit of the peak positions then gave the calibration constants. In case it was not clear a priori whether the molecular ion (M^+) or a quasi-molecular ion (e.g. $[M + H]^+$) was formed, several fits with different adducts were performed and the one with the lowest residual selected.

Values for the laser pulse energy are given as measured at the sample position. They were typically measured at a reference position and converted to the specified value by a previously calibrated reference measurement. Fluence values will not be given because the exact laser focus size inside the vacuum chamber was not determined (spatial constraints prevented the use of a conventional beam analyzer). Ablation craters were observed to be about 20 µm × 80 µm in size for UV front ablation, and to have a diameter of about 270 µm in IR front ablation, but numbers would vary with the applied pulse energy.

4.3.1 UV- and IR-MALDI

The electric potentials for acceleration, collimation, and steering of the ion beam had to be optimized. The deflector voltages were adjusted to give the highest ion yield for readily observable substrate or MALDI matrix peaks, and were usually set to values within ±100 V. The ion lens voltage for the lens included in the extraction assembly did not have a large effect when kept at similar values to that known from a similar commercial machine, and was later optimized to 7.5 kV by observing the strength of the parent ion peak. The potential U_1 of the extraction electrode was varied to find the space focus conditions described in section 4.1.2, while the total acceleration potential was kept constant with the source at

[2] MALDI spectra of common compounds can be found at www.massbank.eu.

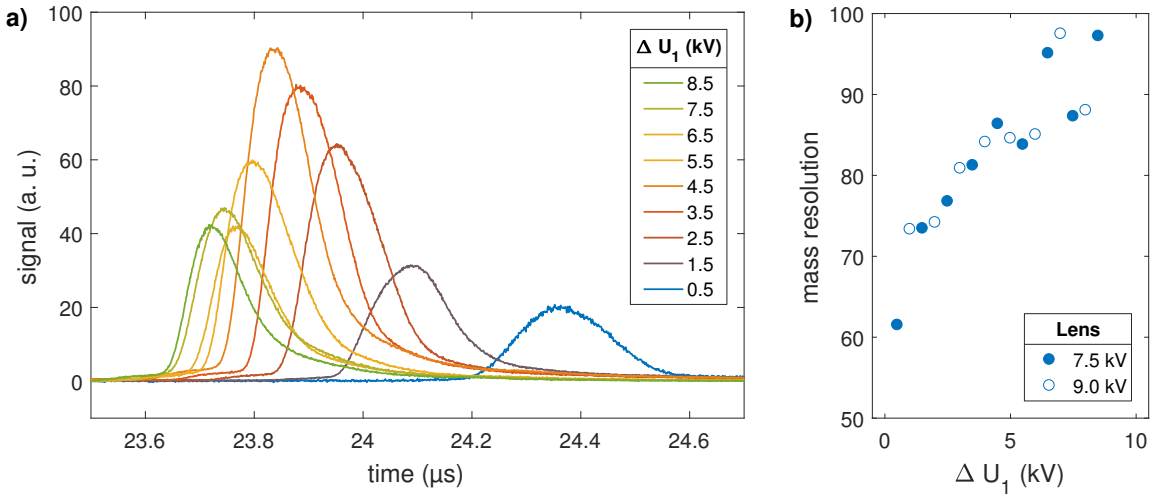

Figure 4.7: The extraction potential was varied to find the space focus conditions. The sample was held at 16 kV. a) Larger electric potentials reduced the field strengths in the extraction region, causing the arrival time to shift to longer times. b) A local optimum in mass resolution was found at about 11 kV extraction electrode potential. Spectra are averaged over about 500 laser shots (140 for the measurement at 15.5 kV).

$U_0 = 16\,\mathrm{kV}$ and the drift tube at $U_2 = 0\,\mathrm{kV}$. Figure 4.7a shows a close-up of the arrival time distribution of the angiotensin I quasi-molecular ion peak $[\mathrm{AngI} + \mathrm{H}]^+$ for different potential differences $\Delta U_1 = U_1 - U_0$. The smaller the potential difference, the longer the time the ions spent in the extraction region, which lead to longer flight times t. The mass spectra were taken by raster-scanning over a dried droplet preparation on a stainless steel substrate, acquiring 20 shots per laser focus position. The different measurement grids (i.e. positions) were interleaved to keep the sample conditions such as crystal morphology and analyte concentration as stable as possible. Averaging was performed on each dataset containing 900 spectra, but acquisitions which did not reach a signal amplitude of 20 mV anywhere in the spectrum (at a digitizer range of 480 mV) were discarded to filter out sampling locations with improper matrix preparation or which were taken on the blank substrate. Panel b) shows an analysis of the mass resolution $R = m/\Delta m = t/2\Delta t$, where the peak width Δt was determined by taking the full width half maximum (FWHM) of slightly smoothed data. Based on eq. (4.4), the optimal extraction electrode potential was expected to be around 15.5 kV. It turned out that this approximation did not hold for the gridless ion optic design. In fact, no real maximum for the mass resolution was found, which kept increasing with increasing extraction field strength. This indicated a significant contribution of the initial ion velocity. A local maximum was identified at around $U_1 \approx 11\,\mathrm{kV}$, roughly two thirds of the total potential. This also gave the strongest ion signal at an Einzel lens voltage setting of 7.5 kV. While the lens voltage did change the extraction electrode potential at which

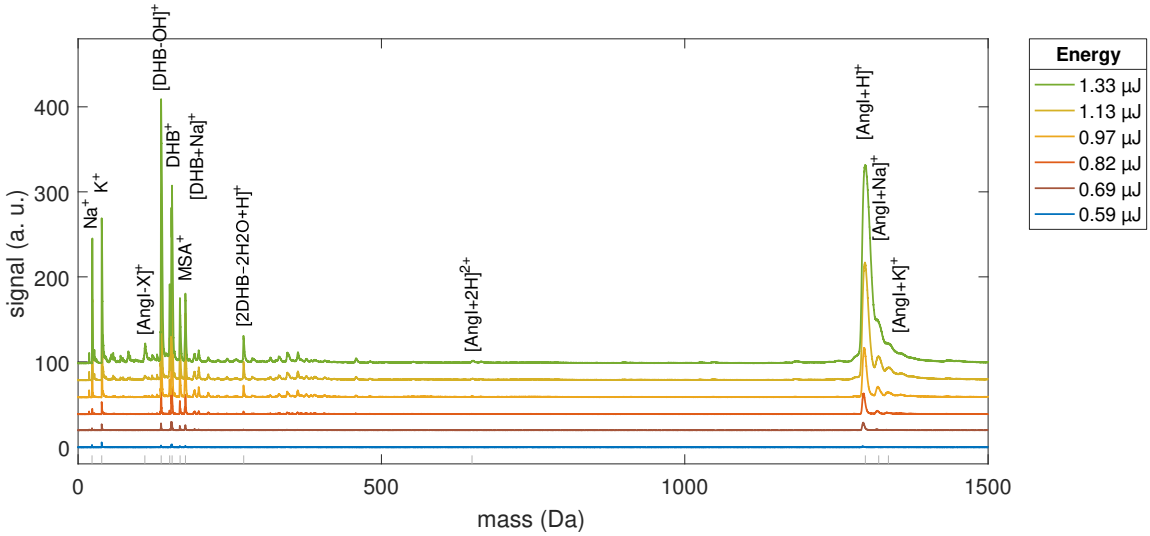

Figure 4.8: UV-MALDI fluence dependence of 100 µM angiotensin I in 0.1 % TFA with matrix sDHB, dried droplet preparation on stainless steel. The quasimolecular ion peaks for angiotensin I (AngI) including salt adducts (Na, K) were of similar amplitude as the matrix peaks for 2,5-dihydroxybenzoic acid (DHB) and 5-methoxysalicylic acid (MSA), which together form sDHB. Average of several hundred spectra.

the strongest signal was observed, it did not have a strong effect on the mass resolution, as can be seen for the mass resolution measurement at 9 kV lens voltage plotted with empty markers in fig. 4.7b. An extraction electrode voltage of 11 kV was used for all MALDI experiments presented in the following.

The observed ion signal depended strongly on the laser pulse energy, as can be seen in fig. 4.8. This figure shows the working range for samples of 100 µM angiotensin I in 0.1 % TFA with sDHB20. As described earlier, the sample was scanned using interleaved sampling positions, and averages were taken from spectra with a minimum amplitude of 5 mV. Each spectrum is shifted vertically to increase readability. The amplitude of the molecular ion peak as well as those of the background increased strongly with increasing pulse energy. At the highest pulse energy shown here, the analyte signal would frequently be clipped by the digitizer range. The effect was not compensated during data analysis, so the average was slightly underestimated and the peak width overestimated.

The most abundant peaks have been annotated and included sodium (22.99 g mol^{-1}, Na^+) and potassium (39.10 g mol^{-1}, K^+), which presumably were part of the matrix compound, the matrix peaks given by 2,5-dihydroxybenzoic acid (154.02 g mol^{-1}, DHB^+) and 5-methoxysalicylic acid (168.03 g mol^{-1}, MSA^+), and the quasimolecular ion peaks for angiotensin I (1295.68 g mol^{-1} plus adduct mass, $[AngI + H]^+$, $[AngI + Na]^+$, and $[AngI + K]^+$). Additional known matrix peaks were given by the protonated DHB ion ($[DHB + H]^+$), water loss

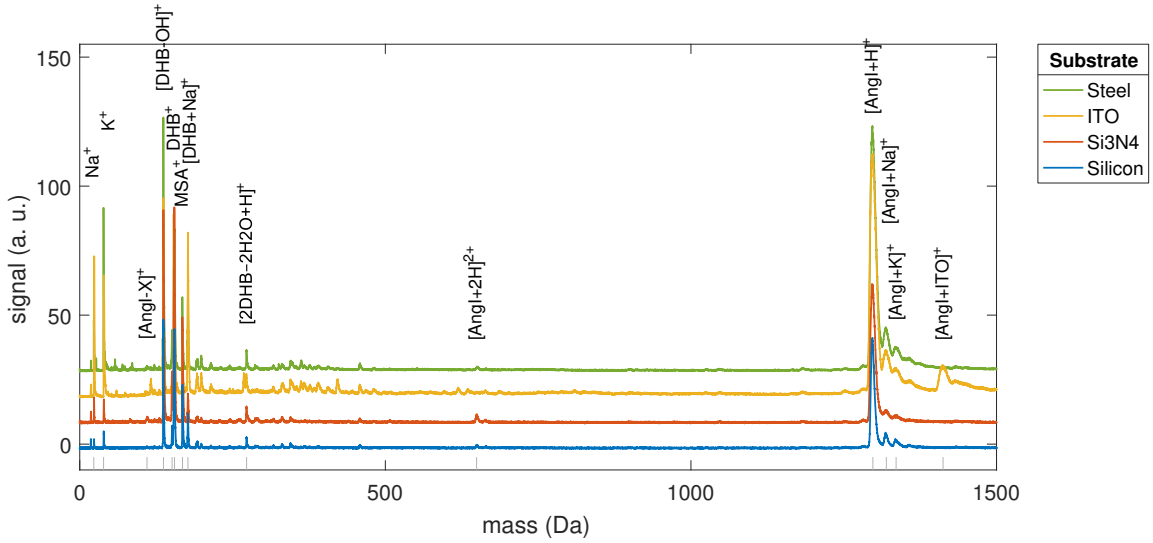

Figure 4.9: UV-MALDI spectra of 100 µM angiotensin I in 0.1 % TFA with matrix sDHB on different sample substrates at 1.13 µJ (for steel and ITO) and 1.33 µJ pulse energy (for silicon and Si_3N_4. Average of several hundred spectra.

from DHB ($[\mathrm{DHB} - \mathrm{OH}]^+$ or $[\mathrm{DHB} + \mathrm{H} - \mathrm{H_2O}]^+$, water loss from MSA ($[\mathrm{MSA} + \mathrm{H} - \mathrm{H_2O}]^+$), and matrix clusters ($[2\,\mathrm{DHB} + \mathrm{H} - 2\,\mathrm{H_2O}]^+$, $[\mathrm{DHB} + \mathrm{MSA} + \mathrm{H} - 2\,\mathrm{H_2O}]^+$). A known angiotensin I fragment ion at $m/z = 110$ (the histidine immonium ion) could also be observed and was labeled as $[\mathrm{AngI} - \mathrm{X}]^+$, as well as the doubly protonated angiotensin I ion ($[\mathrm{AngI} + 2\,\mathrm{H}]^{2+}$). The exact mass of each peak was annotated by a grey tick mark on the bottom of the figure axis, while the annotated text was sometimes shifted to better fit into the figure. The mass calibration was performed for the spectrum with the highest pulse energy. A slight shift towards earlier arrival times and an increase in mass resolution was observed for all peaks when using smaller pulse energies, an effect which was not compensated in this figure (later figures show mostly individual mass calibrations for all curves). This is especially visible for the angiotensin quasi-molecular ion peak and its adducts. Both effects were likely caused by an increase in the amount of ablated material and therewith the plume density, which caused larger energy deficits by ion-neutral collisions.

The same measurements were repeated on several different substrates. Stainless steel is the most common MALDI substrate and the standard sample preparation method can be assumed to have been optimized for this material. For many MSI studies, indium tin oxide (ITO) coated fused silica wafers are the substrate of choice because they are transparent in the visible and are thus easy to image in a conventional light microscope. They are also transparent in the UV so that they are suitable for the back ablation geometry. Doped silicon was of interest for the IR ablation experiments as it can be both optically transparent

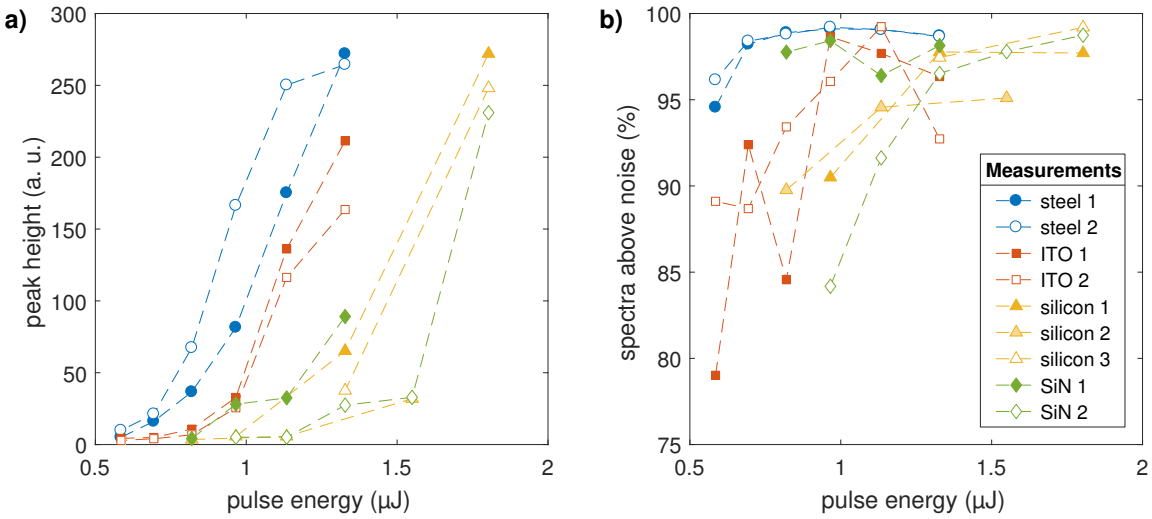

Figure 4.10: Analysis of the UV-MALDI fluence dependence of 100 µM angiotensin I in 0.1 % TFA with matrix sDHB, dried droplet preparation, on several substrates. Measurements on different substrates are shown in different colors. a) Average angiotensin I quasi-molecular ion peak amplitude. b) Fraction of spectra for which the quasi-molecular ion peak had a signal-to-noise ratio of 3:1 or above. The legend in panel b) is valid for both figures. The dashed lines serve as guides to the eye.

at 3 µm wavelength and electrically and thermally conducting. Finally, silicon nitride coated silicon wafers yield a higher IR transmission but are electrically insulating. As can be seen in fig. 4.9, the resulting spectra were very similar. This showed that the reduced electrical conductivity of the silicon and Si_3N_4 substrates posed no significant problem for ion extraction. Slightly reduced signal amplitudes were very likely caused by differences in matrix crystallization: on the non-metallic substrates, the analyte droplets did not spread out as far as on the metal surfaces which hindered proper crystal formation and resulted in a very dense sample layer. The spectra shown here were taken with an elevated fluence of 1.33 µJ, compared to 1.13 µJ for the spectra on the metal surfaces. Additional ion peaks could be observed for the ITO substrate, in particular the indium and tin adduct peaks (114.82 g mol^{-1} and 118.71 g mol^{-1}) for angiotensin I.

The fluence dependencies are summarized in fig. 4.10. Panel a) shows the average peak height of the molecular ion peak $[\mathrm{AngI} + \mathrm{H}]^+$ as a function of pulse energy for different measurements on steel, ITO, silicon, and silicon nitride. The increase in signal intensity was highly nonlinear as expected. A saturation effect was observed for measurement 1 on steel, possibly due to the signal amplitude exceeding the digitizer range on some acquisitions. While similar molecular ion signal intensities were seen on all substrates, steel required the lowest pulse energy and silicon nitride the largest. Again, this was most likely due to the change in sample morphology. Even between samples on identical substrates, significant

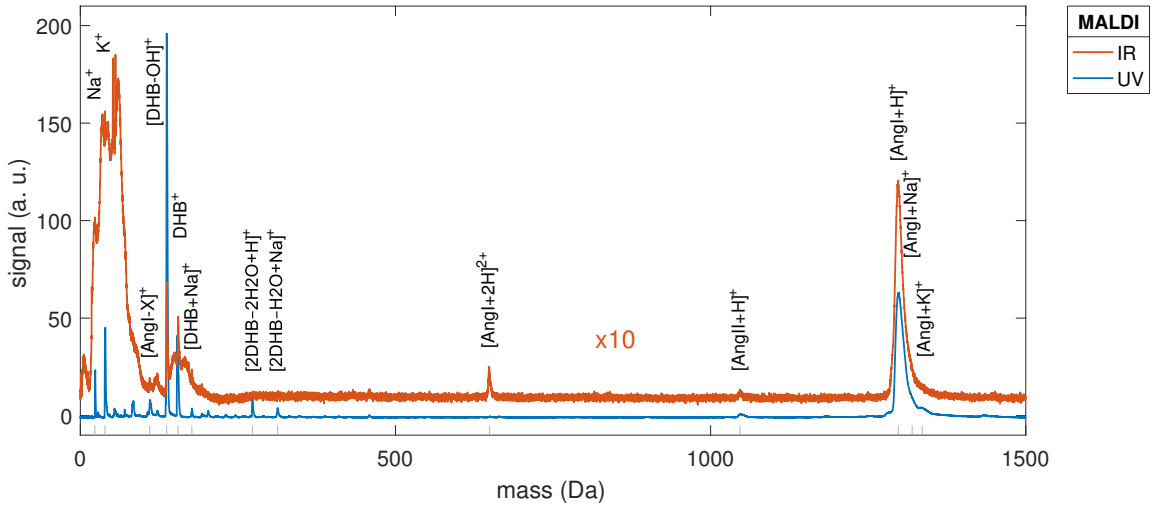

Figure 4.11: Comparison of UV- and IR-MALDI for 100 µM angiotensin I in 0.1 % TFA with matrix DHB on a doped silicon substrate. UV spectrum acquired at 1.8 µJ pulse energy (average of 900 spectra), IR spectrum at 56 µJ (300 spectra). The IR-MALDI spectrum (orange curve) is multiplied by a factor of 10 for better visibility.

fluctuations in signal quality were observed, which is why several measurements are shown here to give an impression of the distribution.

The measurement range for the laser pulse energy was chosen based on the visibility of the molecular ion peak during the experiment. A more quantitative criterion for the detection threshold is the requirement for at least half of the recorded spectra to exhibit a signal to noise ratio of 3:1 [233, 237]. The noise was determined as the standard deviation of the signal in the region between 15 and 22.5 µs where no significant ion peaks were expected, although unknown ion peaks caused some amount of chemical noise. To remove laser sampling positions with improper sample preparation, the fraction was computed not in relation to all recorded spectra, but relative to the amount of spectra that showed any signal above 5 mV. About 30 % of recorded spectra were typically discarded in this way, although this depended strongly on the sample preparation and selected region of interest. Figure 4.10b shows the fraction of spectra in which the molecular ion peak surpassed a signal to noise ratio of 3:1. According to this analysis, the detection threshold was slightly below the lowest pulse energy shown here. Still, the threshold determined without this more intricate analysis was fairly accurate.

IR-MALDI was briefly tried on DHB sample preparations, a matrix which is suitable both at UV and IR wavelengths [16]. Figure 4.11 shows spectra from a droplet of 100 µM angiotensin I in 0.1 % TFA with DHB on a silicon substrate, one recorded at 337 nm and one at 2.94 µm wavelength. The data quality for the IR spectrum was significantly worse, which

is why it is shown with a magnification of a factor of 10. It is likely that further optimization of the sample preparation and laser power could have improved the quality, as IR-MALDI spectra are usually known to be of similar quality than those from UV-MALDI, at least at moderate analyte concentrations. Of course, the greater per-shot sample consumption meant that less spectra could be acquired for each location on the sample surface, leading to slightly worse statistics. Another problem with the IR laser desorption was that the substrate-induced background in the low-mass region increased strongly with increasing laser power, and was almost always stronger than the molecular ion peak in case no deflection of low-mass ions was used. This lead to the signal exceeding the digitizer range in the low mass region at all fluences for which an analyte ion peak could be produced. The substrate peaks in the low-mass region have not been annotated as the spectrum was quite complex and confident peak identification would have required a better mass resolution to rely on the exact ion masses.

The UV spectrum shown here was acquired at rather high laser pulse energy (1.8 µJ), and showed some peaks not seen as clearly in the spectra presented before: the sodium adduct $[2\,\mathrm{DHB} - \mathrm{H_2O} + \mathrm{Na}]^+$ and the protonated angiotensin II peak (1045.53 g/mol plus adduct mass, $[\mathrm{AngII} + \mathrm{H}]^+$). Angiotensin II was possibly part of the analyte solution as an impurity or degradation product, as angiotensin I is only stable for about four days when kept in solution and was usually stored at room temperature. The IR spectrum was acquired at a pulse energy of 56 µJ, which translated to a fluence of roughly $0.2\,\mathrm{J\,cm^{-2}}$, keeping the much larger laser focus diameter in mind. This was in the same range as previously published threshold fluences [233]. The IR spectrum does not show the salt adduct peaks to the molecular ion typically observed for UV-MALDI. It was, however, not clear if this was a real effect or merely due to insufficient mass resolution or detection efficiency.

Finally, it was of interest to test the mass range of the TOF instrument. Ion peaks of heavier molecules are more difficult to resolve because, as has been extensively studied for MALDI [16], all ions are ejected with similar initial velocities. This means that heavier molecules, for which the nominal drift velocity is smaller at the same acceleration potential, show a broader distribution relative to this nominal value. Additionally, MCP detectors are sensitive to the ion velocity, not their kinetic energy, meaning that the detection efficiency drops off significantly above about 1 kDa for the rather low acceleration potential used here [238]. This usually means that larger threshold fluences are observed for larger molecules. Figure 4.12 shows spectra from two samples, one containing 100 µM insulin (5733.55 g/mol), the other 100 µM lysozyme (14 307 g/mol), both in 0.1 %TFA with DHB on doped silicon. The bottom two curves were recorded using the N_2 laser, the upper two curves with the PIRL. Except for the again lower data quality for IR-MALDI, the spectra look very similar. The

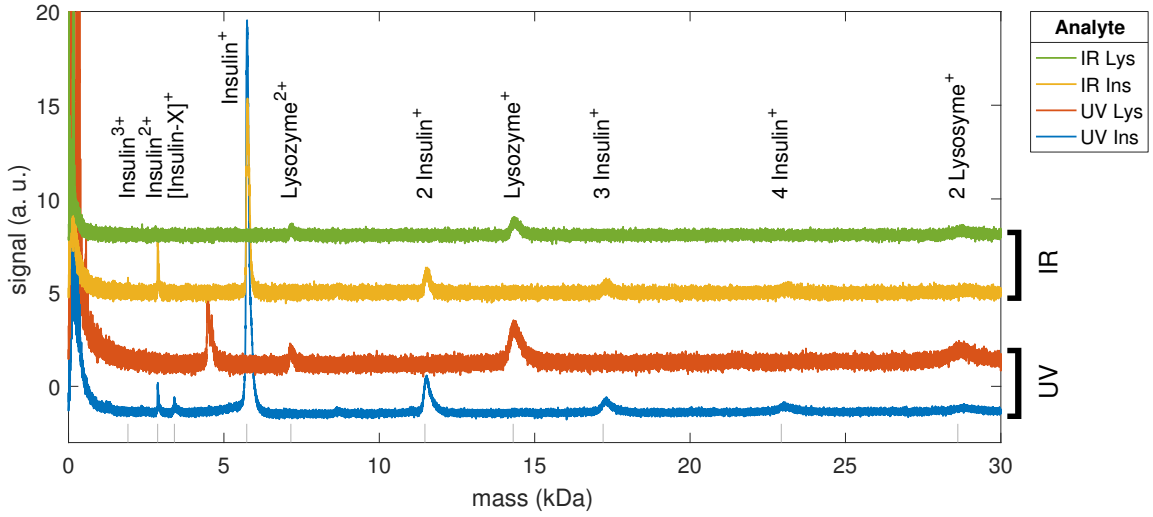

Figure 4.12: Comparison of UV- and IR-MALDI of heavier molecules: 100 µM insulin (blue, yellow curve) or hen egg lysozyme (red, green curve) in 0.1 % TFA with matrix DHB. Average of about 100 spectra (400 spectra for UV-MALDI of insulin).

UV spectrum of insulin was recorded at 2.3 µJ pulse energy, the UV spectrum of lysozyme at 3.0 µJ, and both IR spectra at 36 µJ. For both UV- and IR-MALDI, the lysozyme dimer at $m/z = 28\,615$ and even the insulin pentamer at $m/z = 28\,669$ were discernible. Even though this was a good result for a linear TOF instrument without delayed extraction, it was clear that molecules above 10 kDa would be increasingly difficult to detect.

4.3.2 PIRL Desorption Ionization from Thick Water Ice

While previous studies concerned with IR-LDI from frozen solutions in a TOF instrument would see ions only sporadically and with weak signal intensities [20, 21], it was found here that peptide spectra could be produced reproducibly and with good signal-to-noise. An example spectrum of 100 µM angiotensin I in pure water is shown in fig. 4.13. The signal was averaged over 30 shots at a laser pulse energy of 56 µJ at the sample location. Panel a) shows the low mass region up to 100 Da. This region was dominated by clusters of water, sodium and potassium, three ion peaks which lie very close together. The peaks of smaller clusters were used for mass calibration of the spectrum. The high mass region showed the singly, doubly and triply charged protonated parent ion and the angiotensin dimer. In this case, the doubly charged ion peak was the strongest, although this was only the case for very intense ion signal, whereas otherwise the singly charged ion peak was of comparable magnitude or stronger than the higher charge state. The heavier adduct peaks visible for angiotensin could unfortunately not be identified. A known angiotensin I fragment at $m/z = 272.07$ and the angiotensin II quasi-molecular ion at $m/z = 1046.53$ were also visible. Again, it was not

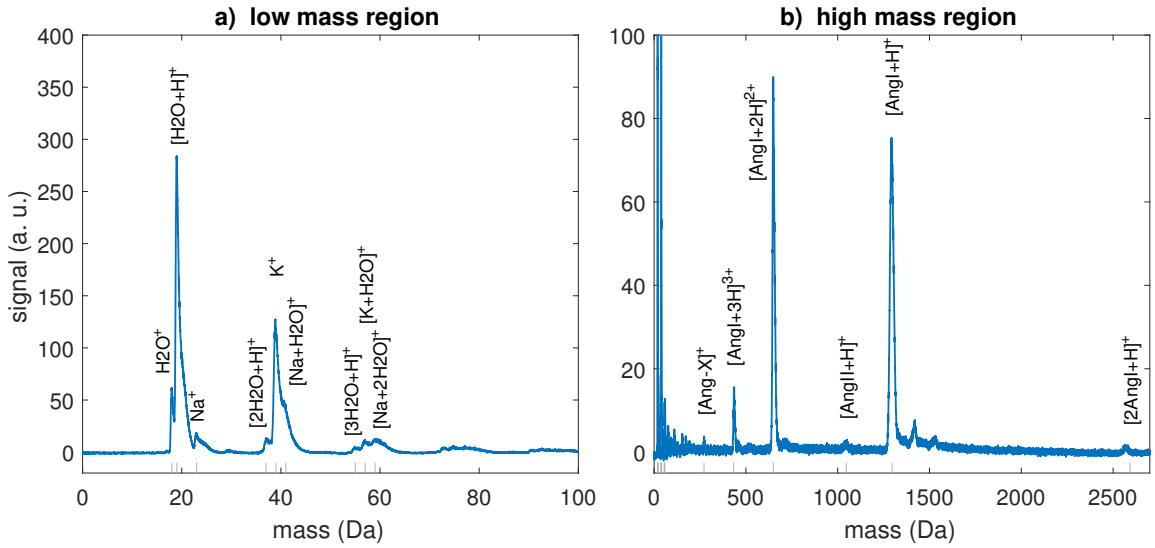

Figure 4.13: DIVE mass spectrum acquired from a frozen droplet of 100 µM angiotensin I in water. Average of 30 laser shots with 56 µJ pulse energy on one sample location. a) The low mass region showed a series of charged clusters of water, sodium, and potassium. b) The high mass region mainly contained the quasi-molecular ion $[\mathrm{AngI} + \mathrm{H}]^+$ including higher charge states and the dimer.

clear whether these were produced during ablation or were already present in the sample solution. Signal could be routinely achieved at analyte concentrations of 100 µM and higher, and was still observed for 10 µM solutions with some effort. In terms of mass range, insulin (5733.55 g/mol) was so far the largest molecule investigated and was successfully detected.

However, not all locations on a frozen droplet yielded ion spectra, similar to what has been reported previously [20]. Figure 4.14 shows the spatial dependence of several prominent ion peaks, again recorded at a laser pulse energy of 56 µJ. Figure 4.13 showed the spectrum for one pixel from this map, but only averaged over the second half of the 60 shots which gave slightly better signal. To create these maps, the maximum ion signal in the region of the proton peak (H^+, (0.66 ± 0.05) µs), the hydronium ion ($\mathrm{H_3O^+}$, (2.97 ± 0.60) µs), the region of water clusters ((5.88 ± 0.30) µs, mainly $[4\,\mathrm{H_2O} + \mathrm{H}]^+$), and the angiotensin I quasi-molecular ion peak ($[\mathrm{AngI} + \mathrm{H}]^+$, (24.3 ± 1.0) µs) were averaged over the first 60 laser shots at each position along the droplet with a step size of 200 µm. Given that peaks shifted from position to position and shot to shot, the maximum signal amplitude within a given arrival time window was considered as the corresponding peak amplitude. This meant that detector saturation or the appearance of additional peaks could potentially add to (or subtract from) the true amplitude. Note the nonlinear colormap in fig. 4.14 which was chosen to emphasize low signal amplitudes. The outline of the droplet is clearly visible on the basis of the $\mathrm{H_3O^+}$ ion peak, which gave very strong and prolonged signal on each droplet

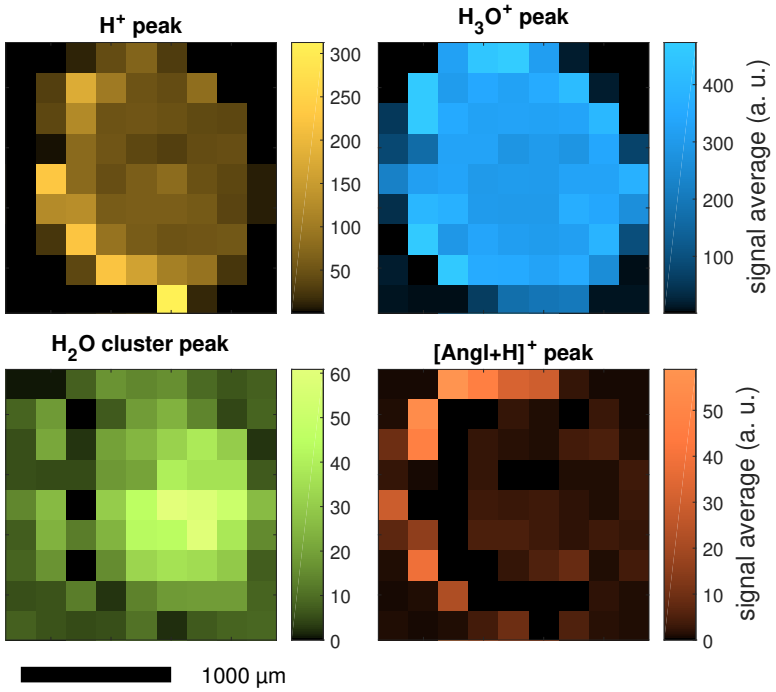

Figure 4.14: Spatial mapping of several ion peaks from a frozen droplet of 100 µM angiotensin I in water. Spectra were acquired at a step size of 200 µm by averaging the first 60 laser shots at each location using a pulse energy of 56 µJ. The analyte peak was primarily visible at the left droplet edge.

position, but yielded no signal or signal for only a couple of shots on the bare substrate. A similar distribution but with slightly lower signal amplitude was found for the proton peak. Both of these peaks would frequently saturate. Indeed, the strong signals in the H^+ map are all indicative of full detector saturation for at least part of the signal acquisition on that spot. This was also reflected in low signal amplitudes for the water cluster and the angiotensin peaks at these positions.

The angiotensin ion was best visible on the left edge of the frozen droplet. This was most likely caused by the difference in laser focusing on different droplet locations: because the laser was incident at a 30° angle from the left side, this droplet face – which was oriented more perpendicular to the laser beam axis – would receive a higher fluence than the right side of the droplet, for which part of the laser beam might have been cut off by the thicker parts already. This is illustrated in fig. 4.15a. In addition, thicker parts of the droplet were farther out of the laser focus, reducing the local fluence even more. The sampling position had to be chosen carefully and on the very rim of the sample. A position 200 µm further towards the droplet center would often already lead to strong detector saturation by the low mass background (mostly the H_3O^+ peak). The suppression of the angiotensin molecular

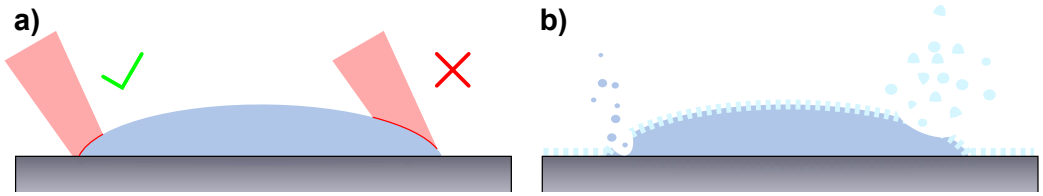

Figure 4.15: Possible explanation for the strong dependence of the ion signal on laser focus position. a) The laser fluence changes depending on the projection of the laser focus onto the droplet surface. b) A larger, less focused laser beam ablates mostly porous condensed ice, whereas more analyte solution is ablated under better focusing conditions. Higher energy densities in the focus on the left rim of the droplet should also lead to better desolvation.

ion peak detection is well visible as a dark semi-circle in fig. 4.14. This detector saturation would not necessarily set in immediately, but would develop after several ten shots and then appear suddenly, possibly once the laser fluence at the slowly receding material surface crossed the threshold for efficient ablation. The reason for this sudden increase in low-mass background remained unclear, although it can be hypothesized that the formation of a deeper crater might play a role.

In general, it took a number of shots for stable signal to appear. Figure 4.16 shows this for the central location on the droplet where the water cluster signal was strongest. The data for this figure was smoothed with a 5 ns moving average to reduce noise in these single shot spectra. The mean ion arrival times mentioned above for the map creation are marked with gray dashed lines. The first shot on a thick ice layer usually produced a broad, undefined peak, which was verified to consist of mostly initially neutral particles: the signal still occurred even after increasing the extraction electrode voltage to several kilovolt above the sample voltage, which created a decelerating field gradient in the first extraction region but a stronger accelerating gradient in the second region, while leaving the total kinetic energy of the ions constant. This way, only positive ions that were created within the second acceleration region would reach the detector. This phenomenon was most likely caused by a slow desolvation process which led to a delayed ionization of large water droplets or clusters. The signal would then evolve within few shots to show a strong hydronium ion peak, but still contain a large neutral bulge. Only then would defined peaks of water clusters appear, until finally the angiotensin I signal would become visible for shot numbers often > 30, although the exact shot number could vary.

Water clusters could also be observed on the bare substrate. This was attributed to a thin layer of condensed ice or frost which would inevitably form during sample loading, even though the procedure was performed under nitrogen atmosphere. Figure 4.17a shows spectra resulting from a series of consecutive laser shots for two different samples. The

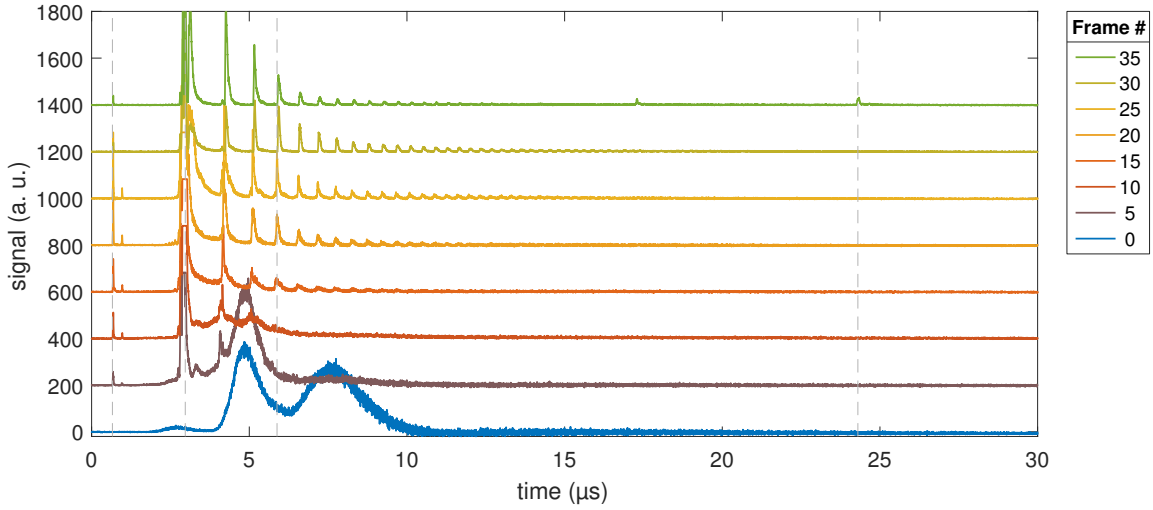

Figure 4.16: Signal evolution over a number of laser shots on the same sample location on the left rim of a frozen droplet containing 100 µM angiotensin I. The peaks mapped in fig. 4.14 are marked with grey dashed lines. While the first shot usually produced one or more broad and featureless peaks, more defined cluster ion peaks appeared after several shots, and after about 30 shots the analyte ion peak became visible.

blue curves represent the first four laser shots on a substrate which was covered in a rather thick condensation layer, as is evidenced by the image in fig. 4.17c, which shows the camera view of several ablation craters right after these acquisitions. The image shows a rather grainy surface of the ice layer, and rugged borders of the ablation craters which exhibit high contrast. The spectra from this sample presented in a) were dominated by the broad, largely undefined ion peak which could also be observed during the first few spectra when ablating on the frozen droplets. In contrast, panel b) shows a number of ablation craters on a much thinner condensation layer on which the spectra shown in orange were recorded. Here, signal could only be acquired for the first laser shot, and very defined water cluster peaks were visible on top of the broad neutral bulge.

This seemed to indicate a detrimental influence of this bulge, which apparently overshadowed other, more resolved ion peaks, or even involved processes leading to a decrease in ionization efficiency for the analyte ions. Ablation of more of the condensation layer would thus negatively impact analyte ion signal. As is illustrated in fig. 4.15b, the different laser focusing conditions on different parts of the droplet possibly led to a change in the ratio of ablated analyte versus condensation layer, where the laser energy was mostly absorbed by the latter when the beam was defocused. To investigate whether sample thickness was the main factor for the differences in the observed ion signal, a different sample preparation technique was tried: spraying the analyte solution onto a cold substrate using a spray pistol produced a seemingly homogeneous layer of fine micro droplets. No angiotensin signal

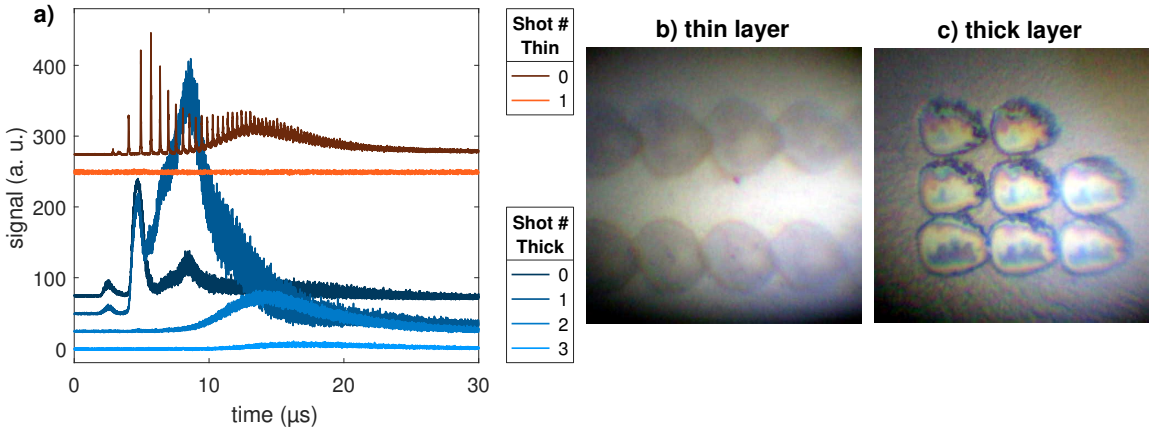

Figure 4.17: Signal evolution over several consecutive shots on the frozen condensation layer on a silicon substrate. a) A thick condensed layer led to broad, ill-defined signal for several laser shots, while the signal from a very thin layer only appeared for one shot and exhibited sharp water cluster peaks. Corresponding camera images of the sample surface during the experiment are shown in b) and c) for the thin and thick condensation layer, respectively.

could be observed from these samples, further pointing towards the importance of the ratio between the dense ice of the frozen droplets versus the porous, low density ice of the condensation layer.

The large sample thickness and the increased ablation depth on the frozen droplets led to another effect: the ion arrival time for a single species would fluctuate considerably, both between shots on one sample location and from position to position along a droplet. Different positions of ion generation along the TOF axis could be expected to be a main source for this arrival time spread. A natural approach to solve this problem would have been to optimize the extraction voltages according to the Wiley-McLaren design, as was done in the beginning of section 4.3.1. However, the rather high electric ion extraction potential used for the MALDI experiments before was not optimal and led to significant detector saturation in the low-mass region when applied during the measurements from frozen droplets. This would impede measurements of the analyte ion peak.

A series of spectra acquired at different extraction voltages is shown in fig. 4.18a. For these measurements, frozen droplets were prepared from 100 µM angiotensin I in 0.001 M (0.008 % v/v) TFA. As can be seen, the analyte ion signal dropped significantly for stronger acceleration fields while the low mass background became stronger. For most spectra shown in this figure, this background was strong enough to be clipped by the digitizer, and would even completely saturate the amplifier for the measurement at 13.2 kV, which led to the flat and negative signal for later arrival times. The signal quality was analyzed for a number of measurements in form of the ratio between the analyte ion peak amplitude and the strength

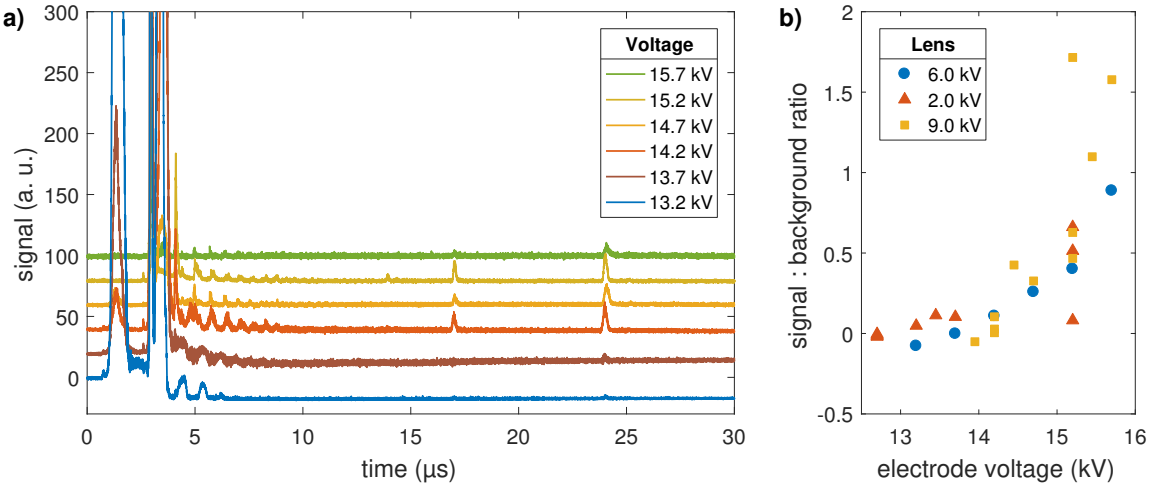

Figure 4.18: Signal dependence on the extraction voltage recorded from a frozen water droplet containing 100 µM angiotensin I and 0.008 % TFA with a pulse energy of 45 µJ. Averages of 10 acquisitions. The total acceleration potential was 16 kV. a) Spectra for different extraction electrode potentials with an Einzel lens voltage of 6 kV. b) Ratio of the analyte ion peak height and the background signal strength as a function of extraction voltage for different lens voltages. The signal quality improved with smaller extraction fields in the first acceleration region.

of the low-mass background. The latter was quantified as the area under the curve between 2.75 to 4 µs, which gave a good indication of the level of detector saturation. Figure 4.18b shows this ratio for three different lens voltages. Independent of the ion lens, better signal-to-background ratios were found for smaller extraction fields (i.e. larger extraction electrode potentials). However, at extraction voltages close to the sample potential, the overall signal amplitude would decrease again, possibly because the ion beam was not sufficiently collimated or ions were not efficiently extracted. An electrode potential of 15.2 kV seemed optimal and was chosen for all presented DIVE measurements. As shown for the UV-MALDI experiments, such low extraction voltages negatively impacted the mass resolution, so that a resolution of only about 40 was routinely achieved in the DIVE experiments. The reason for the detector saturation for stronger acceleration fields remained unclear.

As discussed in chapter 2, the mechanisms leading to analyte ionization are still a field of active research. However, in all of the presented models, an increased availability of charges that can be easily transferred to the analyte should lead to an increase in ion formation. In the lucky survivors model in particular, the analyte molecule's charge state in solution should strongly influence the observed ion yield [11]. For this reason, measurements at different pH values were performed by adding different concentrations of trifluoracetic acid (TFA) or sodium hydroxide (NaOH), ranging from 5 mM to 1 M, to a sample of 100 µM angiotensin I. Angiotensin I, which is represented by the aminoacid sequence

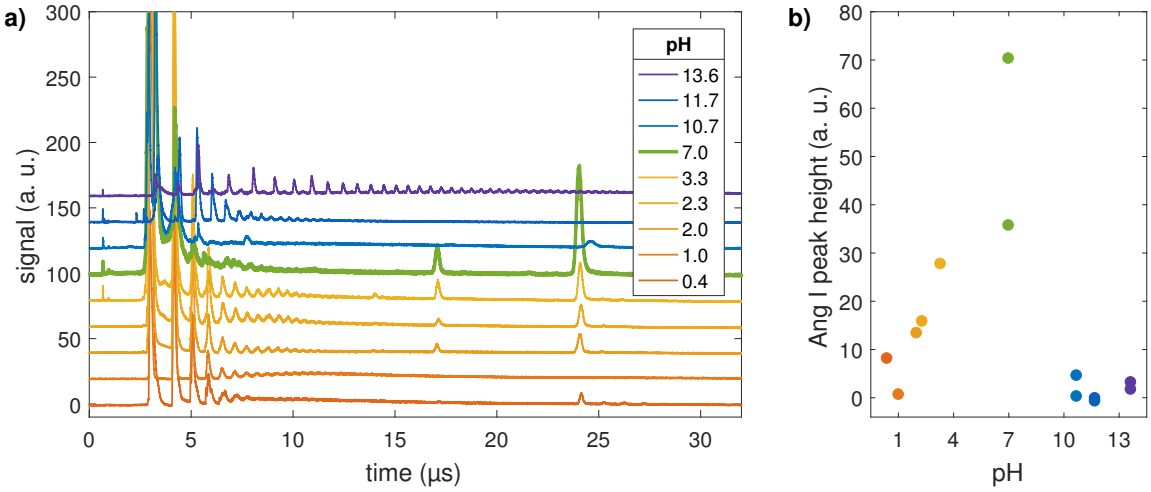

Figure 4.19: DIVE ion signal at different pH conditions recorded from frozen droplets of 100 µM angiotensin I in aqueous solution containing either TFA or NaOH. Averages of 100 spectra at 45 µJ pulse energy. a) The series of spectra shows strong water cluster signals at non-neutral pH. b) The strongest analyte signal was observed at neutral pH, i.e. in pure water.

Asp - Arg - Val - Tyr - Ile - His - Pro - Phe - His - Leu ,

contains 3 basic (arginine, histidine) and one acidic amino acid (aspartic acid). At pH 7.5, its isoelectric point, angiotensin I carries no net electric charge in solution. A pH of about 7 was verified for the angiotensin solution in pure water by an indicator paper. The measurements presented in fig. 4.19 were performed at a laser pulse energy of 45 µJ. The first 100 shots from one location were averaged for each sampling position, and the best average spectrum out of several taken at the same conditions for the respective pH selected for presentation in panel a). The angiotensin I quasi-molecular ion peak signal amplitude for the different measurements is summarized in panel b). Perhaps contrary to the expectation, best signal was achieved at neutral pH, and the charge state distribution did not vary significantly.

Some variation in the data was clearly observed. Especially one of the three measurements at pH 7 showed a much lower signal intensity, most likely because of a suboptimal sampling location on the droplet edge. Still, a clear trend towards less signal for higher acid/base concentrations was verified over a large number of measurements. The ion yield seemed especially suppressed when a base was added, such that signal was not attainable at pH > 11. On the other hand, the quasi-molecular ion could still be observed at the lowest pH of 0.7, but with significantly reduced intensity. Strong and well-defined water clusters seemed to appear preferentially for the higher acid/base concentrations. Note that spectra are shown

[4]Based on data from the Spectral Database for Organic Compounds (SDBS) https://sdbs.db.aist.go.jp
[4]Taken from Wikimedia Commons https://commons.wikimedia.org/wiki/File:Cobalamin.png

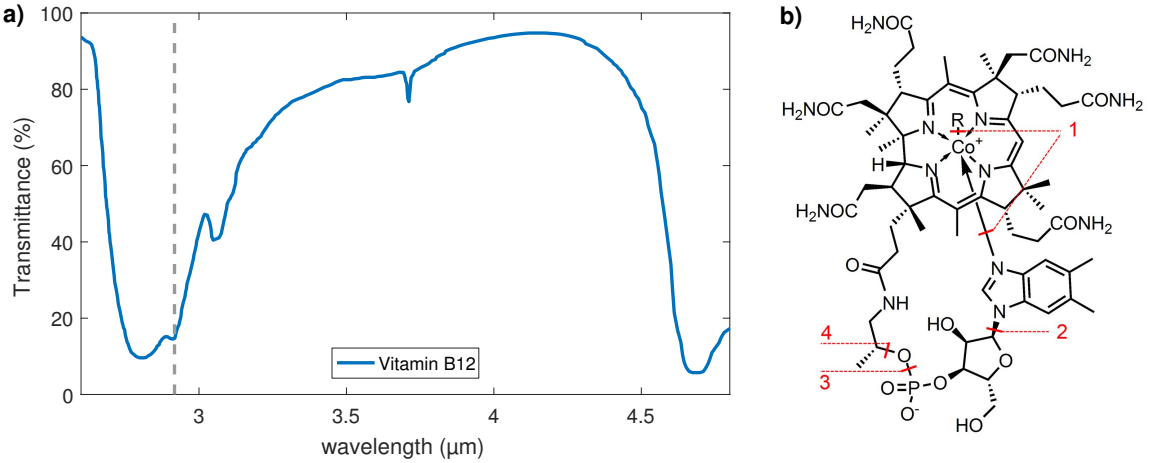

Figure 4.20: a) Absorption spectrum of vitamin B12 (cyanocobalamin).[3] b) Structure of vitamin B12[4], where R = CN for cyanocobalamin, with the identities of the observed fragment ions indicated in red according to ref. [239]. (1) [M − CN] (2) $[M - CN - base]^+$ (3) $[M - CN - base - sugar - PO_3]^+$ (4) $[M - CN - base - sugar - PO_4]^+$

as a function of arrival time and can thus be slightly shifted due to the position on the sample and the exact electric potentials during the measurements. That at least some signal was observed for such a wide range of pH values was a good sign for the applicability of MSI under DIVE conditions to a broad variety of biological samples.

Finally, it was necessary to show that the ionization was not a substrate effect, but that ions were created through the DIVE process. In particular, substrate heating could lead to ablation without the need for a water matrix, as has been shown in a study of matrix-free IR laser desorption ionization from polished silicon surfaces [48]. This study reported significant fragmentation of vitamin B12 (1355.36 g/mol) under conditions of both IR-MALDI with succinic acid and matrix-free IR-LDI from silicon and steel targets. More specifically, they detected almost exclusively the fragment ions $[M - CN - base - sugar - PO_4 + H]^+$ ($m/z = 972$) and $[M - Co - CN - base - sugar + H]^+$ ($m/z = 913$). The reason for this fragmentation was shown to be caused by the strong optical absorption of B12 at 2.94 µm wavelength, and did not occur for UV-MALDI. Similarly severe fragmentation has been observed for matrix-free UV-LDI or when a too small amount of matrix was added for UV-MALDI [239]. Generally, vitamin B12 is known to be a very fragile molecule, and the loss of the reactive center, which for cyanocobalamin is the cyano-group (CN), is usually observed in UV-MALDI, often even as the dominant ion peak. An IR absorption spectrum of B12 with the wavelength of interest marked by a gray dashed line is shown in fig. 4.21a, and the molecule's structure with the most likely fragmentation sites annotated in fig. 4.21b.

The DIVE-MS measurements performed in the current work showed a very different

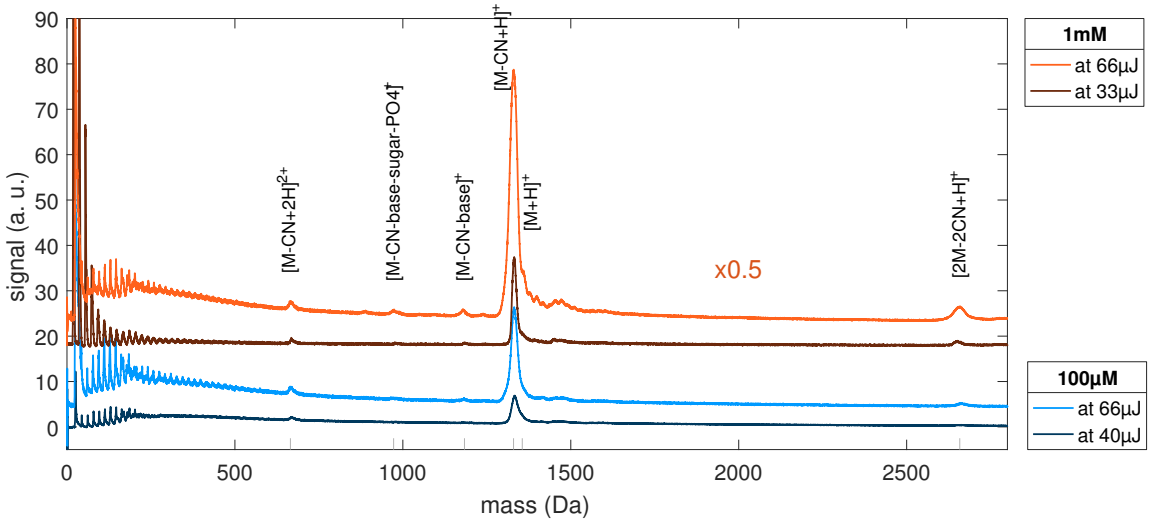

Figure 4.21: Spectra recorded from frozen droplets containing different concentrations of vitamin B12 exhibit considerably less fragmentation than those known for matrix-free LDI. Low-mass ion suppression was enabled for all measurements but the one at 33 µJ pulse energy. Averages of several hundred spectra.

picture to what was shown for matrix-free LDI. Figure 4.21 demonstrates that an intense peak close to the expected molecular ion arrival time was observed at concentrations of 100 µM to 1 mM and that no significant fragmentation occurred even at a laser fluence of 66 µJ. Samples were prepared in 0.1 % TFA, and the low-mass background was suppressed by pulsing a pair of deflector plates for all but the lowest shown pulse energy. In agreement with ref. [239], the dominant peak was most likely the $[M - CN + H]^+$ fragment, although a clear identification was difficult because of the poor mass resolution and accuracy of the instrument. Under this assumption, the high mass tail was composed of the salt adduct ion peaks for this fragment as well as for the intact B12 molecule. An adduct peak at about 150 Da could unfortunately not be identified. The fragments $[M - CN - base - sugar - PO_4]^+$, $[M - CN - base - sugar - PO_3]^+$, and $[M - CN - base]^+$ could also be observed, although with very faint amplitudes.

With a pulse energy of 66 µJ, the employed fluence can be estimated to have been a factor of 2 lower than what was used in ref. [48]. This shows that the ablation and ionization threshold fluence is lower in DIVE compared to matrix-free LDI. In addition, the absence of significant fragmentation was a clear sign of the beneficial effects of evaporative cooling caused by the water molecules, similar to the processes occurring in MALDI.

4.4 Conclusions

It was shown that ions of biological molecules could be efficiently produced from frozen aqueous solution under vacuum conditions by means of desorption by impulsive vibrational excitation. Sampling from the very edge of frozen droplets on a doped silicon substrate, the molecular ion peak for various single-analyte solutions was detected reproducibly and with a signal-to-noise $\gg 10$. Several molecule classes were analyzed, including the peptide angiotensin I, the vitamin B12, and the protein insulin. The lowest concentration from which signal could still be observed was 10 µM, with 5 pmol of analyte loaded in one frozen droplet. This is far above typical limits of detection in UV-MALDI, which reach the low femtomol to attomol region. However, only a small part of the droplet had to be sampled, and with the ability to record often more than 100 spectra from a single location, the required volume can potentially be largely reduced, so comparable limits of detection should be within reach.

The absence of significant fragmentation even for a fragile molecule such as vitamin B12 demonstrated that DIVE is far softer than matrix-free LDI. The spectra acquired here were very comparable with results known for UV-MALDI [239], which is surprising given the molecule's significant optical absorption at the PIRL wavelength. An efficient energy dissipation channel that protects the ion integrity during ablation could be given by fast evaporative cooling by desolvating water molecules under DIVE conditions.

Detector saturation in the low mass region was identified as a problem for increasing the laser power and extraction voltage. While on steel and other opaque substrates, large amounts of low mass noise appeared because of plasma generation in the laser focus, this effect was not observed on silicon unless surface impurities were hit by the laser. Instead, water and salt ion clusters were the main contributors to the noise observed here. Deflecting undesired signal contributions by a high voltage pulse significantly reduced the low-mass background.

Contrary to UV-MALDI in positive ion mode, which usually yields best results under strongly acidic conditions with pH < 3 [240], best signal for DIVE was obtained at neutral pH. The influence of pH was apparently not further investigated in previous studies, where pure water [20] or water with 0.1 % TFA [21] were used as sample solvents. The analysis performed here shows that a wider range is potentially accessible, including conditions of physiological pH for most biomolecules. One reason why analyte signal might have previously been elusive was that only a small part on the rim of a frozen droplet produced strong ion peaks, whereas thicker parts tended to only yield a strong, unspecific low-mass background, which usually led to detector saturation. Another reason might have been that signal would only appear after several ten shots onto the same sample location. This shot

dependency could very well be caused by the condensation layer that grew during sample loading even under a dry nitrogen atmosphere: spectra on a blank substrate covered with such a layer looked very similar to the first shots on a droplet. Analyte ion formation was likely precluded by the desorption of water clusters from this layer, which would explain why no signal could be observed from the thin samples produced by spraying a cold substrate with a fine mist of analyte solution. The sample preparation procedure thus needs to be improved to prevent such ice layer condensation.

Generally, a thin-film preparation technique would be preferable to the droplet preparation, and would more closely resemble the morphology of thin cryo-sections. It would also enable the use of the backside ablation geometry. Vitrification by quickly immersing a wetted substrate in cold ethane, similar to what is commonly used in electron microscopy, could be a technique suitable for further fundamental studies of the ionization mechanism. Such thin films would also help to reduce the initial position spread of the ions and thus lead to a better mass resolution. This would allow for a better identification of the observed ion species, in particular any fragment ions, and also improve the visibility of heavier ion peaks. An investigation of the mass range of PIRL ionization was currently limited by peak broadening and the drop-off of the detection efficiency for higher masses. Increasing the acceleration potential to at least 20 kV and incorporating a reflectron into the instrument would alleviate these issues.

Chapter 5

Summary and Outlook

Nobel laureate John Fenn's metaphor of "*making elephants fly*" [241], which was as much an adequate description of how ions of sheer unlimited mass are created in the electrospray process as it was an expression of the initial disbelief that such a simple method could be this successful, is as relevant today as it has ever been. High-throughput screening of tissues and bodily fluids in the clinical environment requires a simple yet effective method of ion generation. Both biomarker identification and proteomics in general would benefit profoundly from top-down mass spectrometry, for which the ability to capture and identify these elephants intact is essential. Finally, mass spectrometry imaging would hugely benefit from a reduction of the required sample preparation steps and the elimination of the requirement of an artificial matrix. Only, how does one get the elephants into the air when they are not already in solution? PIRL-DIVE sets out to solve this problem by offering the ability to analyze specimens by making use of their endogenous water "matrix", incurring only minimal amounts of internal energy to the created ions, and providing the flexibility and ease-of-use that only a laser-based method can.

The present work investigated the PIRL ablation process under two very different conditions: digital interference microscopy was used to look at the plume dynamics under atmospheric pressure, where the expansion in ambient air led to the formation of a hot and dense shock front. Droplets were shown to make up a significant fraction of the ejected material when ablating from a liquid surface, while vapor phase material would only prominently appear at higher fluences well above the ablation threshold. Especially with a recent study by Y. Lu in mind, which showed an unusually large amount of multiply charged ions when coupling the PIRL plume from a droplet of analyte solution to an ion trap mass spectrometer [111], the role of droplet formation and desolvation in direct laser ablation and ionization has yet to be fully understood. The evolution of a dense material cloud moving at the tip of the plume was presented in chapter 3, and an experiment with which this cloud could potentially be analyzed in the absence of larger droplets by ablating only a very small

volume of liquid was suggested. It was demonstrated that in this geometry, the amount of droplet desolvation could be directly controlled by changing the laser fluence.

In the other type of experiment, PIRL-DIVE under vacuum conditions, the results indicated that proper desolvation of the ablated material might also play a significant role for ion generation in this scenario. Both the thickness of a frozen analyte droplet at the sampling location and the formation of an over-layer of condensed ice had a strong influence on the detected ion yield. Delayed desolvation of large water clusters, which predominantly formed under improper irradiation conditions such as insufficient laser fluence or shielding by the porous over-layer of ice, could be one explanation for the observed bulge of unspecific ion signal. In any case, contrary to previous reports, strong and stable ion signal was detectable from these droplets for hundreds of shots at analyte concentrations between 10 µM to 1 mM. The best signal quality was achieved on droplets with neutral pH, and for sampling locations at the rim of the droplet facing the laser beam.

A combination of the time-resolved imaging technique with the ablation under vacuum would be desirable to investigate the effects of the condensation layer and the droplet thickness further. Of course, the spatial constraints of a vacuum chamber add another level of complexity to the interferometry setup. Still, a characterization of the ratio of vapor phase to liquid or solid phase material during PIRL ablation would give insights into the ionization processes, and could also serve as a precursor to the setup of laser post-ionization, as has been shown previously for the MALDI-2 ion source developed in the Dreisewerd group [131, 159].

Moreover, the ablation of small particles for sample delivery in serial x-ray crystallography was demonstrated here to be feasible, but should be extended to include actual protein crystals. For this, the incorporation of an improved chip design and loading protocol such as that presented in ref. [1] would be of help.

Finally, ionization by DIVE under vacuum conditions did not yet reach the performance of UV-MALDI in terms of the limit of detection or the mass resolution. However, even in the current state, direct laser ablation of frozen cryo-sections of tissues or cells should yield enough signal for basic mass spectrometry imaging, similar to what has been shown for subambient [94] and ambient [136, 137] conditions. Improving the sample preparation protocol to avoid condensation and to produce perfectly flat and thin specimen layers is expected to increase the ion yield. Higher energy densities throughout the layer should lead to better desolvation and faster evaporative cooling of the ejected material. At the same time, less material is ejected per area from thinner layers, so that a less dense ablation plume is formed. Reducing the amount of in-plume collisions between ions and neutrals could decrease the energy loss the charged particles experience during their acceleration

through the ablation cloud, and moderate the neutralization of pre-charged molecules. In addition, prompt desolvation of pre-charged ions and their mainly forward-peaked ejection when vaporized by a picosecond laser pulse could help to retain spatial correlations between molecules ablated from a larger spot. In combination, DIVE from thin sample sections presents itself as a promising approach to stigmatic ion imaging below the diffraction limit.

Bibliography

[1] E. C. Schulz, J. Kaub, F. Busse, P. Mehrabi, H. M. Müller-Werkmeister, E. F. Pai, W. D. Robertson, and R. J. D. Miller. Protein crystals IR laser ablated from aqueous solution at high speed retain their diffractive properties: applications in high-speed serial crystallography. *J. Appl. Crystallogr.*, 50(6):1773–1781, December 2017.

[2] F. Busse, S. Kruber, W. D. Robertson, and R. J. D. Miller. Digital interference microscopy and density reconstruction of picosecond infrared laser desorption at the water-air interface. *J. Appl. Phys.*, 124(9):094701, September 2018.

[3] E. R. Amstalden van Hove, D. F. Smith, and R. M. A. Heeren. A concise review of mass spectrometry imaging. *J. Chromatogr. A*, 1217(25):3946–3954, June 2010.

[4] B. Spengler. Mass Spectrometry Imaging of Biomolecular Information. *Anal. Chem.*, 87(1):64–82, January 2015.

[5] K. K. Murray, C. A. Seneviratne, and S. Ghorai. High resolution laser mass spectrometry bioimaging. *Methods*, 104:118–126, July 2016.

[6] M. T. Bokhart and D. C. Muddiman. Infrared matrix-assisted laser desorption electrospray ionization mass spectrometry imaging analysis of biospecimens. *Analyst*, 141(18):5236–5245, August 2016.

[7] J. Griffiths. A Brief History of Mass Spectrometry. *Anal. Chem.*, 80(15):5678–5683, August 2008.

[8] C. N. McEwen and B. S. Larsen. Fifty years of desorption ionization of nonvolatile compounds. *Int. J. Mass Spectrom.*, 377:515–531, February 2015.

[9] B. K. Kaletaş, I. M. v. d. Wiel, J. Stauber, L. J. Dekker, C. Güzel, J. M. Kros, T. M. Luider, and R. M. A. Heeren. Sample preparation issues for tissue imaging by imaging MS. *Proteomics*, 9(10):2622–2633, 2009.

[10] S. R. Ellis, A. L. Bruinen, and R. M. A. Heeren. A critical evaluation of the current state-of-the-art in quantitative imaging mass spectrometry. *Anal. Bioanal. Chem.*, 406(5):1275–1289, February 2014.

[11] T. W. Jaskolla and M. Karas. Compelling Evidence for Lucky Survivor and Gas Phase Protonation: The Unified MALDI Analyte Protonation Mechanism. *J. Am. Soc. Mass Spectrom.*, 22(6):976–988, June 2011.

[12] R. Knochenmuss. The Coupled Chemical and Physical Dynamics Model of MALDI. *Annual Rev. Anal. Chem.*, 9(1):365–385, 2016.

[13] K. Dreisewerd. The Desorption Process in MALDI. *Chem. Rev.*, 103(2):395–426, February 2003.

[14] M. Karas and R. Krüger. Ion Formation in MALDI: The Cluster Ionization Mechanism. *Chem. Rev.*, 103(2):427–440, February 2003.

[15] R. Knochenmuss. Ion formation mechanisms in UV-MALDI. *Analyst*, 131(9):966–986, 2006.

[16] K. Dreisewerd, S. Berkenkamp, A. Leisner, A. Rohlfing, and C. Menzel. Fundamentals of matrix-assisted laser desorption/ionization mass spectrometry with pulsed infrared lasers. *Int. J. Mass Spectrom.*, 226(1):189–209, March 2003.

[17] K. Franjic and R. J. D. Miller. Vibrationally excited ultrafast thermodynamic phase transitions at the water/air interface. *Phys. Chem. Chem. Phys.*, 12(20):5225–5239, May 2010.

[18] R. M. Alberici, R. C. Simas, G. B. Sanvido, W. Romão, P. M. Lalli, M. Benassi, I. B. S. Cunha, and M. N. Eberlin. Ambient mass spectrometry: bringing MS into the “real world”. *Anal. Bioanal. Chem.*, 398(1):265–294, September 2010.

[19] A. D. Catherman, O. S. Skinner, and N. L. Kelleher. Top Down Proteomics: Facts and Perspectives. *Biochem. Biophys. Res. Commun.*, 445(4):683–693, March 2014.

[20] S. Berkenkamp, M. Karas, and F. Hillenkamp. Ice as a matrix for IR-matrix-assisted laser desorption/ionization: mass spectra from a protein single crystal. *Proc. Natl. Acad. Sci. U.S.A.*, 93(14):7003–7007, July 1996.

[21] M. L. Baltz-Knorr, K. E. Schriver, and R. F. Haglund. Infrared laser ablation and ionization of water clusters and biomolecules from ice. *Appl. Surf. Sci.*, 197-198:11–16, September 2002.

[22] S. Berkenkamp, C. Menzel, M. Karas, and F. Hillenkamp. Performance of Infrared Matrix-assisted Laser Desorption/Ionization Mass Spectrometry with Lasers Emitting in the 3 um Wavelength Range. *Rapid Commun. Mass Spectrom.*, 11(13):1399–1406, August 1997.

[23] A. J. Dempster. A new Method of Positive Ray Analysis. *Phys. Rev.*, 11(4):316–325, April 1918.

[24] M. S. B. Munson and F. H. Field. Chemical Ionization Mass Spectrometry. I. General Introduction. *J. Am. Chem. Soc.*, 88(12):2621–2630, June 1966.

[25] D. C. Muddiman. Ionization Methods. The Basics of Mass Spectrometry, Video Tutorial, www.asms.org/about-mass-spectrometry.

[26] H. D. Beckey. Field desorption mass spectrometry: A technique for the study of thermally unstable substances of low volatility. *Int. J. Mass Spectrom. Ion Phys.*, 2(6):500–502, June 1969.

[27] L. Prokai. *Field Desorption Mass Spectrometry.* CRC Press, December 1989.

[28] F. J. Vastola, R. O. Mumma, and A. J. Pirone. Analysis of organic salts by laser ionization. *J. Mass Spectrom.*, 3(1):101–104, 1970.

[29] R. J. Cotter. Laser mass spectrometry: an overview of techniques, instruments and applications. *Anal. Chim. Acta*, 195:45–59, January 1987.

[30] J. Wei, J. M. Buriak, and G. Siuzdak. Desorption–ionization mass spectrometry on porous silicon. *Nature*, 399(6733):243–246, May 1999.

[31] W. G. Lewis, Z. Shen, M. G. Finn, and G. Siuzdak. Desorption/ionization on silicon (DIOS) mass spectrometry: background and applications. *Int. J. Mass Spectrom.*, 226(1):107–116, March 2003.

[32] M. Barber, R. S. Bordoli, R. D. Sedgwick, and A. N. Tyler. Fast atom bombardment of solids (F.A.B.): a new ion source for mass spectrometry. *J. Chem. Soc., Chem. Commun.*, 0(7):325–327, January 1981.

[33] M. Barber, R. S. Bordoli, G. J. Elliott, R. D. Sedgwick, and A. N. Tyler. Fast Atom Bombardment Mass Spectrometry. *Anal. Chem.*, 54(4):645A–657A, April 1982.

[34] C. K. Meng, M. Mann, and J. B. Fenn. Of protons or proteins. *Z. Phys. D*, 10(2):361–368, June 1988.

[35] M. Wilm. Principles of electrospray ionization. *Mol. Cell. Proteomics*, page mcp.R111.009407, January 2011.

[36] K. Tanaka, H. Waki, Y. Ido, S. Akita, Y. Yoshida, T. Yoshida, and T. Matsuo. Protein and polymer analyses up to m/z 100 000 by laser ionization time-of-flight mass spectrometry. *Rapid Commun. Mass Spectrom.*, 2(8):151–153, 1988.

[37] M. Karas, D. Bachmann, and F. Hillenkamp. Influence of the wavelength in high-irradiance ultraviolet laser desorption mass spectrometry of organic molecules. *Anal. Chem.*, 57(14):2935–2939, December 1985.

[38] M. Karas, D. Bachmann, U. Bahr, and F. Hillenkamp. Matrix-assisted ultraviolet laser desorption of non-volatile compounds. *Int. J. Mass Spectrom. Ion Process.*, 78:53–68, September 1987.

[39] M. Karas and F. Hillenkamp. Laser desorption ionization of proteins with molecular masses exceeding 10,000 daltons. *Anal. Chem.*, 60(20):2299–2301, October 1988.

[40] M. Karas, U. Bahr, A. Ingendoh, E. Nordhoff, B. Stahl, K. Strupat, and F. Hillenkamp. Principles and applications of matrix-assisted UV-laser desorption/ionization mass spectrometry. *Anal. Chim. Acta*, 241(2):175–185, January 1990.

[41] F. Hillenkamp. Laser Induced Ion Formation from Organic Solids (Review). In A. Benninghoven, editor, *Ion Formation from Organic Solids*, volume 25 of *Springer Series in Chemical Physics*, pages 190–205, Berlin, Heidelberg, 1983. Springer.

[42] D. A. King. Thermal desorption from metal surfaces: A review. *Surf. Sci.*, 47(1):384–402, January 1975.

[43] B. Lindner and U. Seydel. Laser desorption mass spectrometry of nonvolatiles under shock wave conditions. *Anal. Chem.*, 57(4):895–899, April 1985.

[44] D. S. Peterson. Matrix-free methods for laser desorption/ionization mass spectrometry. *Mass Spectrom. Rev.*, 26(1):19–34, 2007.

[45] M. A. Posthumus, P. G. Kistemaker, H. L. C. Meuzelaar, and M. C. Ten Noever de Brauw. Laser desorption-mass spectrometry of polar nonvolatile bio-organic molecules. *Anal. Chem.*, 50(7):985–991, June 1978.

[46] S. H. Bhattacharya, T. J. Raiford, and K. K. Murray. Infrared Laser Desorption/Ionization on Silicon. *Anal. Chem.*, 74(9):2228–2231, May 2002.

[47] K. K. Murray, S. H. Bhattacharya, M. W. Little, and T. J. Raiford. Infrared Laser Desorption On Transparent Targets. *Proc. Am. Soc. Mass Spectrom.*, 50(WP316):2, 2002.

[48] D. J. Rousell, S. M. Dutta, M. W. Little, and K. K. Murray. Matrix-free infrared soft laser desorption/ionization. *J. Mass Spectrom.*, 39(10):1182–1189, 2004.

[49] Y. Chen, H. Chen, A. Aleksandrov, and T. M. Orlando. Roles of Water, Acidity, and Surface Morphology in Surface-Assisted Laser Desorption/Ionization of Amino Acids. *J. Phys. Chem. C*, 112(17):6953–6960, May 2008.

[50] M. W. Little, J. Laboy, and K. K. Murray. Wavelength Dependence of Soft Infrared Laser Desorption and Ionization. *J. Phys. Chem. C*, 111(3):1412–1416, January 2007.

[51] R. Cramer, editor. *Advances in MALDI and Laser-Induced Soft Ionization Mass Spectrometry*. Springer International Publishing, Cham, 2016.

[52] L. V. Zhigilei, E. Leveugle, B. J. Garrison, Y. G. Yingling, and M. I. Zeifman. Computer simulations of laser ablation of molecular substrates. *Chem. Rev.*, 103(2):321–348, 2003.

[53] R. Knochenmuss and R. Zenobi. MALDI Ionization: The Role of In-Plume Processes. *Chem. Rev.*, 103(2):441–452, February 2003.

[54] K. Dreisewerd. Recent methodological advances in MALDI mass spectrometry. *Anal. Bioanal. Chem.*, 406(9-10):2261–2278, April 2014.

[55] R. Knochenmuss. Energetics and Kinetics of Thermal Ionization Models of MALDI. *J. Am. Soc. Mass Spectrom.*, 25(9):1521–1527, September 2014.

[56] R. Knochenmuss. A quantitative model of ultraviolet matrix-assisted laser desorption/ionization. *J. Mass Spectrom.*, 37(8):867–877, August 2002.

[57] R. Knochenmuss. A Quantitative Model of Ultraviolet Matrix-Assisted Laser Desorption/Ionization Including Analyte Ion Generation. *Anal. Chem.*, 75(10):2199–2207, May 2003.

[58] R. Knochenmuss. Photoionization Pathways and Free Electrons in UV-MALDI. *Anal. Chem.*, 76(11):3179–3184, June 2004.

[59] R. Knochenmuss and L. V. Zhigilei. Molecular Dynamics Model of Ultraviolet Matrix-Assisted Laser Desorption/Ionization Including Ionization Processes. *J. Phys. Chem. B*, 109(48):22947–22957, December 2005.

[60] R. Knochenmuss. A bipolar rate equation model of MALDI primary and secondary ionization processes, with application to positive/negative analyte ion ratios and suppression effects. *Int. J. Mass Spectrom.*, 285(3):105–113, August 2009.

[61] R. Knochenmuss and L. V. Zhigilei. Molecular dynamics simulations of MALDI: laser fluence and pulse width dependence of plume characteristics and consequences for matrix and analyte ionization. *J. Mass Spectrom.*, 45(4):333–346, April 2010.

[62] R. Knochenmuss and L. V. Zhigilei. What determines MALDI ion yields? A molecular dynamics study of ion loss mechanisms. *Anal. Bioanal. Chem.*, 402(8):2511–2519, March 2012.

[63] R. Knochenmuss. MALDI and Related Methods: A Solved Problem or Still a Mystery? *Mass Spectrom.*, 2(Special Issue):S006, April 2013.

[64] R. Knochenmuss. MALDI mechanisms: wavelength and matrix dependence of the coupled photophysical and chemical dynamics model. *Analyst*, 139(1):147–156, 2014.

[65] R. Knochenmuss. Ion Yields in the Coupled Chemical and Physical Dynamics Model of Matrix-Assisted Laser Desorption/Ionization. *J. Am. Soc. Mass Spectrom.*, 26(10):1645–1648, October 2015.

[66] Q. Lin and R. Knochenmuss. Two-photon ionization thresholds of matrix-assisted laser desorption/ionization matrix clusters. *Rapid Commun. Mass Spectrom.*, 15(16):1422–1426, August 2001.

[67] M. Karas, M. Glückmann, and J. Schäfer. Ionization in matrix-assisted laser desorption/ionization: singly charged molecular ions are the lucky survivors. *J. Mass Spectrom.*, 35(1):1–12, January 2000.

[68] I. Fournier, A. Brunot, J. C. Tabet, and G. Bolbach. Delayed extraction experiments using a repulsive potential before ion extraction: evidence of clusters as ion precursors in UV-MALDI. Part I: dynamical effects with the matrix 2,5-dihydroxybenzoic acid. *Int. J. Mass Spectrom.*, 213(2):203–215, February 2002.

[69] S. Alves, F. Fournier, C. Afonso, F. Wind, and J.-C. Tabet. Gas-Phase Ionization/Desolvation Processes and Their Effect on Protein Charge State Distribution under Matrix-Assisted Laser Desorption/Ionization Conditions. *Eur. J. Mass Spectrom.*, 12(6):369–383, December 2006.

[70] G. R. Kinsel, M. E. Gimon-Kinsel, K. J. Gillig, and D. H. Russell. Investigation of the dynamics of matrix-assisted laser desorption/ionization ion formation using an electrostatic analyzer/time-of-flight mass spectrometer. *J. Mass Spectrom.*, 34(6):684–690, 1999.

[71] I. Fournier, A. Brunot, J. C. Tabet, and G. Bolbach. Delayed extraction experiments using a repulsing potential before ion extraction: evidence of non-covalent clusters as ion precursor in UV matrix-assisted laser desorption/ionization. Part II—Dynamic effects with α-cyano-4-hydroxycinnamic acid matrix. *J. Mass Spectrom.*, 40(1):50–59, 2005.

[72] A. N. Krutchinsky and B. T. Chait. On the nature of the chemical noise in MALDI mass spectra. *J. Am. Soc. Mass Spectrom.*, 13(2):129–134, February 2002.

[73] M. Handschuh, S. Nettesheim, and R. Zenobi. Laser-induced molecular desorption and particle ejection from organic films. *Appl. Surf. Sci.*, 137(1):125–135, January 1999.

[74] S. Trimpin, B. Wang, E. D. Inutan, J. Li, C. B. Lietz, A. Harron, V. S. Pagnotti, D. Sardelis, and C. N. McEwen. A Mechanism for Ionization of Nonvolatile Compounds in Mass Spectrometry: Considerations from MALDI and Inlet Ionization. *J. Am. Soc. Mass Spectrom.*, 23(10):1644–1660, October 2012.

[75] Y. J. Bae and M. S. Kim. A Thermal Mechanism of Ion Formation in MALDI. *Annual Rev. Anal. Chem.*, 8(1):41–60, July 2015.

[76] S. Niu, W. Zhang, and B. T. Chait. Direct comparison of infrared and ultraviolet wavelength matrix-assisted laser desorption/ionization mass spectrometry of proteins. *J. Am. Soc. Mass Spectrom.*, 9(1):1–7, January 1998.

[77] X. Chen, J. A. Carroll, and R. C. Beavis. Near-ultraviolet-induced matrix-assisted laser desorption/ionization as a function of wavelength. *J. Am. Soc. Mass Spectrom.*, 9(9):885–891, September 1998.

[78] D. A. Allwood, P. E. Dyer, R. W. Dreyfus, and I. K. Perera. Plasma modelling of matrix assisted UV laser desorption ionisation (MALDI). *Appl. Surf. Sci.*, 109-110:616–620, February 1997.

[79] D. A. Allwood, P. E. Dyer, and R. W. Dreyfus. Ionization Modelling of Matrix Molecules in Ultraviolet Matrix-assisted Laser Desorption/Ionization. *Rapid Commun. Mass Spectrom.*, 11(5):499–503, 1997.

[80] I.-C. Lu, C. Lee, H.-Y. Chen, H.-Y. Lin, S.-W. Hung, Y. A. Dyakov, K.-T. Hsu, C.-Y. Liao, Y.-Y. Lee, C.-M. Tseng, Y.-T. Lee, and C.-K. Ni. Ion Intensity and Thermal Proton Transfer in Ultraviolet Matrix-Assisted Laser Desorption/Ionization. *J. Phys. Chem. B*, 118(15):4132–4139, April 2014.

[81] K. Y. Chu, S. Lee, M.-T. Tsai, I.-C. Lu, Y. A. Dyakov, Y. H. Lai, Y.-T. Lee, and C.-K. Ni. Thermal Proton Transfer Reactions in Ultraviolet Matrix-Assisted Laser Desorption/Ionization. *J. Am. Soc. Mass Spectrom.*, 25(3):310–318, March 2014.

[82] I.-C. Lu, C. Lee, Y.-T. Lee, and C.-K. Ni. Ionization Mechanism of Matrix-Assisted Laser Desorption/Ionization. *Annual Rev. Anal. Chem.*, 8(1):21–39, July 2015.

[83] K. Breuker, R. Knochenmuss, J. Zhang, A. Stortelder, and R. Zenobi. Thermodynamic control of final ion distributions in MALDI: in-plume proton transfer reactions. *Int. J. Mass Spectrom.*, 226(1):211–222, March 2003.

[84] A. Gray-Weale and C.-K. Ni. Comment on: "Energetics and Kinetics of Thermal Ionization Models of MALDI" by Richard Knochenmuss. J. Am. Soc. Mass Spectrom. 25, 1521–1527 (2014). *J. Am. Soc. Mass Spectrom.*, 26(12):2162–2166, December 2015.

[85] R. Knochenmuss. Reply to the Comment on: "Energetics and Kinetics of Thermal Ionization Models of MALDI" by Richard Knochenmuss. J. Am. Soc. Mass Spectrom. 25, 1521–1527 (2014). *J. Am. Soc. Mass Spectrom.*, 26(12):2167–2168, December 2015.

[86] A. Gray-Weale and C.-K. Ni. Comment to the Reply on: "Energetics and Kinetics of Thermal Ionization Models of MALDI" by Richard Knochenmuss. J. Am. Soc. Mass Spectrom. 25, 1521–1527 (2014). *J. Am. Soc. Mass Spectrom.*, 26(12):2169–2170, December 2015.

[87] W. Zhang, S. Niu, and B. T. Chait. Exploring infrared wavelength matrix-assisted laser desorption/ionization of proteins with delayed-extraction time-of-flight mass spectrometry. *J. Am. Soc. Mass Spectrom.*, 9(9):879–884, September 1998.

[88] R. Cramer and A. L. Burlingame. IR-MALDI — Softer Ionization in MALDI-MS for Studies of Labile Macromolecules. In A. L. Burlingame, S. A. Carr, and M. A. Baldwin, editors, *Mass Spectrometry in Biology and Medicine*, pages 289–307. Humana Press, Totowa, NJ, 2000.

[89] S. Berkenkamp. Infrared MALDI Mass Spectrometry of Large Nucleic Acids. *Science*, 281(5374):260–262, July 1998.

[90] A. Overberg, M. Karas, U. Bahr, R. Kaufmann, and F. Hillenkamp. Matrix-assisted infrared-laser (2.94 μm) desorption/ionization mass spectrometry of large biomolecules. *Rapid Commun. Mass Spectrom.*, 4(8):293–296, August 1990.

[91] P. Kraft, S. Alimpiev, E. Dratz, and J. Sunner. Infrared, surface-assisted laser desorption ionization mass spectrometry on frozen aqueous solutions of proteins and peptides using suspensions of organic solids. *J. Am. Soc. Mass Spectrom.*, 9(9):912–924, September 1998.

[92] C. Menzel, S. Berkenkamp, and F. Hillenkamp. Infrared matrix-assisted laser desorption/ionization mass spectrometry with a transversely excited atmospheric pressure carbon dioxide laser at 10.6 µm wavelength with static and delayed ion extraction. *Rapid Commun. Mass Spectrom.*, 13(1):26–32, 1999.

[93] S. Berkenkamp, C. Menzel, F. Hillenkamp, and K. Dreisewerd. Measurements of mean initial velocities of analyte and matrix ions in infrared matrix-assisted laser desorption ionization mass spectrometry. *J. Am. Soc. Mass Spectrom.*, 13(3):209–220, March 2002.

[94] A. Pirkl, J. Soltwisch, F. Draude, and K. Dreisewerd. Infrared Matrix-Assisted Laser Desorption/Ionization Orthogonal-Time-of-Flight Mass Spectrometry Employing a Cooling Stage and Water Ice As a Matrix. *Anal. Chem.*, 84(13):5669–5676, July 2012.

[95] L. Witt, A. Pirkl, F. Draude, J. Peter-Katalinić, K. Dreisewerd, and M. Mormann. Water Ice is a Soft Matrix for the Structural Characterization of Glycosaminoglycans by Infrared Matrix-Assisted Laser Desorption/Ionization. *Anal. Chem.*, 86(13):6439–6446, July 2014.

[96] C. Menzel, K. Dreisewerd, S. Berkenkamp, and F. Hillenkamp. Mechanisms of energy deposition in infrared matrix-assisted laser desorption/ionization mass spectrometry. *Int. J. Mass Spectrom.*, 207(1):73–96, April 2001.

[97] C. W. Robertson and D. Williams. Lambert Absorption Coefficients of Water in the Infrared*. *J. Opt. Soc. Am.*, 61(10):1316, October 1971.

[98] A. Vogel and V. Venugopalan. Mechanisms of Pulsed Laser Ablation of Biological Tissues. *Chem. Rev.*, 103(2):577–644, February 2003.

[99] M. R. Papantonakis, J. Kim, W. P. Hess, and R. F. Haglund. What do matrix-assisted laser desorption/ionization mass spectra reveal about ionization mechanisms? *J. Mass Spectrom.*, 37(6):639–647, June 2002.

[100] K. Dreisewerd, M. Schürenberg, M. Karas, and F. Hillenkamp. Matrix-assisted laser desorption/ionization with nitrogen lasers of different pulse widths. *Int. J. Mass Spectrom. Ion Process.*, 154(3):171–178, July 1996.

[101] Y. Chen and A. Vertes. Pumping Rate and Surface Morphology Dependence of Ionization Processes in Matrix-Assisted Laser Desorption Ionization. *J. Phys. Chem. A*, 107(46):9754–9761, November 2003.

[102] P. Demirev, A. Westman, C. T. Reimann, P. Håkansson, D. Barofsky, B. U. R. Sundqvist, Y. D. Cheng, W. Seibt, and K. Siegbahn. Matrix-assisted laser desorption with ultra-short laser pulses. *Rapid Commun. Mass Spectrom.*, 6(3):187–191, March 1992.

[103] K. Franjic, M. L. Cowan, D. Kraemer, and R. J. D. Miller. Laser selective cutting of biological tissues by impulsive heat deposition through ultrafast vibrational excitations. *Opt. Express*, 17(25):22937–22959, December 2009.

[104] S. Amini-Nik, D. Kraemer, M. L. Cowan, K. Gunaratne, P. Nadesan, B. A. Alman, and R. J. D. Miller. Ultrafast Mid-IR Laser Scalpel: Protein Signals of the Fundamental Limits to Minimally Invasive Surgery. *PLoS ONE*, 5(9):e13053, September 2010.

[105] P. D. S. J. Linke, L. Ren, A. Frings, J. Steinberg, W. Wöllmer, T. Katz, R. Reimer, N. O. Hansen, N. Jowett, G. Richard, and R. J. D. Miller. Perspektiven der laserassistierten Keratoplastik. *Ophthalmologe*, 111(6):523–530, June 2014.

[106] H. Petersen, F. Tavakoli, S. Kruber, A. Münscher, A. Gliese, N.-O. Hansen, S. Uschold, D. Eggert, W. D. Robertson, T. Gosau, S. Sehner, M. Kwiatkowski, H. Schlüter, U. Schumacher, R. Knecht, and R. D. Miller. Comparative study of wound healing in rat skin following incision with a novel picosecond infrared laser (PIRL) and different surgical modalities. *Lasers Surg. Med.*, 48(4):385–391, April 2016.

[107] L. Ren, W. D. Robertson, R. Reimer, C. Heinze, C. Schneider, D. Eggert, P. Truschow, N.-O. Hansen, P. Kroetz, J. Zou, and R. J. D. Miller. Towards instantaneous cellular level bio diagnosis: laser extraction and imaging of biological entities with conserved integrity and activity. *Nanotechnology*, 26(28):284001, July 2015.

[108] M. Kwiatkowski, M. Wurlitzer, M. Omidi, L. Ren, S. Kruber, R. Nimer, W. D. Robertson, A. Horst, R. J. D. Miller, and H. Schlüter. Ultrafast Extraction of Proteins from Tissues Using Desorption by Impulsive Vibrational Excitation. *Angew. Chem. Int. Ed.*, 54(1):285–288, January 2015.

[109] M. Kwiatkowski, M. Wurlitzer, A. Krutilin, P. Kiani, R. Nimer, M. Omidi, A. Mannaa, T. Bussmann, K. Bartkowiak, S. Kruber, S. Uschold, P. Steffen, J. Lübberstedt, N. Küpker, H. Petersen, R. Knecht, N. O. Hansen, A. Zarrine-Afsar, W. D. Robertson, R. J. D. Miller, and H. Schlüter. Homogenization of tissues via picosecond-infrared laser (PIRL) ablation: Giving a closer view on the in-vivo composition of protein species as compared to mechanical homogenization. *J. Proteom.*, 134:193–202, 2016.

[110] A. Krutilin, S. Maier, R. Schuster, S. Kruber, M. Kwiatkowski, W. D. Robertson, N.-O. Hansen, R. J. D. Miller, and H. Schlüter. Sampling of Tissues with Laser Ablation for Proteomics: Comparison of Picosecond Infrared Laser (PIRL) and Microsecond Infrared Laser (MIRL). *J. Proteome Res.*, January 2019.

[111] Y. Lu, C. L. Pieterse, W. D. Robertson, and R. J. D. Miller. Soft Picosecond Infrared Laser Extraction of Highly Charged Proteins and Peptides from Bulk Liquid Water for Mass Spectrometry. *Anal. Chem.*, 90(7):4422–4428, April 2018.

[112] J. Zou, F. Talbot, A. Tata, L. Ermini, K. Franjic, M. Ventura, J. Zheng, H. Ginsberg, M. Post, D. R. Ifa, D. Jaffray, R. J. D. Miller, and A. Zarrine-Afsar. Ambient Mass Spectrometry Imaging with Picosecond Infrared Laser Ablation Electrospray Ionization (PIR-LAESI). *Anal. Chem.*, 87(24):12071–12079, December 2015.

[113] W. D. Robertson, H. Schlüter, R. D. Miller, and Q. C. Ji. New frontiers in drug development utilizing desorption by impulsive vibrational excitation for sample preparation, tissue imaging and beyond. *Bioanalysis*, October 2018.

[114] J. Zou, C. Wu, W. D. Robertson, L. V. Zhigilei, and R. J. D. Miller. Molecular dynamics investigation of desorption and ion separation following picosecond infrared laser (PIRL) ablation of an ionic aqueous protein solution. *J. Chem. Phys.*, 145(20):204202, November 2016.

[115] A. I. Gusev. Interfacing matrix-assisted laser desorption/ionization mass spectrometry with column and planar separations. *Fresenius J. Anal. Chem.*, 366(6):691–700, March 2000.

[116] V. V. Laiko, S. C. Moyer, and R. J. Cotter. Atmospheric Pressure MALDI/Ion Trap Mass Spectrometry. *Anal. Chem.*, 72(21):5239–5243, November 2000.

[117] M. Nazari and D. C. Muddiman. MALDESI: Fundamentals, Direct Analysis, and MS Imaging. In R. Cramer, editor, *Advances in MALDI and Laser-Induced Soft Ionization Mass Spectrometry*, pages 169–182. Springer International Publishing, Cham, 2016.

[118] V. V. Laiko, N. I. Taranenko, V. D. Berkout, M. A. Yakshin, C. R. Prasad, H. S. Lee, and V. M. Doroshenko. Desorption/ionization of biomolecules from aqueous solutions at atmospheric pressure using an infrared laser at 3 um. *J. Am. Soc. Mass Spectrom.*, 13(4):354–361, April 2002.

[119] V. V. Laiko, N. I. Taranenko, and V. M. Doroshenko. On the mechanism of ion formation from the aqueous solutions irradiated with 3 µm IR laser pulses under atmospheric pressure. *J. Mass Spectrom.*, 41(10):1315–1321, 2006.

[120] S. König, O. Kollas, and K. Dreisewerd. Generation of Highly Charged Peptide and Protein Ions by Atmospheric Pressure Matrix-Assisted Infrared Laser Desorption/Ionization Ion Trap Mass Spectrometry. *Anal. Chem.*, 79(14):5484–5488, July 2007.

[121] A. Vertes, P. Nemes, B. Shrestha, A. A. Barton, Z. Chen, and Y. Li. Molecular imaging by Mid-IR laser ablation mass spectrometry. *Appl. Phys. A*, 93(4):885–891, December 2008.

[122] J. S. Sampson and D. C. Muddiman. Atmospheric pressure infrared (10.6 µm) laser desorption electrospray ionization (IR-LDESI) coupled to a LTQ Fourier transform ion cyclotron resonance mass spectrometer. *Rapid Commun. Mass Spectrom.*, 23(13):1989–1992, 2009.

[123] R. Hiraguchi, H. Hazama, K. Senoo, Y. Yahata, K. Masuda, and K. Awazu. Continuous Flow Atmospheric Pressure Laser Desorption/Ionization Using a 6–7-µm-Band Mid-Infrared Tunable Laser for Biomolecular Mass Spectrometry. *Int. J. Mol. Sci.*, 15(6):10821–10834, June 2014.

[124] J. Villatoro, M. Zühlke, D. Riebe, J. Riedel, T. Beitz, and H.-G. Löhmannsröben. IR-MALDI ion mobility spectrometry. *Anal. Bioanal. Chem.*, 408(23):6259–6268, September 2016.

[125] Y. Iguchi, H. Hazama, and K. Awazu. Continuous flow reduced-pressure infrared laser desorption/ionization mass spectrometry. *Rapid Commun. Mass Spectrom.*, 31(21):1845–1850, 2017.

[126] J. I. Brauer, I. B. Beech, and J. Sunner. Mass Spectrometric Imaging Using Laser Ablation and Solvent Capture by Aspiration (LASCA). *J. Am. Soc. Mass Spectrom.*, 26(9):1538–1547, September 2015.

[127] J. F. Cahill, V. Kertesz, and G. J. Van Berkel. Characterization and Application of a Hybrid Optical Microscopy/Laser Ablation Liquid Vortex Capture/Electrospray Ionization System for Mass Spectrometry Imaging with Sub-micrometer Spatial Resolution. *Anal. Chem.*, 87(21):11113–11121, November 2015.

[128] J. T. O'Brien, E. R. Williams, and H.-Y. N. Holman. Ambient Infrared Laser Ablation Mass Spectrometry (AIRLAB-MS) of Live Plant Tissue with Plume Capture by Continuous Flow Solvent Probe. *Anal. Chem.*, 87(5):2631–2638, March 2015.

[129] A. Vaikkinen, B. Shrestha, T. J. Kauppila, A. Vertes, and R. Kostiainen. Infrared Laser Ablation Atmospheric Pressure Photoionization Mass Spectrometry. *Anal. Chem.*, 84(3):1630–1636, February 2012.

[130] A. Vaikkinen, B. Shrestha, J. Koivisto, R. Kostiainen, A. Vertes, and T. J. Kauppila. Laser ablation atmospheric pressure photoionization mass spectrometry imaging of phytochemicals from sage leaves. *Rapid Commun. Mass Spectrom.*, 28(23):2490–2496, 2014.

[131] J. Soltwisch, H. Kettling, S. Vens-Cappell, M. Wiegelmann, J. Müthing, and K. Dreisewerd. Mass spectrometry imaging with laser-induced postionization. *Science*, 348(6231):211–215, April 2015.

[132] J. Balog, T. Szaniszlo, K.-C. Schaefer, J. Denes, A. Lopata, L. Godorhazy, D. Szalay, L. Balogh, L. Sasi-Szabo, M. Toth, and Z. Takats. Identification of Biological Tissues by Rapid Evaporative Ionization Mass Spectrometry. *Anal. Chem.*, 82(17):7343–7350, September 2010.

[133] O. Golf, N. Strittmatter, T. Karancsi, S. D. Pringle, A. V. M. Speller, A. Mroz, J. M. Kinross, N. Abbassi-Ghadi, E. A. Jones, and Z. Takats. Rapid Evaporative Ionization Mass Spectrometry Imaging Platform for Direct Mapping from Bulk Tissue and Bacterial Growth Media. *Anal. Chem.*, 87(5):2527–2534, March 2015.

[134] L. R. Compton, B. Reschke, J. Friend, M. Powell, and A. Vertes. Remote laser ablation electrospray ionization mass spectrometry for non-proximate analysis of biological tissues. *Rapid Commun. Mass Spectrom.*, 29(1):67–73, 2015.

[135] J. A. Fincher, A. R. Korte, B. Reschke, N. J. Morris, M. J. Powell, and A. Vertes. Enhanced sensitivity and metabolite coverage with remote laser ablation electrospray ionization-mass spectrometry aided by coaxial plume and gas dynamics. *Analyst*, 142(17):3157–3164, August 2017.

[136] B. Fatou, P. Saudemont, E. Leblanc, D. Vinatier, V. Mesdag, M. Wisztorski, C. Focsa, M. Salzet, M. Ziskind, and I. Fournier. In vivo Real-Time Mass Spectrometry for Guided Surgery Application. *Sci. Rep.*, 6:25919, May 2016.

[137] B. Fatou, M. Ziskind, P. Saudemont, J. Quanico, C. Focsa, M. Salzet, and I. Fournier. Remote Atmospheric Pressure Infrared Matrix-Assisted Laser Desorption-Ionization Mass Spectrometry (Remote IR-MALDI MS) of Proteins. *Mol. Cell. Proteomics*, 17(8):1637–1649, August 2018.

[138] M. K. Passarelli, A. Pirkl, R. Moellers, D. Grinfeld, F. Kollmer, R. Havelund, C. F. Newman, P. S. Marshall, H. Arlinghaus, M. R. Alexander, A. West, S. Horning, E. Niehuis, A. Makarov, C. T. Dollery, and I. S. Gilmore. The 3d OrbiSIMS—label-free metabolic imaging with subcellular lateral resolution and high mass-resolving power. *Nat. Methods*, page nmeth.4504, November 2017.

[139] A. Zavalin, J. Yang, K. Hayden, M. Vestal, and R. M. Caprioli. Tissue protein imaging at 1 μm laser spot diameter for high spatial resolution and high imaging speed using transmission geometry MALDI TOF MS. *Anal. Bioanal. Chem.*, 407(8):2337–2342, March 2015.

[140] M. Kompauer, S. Heiles, and B. Spengler. Atmospheric pressure MALDI mass spectrometry imaging of tissues and cells at 1.4-μm lateral resolution. *Nat. Methods*, 14(1):90–96, January 2017.

[141] W. Hang, Z. Yin, X. Cheng, R. Liu, X. Li, L. Hang, J. Xu, X. Yan, J. Li, and Z. Tian. Chemical and topographical single-cell imaging by near-field desorption mass spectrometry. *Angew. Chem. Int. Ed.*, (58):4541, 2019.

[142] J. Soltwisch, G. Göritz, J. H. Jungmann, A. Kiss, D. F. Smith, S. R. Ellis, and R. M. Heeren. MALDI Mass Spectrometry Imaging in Microscope Mode with Infrared Lasers: Bypassing the Diffraction Limits. *Anal. Chem.*, 86(1):321–325, January 2014.

[143] K. Awazu, H. Hazama, T. Hamanaka, J. Aoki, M. Toyoda, and Y. Naito. Tissue imaging with a stigmatic mass microscope using laser desorption/ionization. In *Imaging, Manipulation, and Analysis of Biomolecules, Cells, and Tissues X*, volume 8225, page 82252E. International Society for Optics and Photonics, February 2012.

[144] Y. Li, B. Shrestha, and A. Vertes. Atmospheric Pressure Molecular Imaging by Infrared MALDI Mass Spectrometry. *Anal. Chem.*, 79(2):523–532, January 2007.

[145] K. Dreisewerd, F. Draude, S. Kruppe, A. Rohlfing, S. Berkenkamp, and G. Pohlentz. Molecular Analysis of Native Tissue and Whole Oils by Infrared Laser Mass Spectrometry. *Anal. Chem.*, 79(12):4514–4520, June 2007.

[146] Y. Coello, A. D. Jones, T. C. Gunaratne, and M. Dantus. Atmospheric Pressure Femtosecond Laser Imaging Mass Spectrometry. *Anal. Chem.*, 82(7):2753–2758, April 2010.

[147] V. Venugopalan, N. S. Nishioka, and B. B. Mikić. Thermodynamic response of soft biological tissues to pulsed infrared-laser irradiation. *Biophys. J.*, 70(6):2981–2993, June 1996.

[148] A. Rohlfing, C. Menzel, L. M. Kukreja, F. Hillenkamp, and K. Dreisewerd. Photoacoustic Analysis of Matrix-Assisted Laser Desorption/Ionization Processes with Pulsed Infrared Lasers. *J. Phys. Chem. B*, 107(44):12275–12286, November 2003.

[149] S. N. Jackson, J.-K. Kim, J. L. Laboy, and K. K. Murray. Particle formation by infrared laser ablation of glycerol: implications for ion formation. *Rapid Commun. Mass Spectrom.*, 20(8):1299–1304, April 2006.

[150] X. Fan, M. W. Little, and K. K. Murray. Infrared laser wavelength dependence of particles ablated from glycerol. *Appl. Surf. Sci.*, 255(5, Part 1):1699–1704, December 2008.

[151] S. N. Jackson, S. Mishra, and K. K. Murray. Characterization of Coarse Particles Formed by Laser Ablation of MALDI Matrixes. *J. Phys. Chem. B*, 107(47):13106–13110, November 2003.

[152] T. Musapelo and K. K. Murray. Particle Formation in Ambient MALDI Plumes. *Anal. Chem.*, 83(17):6601–6608, September 2011.

[153] S. Amoruso, G. Ausanio, R. Bruzzese, L. Gragnaniello, L. Lanotte, M. Vitiello, and X. Wang. Characterization of laser ablation of solid targets with near-infrared laser pulses of 100 fs and 1 ps duration. *Appl. Surf. Sci.*, 252(13):4863–4870, April 2006.

[154] S. S. Harilal, P. K. Diwakar, M. P. Polek, and M. C. Phillips. Morphological changes in ultrafast laser ablation plumes with varying spot size. *Opt. Express*, 23(12):15608–15615, June 2015.

[155] N. Farid, S. S. Harilal, H. Ding, and A. Hassanein. Emission features and expansion dynamics of nanosecond laser ablation plumes at different ambient pressures. *J. Appl. Phys.*, 115(3):033107, January 2014.

[156] A. A. Puretzky, D. B. Geohegan, G. B. Hurst, M. V. Buchanan, and B. S. Luk'yanchuk. Imaging of Vapor Plumes Produced by Matrix Assisted Laser Desorption: A Plume Sharpening Effect. *Phys. Rev. Lett.*, 83(2):444–447, July 1999.

[157] T. L. Merrigan, D. J. Timson, C. A. Hunniford, M. Catney, and R. W. McCullough. Plume characteristics and dynamics of UV and IR laser-desorbed oligonucleotides. *Int. J. Biol. Macromol.*, 50(4):1081–1090, May 2012.

[158] A. Vogel, I. Apitz, S. Freidank, and R. Dijkink. Sensitive high-resolution white-light Schlieren technique with a large dynamic range for the investigation of ablation dynamics. *Opt. Lett.*, 31(12):1812–1814, June 2006.

[159] O. Minte, J. Soltwisch, and K. Dreisewerd. A shadowgraphy technique for visualizing the plume development in MALDI/MALDI-2 at high spatio-temporal resolution. Rostock, 2019.

[160] M. K. Kim. *Digital Holographic Microscopy: Principles, Techniques, and Applications*. Springer Series in Optical Sciences. Springer-Verlag, New York, 2011.

[161] B. Kemper, D. D. Carl, J. Schnekenburger, I. Bredebusch, M. Schäfer, W. Domschke, and G. v. Bally. Investigation of living pancreas tumor cells by digital holographic microscopy. *J. Biomed. Opt.*, 11(3):034005, May 2006.

[162] C. Canalias, V. Pasiskevicius, F. Laurell, S. Grilli, P. Ferraro, and P. De Natale. In situ visualization of domain kinetics in flux grown KTiOPO4 by digital holography. *J. Appl. Phys.*, 102(6):064105, September 2007.

[163] P. Ferraro, S. Grilli, D. Alfieri, S. D. Nicola, A. Finizio, G. Pierattini, B. Javidi, G. Coppola, and V. Striano. Extended focused image in microscopy by digital holography. *Opt. Express*, 13(18):6738–6749, September 2005.

[164] C. P. McElhinney, B. M. Hennelly, and T. J. Naughton. Extended focused imaging for digital holograms of macroscopic three-dimensional objects. *Appl. Opt.*, 47(19):D71–D79, July 2008.

[165] T. Colomb, N. Pavillon, J. Kühn, E. Cuche, C. Depeursinge, and Y. Emery. Extended depth-of-focus by digital holographic microscopy. *Opt. Lett.*, 35(11):1840–1842, June 2010.

[166] F. Merola, P. Memmolo, L. Miccio, R. Savoia, M. Mugnano, A. Fontana, G. D'Ippolito, A. Sardo, A. Iolascon, A. Gambale, and P. Ferraro. Tomographic flow cytometry by digital holography. *Light Sci. Appl.*, 6(4):e16241, April 2017.

[167] A. Urniežius, N. Šiaulys, V. Kudriašov, V. Sirutkaitis, and A. Melninkaitis. Application of time-resolved digital holographic microscopy in studies of early femtosecond laser ablation. *Appl. Phys. A*, 108(2):343–349, June 2012.

[168] N. Šiaulys, L. Gallais, and A. Melninkaitis. Direct holographic imaging of ultrafast laser damage process in thin films. *Opt. Lett.*, 39(7):2164–2167, April 2014.

[169] K. Choudhury, R. K. Singh, S. Narayan, A. Srivastava, and A. Kumar. Time resolved interferometric study of the plasma plume induced shock wave in confined geometry: Two-dimensional mapping of the ambient and plasma density. *Phys. Plasmas*, 23(4):042108, April 2016.

[170] D. Breitling, H. Schittenhelm, P. Berger, F. Dausinger, and H. Hügel. Shadowgraphic and interferometric investigations on Nd:YAG laser-induced vapor/plasma plumes for different processing wavelengths. *Appl. Phys. A*, 69(1):S505–S508, December 1999.

[171] Z. Chen and A. Vertes. Early plume expansion in atmospheric pressure midinfrared laser ablation of water-rich targets. *Phys. Rev. E*, 77(3):036316, March 2008.

[172] E. Amer, P. Gren, and M. Sjödahl. Shock wave generation in laser ablation studied using pulsed digital holographic interferometry. *J. Phys. D.*, 41(21):215502, 2008.

[173] E. Amer, P. Gren, and M. Sjödahl. Laser-ablation-induced refractive index fields studied using pulsed digital holographic interferometry. *Opt. Lasers Eng.*, 47(7):793–799, July 2009.

[174] M. Takeda, H. Ina, and S. Kobayashi. Fourier-transform method of fringe-pattern analysis for computer-based topography and interferometry. *J. Opt. Soc. Am.*, 72(1):156–160, January 1982.

[175] P. Ferraro, S. D. Nicola, A. Finizio, G. Coppola, S. Grilli, C. Magro, and G. Pierattini. Compensation of the inherent wave front curvature in digital holographic coherent microscopy for quantitative phase-contrast imaging. *Appl. Opt.*, 42(11):1938–1946, April 2003.

[176] V. V. Temnov, K. Sokolowski-Tinten, P. Zhou, and D. v. d. Linde. Femtosecond time-resolved interferometric microscopy. *Appl. Phys. A*, 78(4):483–489, January 2004.

[177] T. Colomb, J. Kühn, F. Charrière, C. Depeursinge, P. Marquet, and N. Aspert. Total aberrations compensation in digital holographic microscopy with a reference conjugated hologram. *Opt. Express*, 14(10):4300–4306, May 2006.

[178] M. A. Herráez, D. R. Burton, M. J. Lalor, and M. A. Gdeisat. Fast two-dimensional phase-unwrapping algorithm based on sorting by reliability following a noncontinuous path. *Appl. Opt.*, 41(35):7437–7444, December 2002.

[179] V. V. Temnov, K. Sokolowski-Tinten, P. Zhou, and D. v. d. Linde. Ultrafast imaging interferometry at femtosecond-laser-excited surfaces. *J. Opt. Soc. Am. B*, 23(9):1954–1964, September 2006.

[180] A. Vogel, B. Kersten, and I. Apitz. Material ejection in free-running Er:YAG laser ablation of water, liver, and skin. In *Proc. SPIE*, volume 4961 of *Laser-Tissue Interaction XIV*, pages 40–48. International Society for Optics and Photonics, August 2003.

[181] G. Taylor. The Formation of a Blast Wave by a Very Intense Explosion. I. Theoretical Discussion. *Proc. Royal Soc. A*, 201(1065):159–174, March 1950.

[182] D. A. Freiwald and R. A. Axford. Approximate spherical blast theory including source mass. *J. Appl. Phys.*, 46(3):1171–1174, March 1975.

[183] G. J. Hutchens. Approximate near-field blast theory: A generalized approach. *J. Appl. Phys.*, 88(6):3654–3658, August 2000.

[184] S. H. Jeong, R. Greif, and R. E. Russo. Propagation of the shock wave generated from excimer laser heating of aluminum targets in comparison with ideal blast wave theory. *Appl. Surf. Sci.*, 127–129:1029–1034, May 1998.

[185] E. d. Posada, M. A. Arronte, L. Ponce, E. Rodríguez, T. Flores, and J. G. Lunney. On the use of shockwave models in laser produced plasma expansion. *J. Phys.: Conf. Ser.*, 274(1):012078, 2011.

[186] T. A. Schmitz, J. Koch, D. Günther, and R. Zenobi. Early plume and shock wave dynamics in atmospheric-pressure ultraviolet-laser ablation of different matrix-assisted laser ablation matrices. *J. Appl. Phys.*, 109(12):123106, June 2011.

[187] G. Callies, P. Berger, and H. Hugel. Time-resolved observation of gas-dynamic discontinuities arising during excimer laser ablation and their interpretation. *J. Phys. D*, 28(4):794, 1995.

[188] I. Apitz and A. Vogel. Material ejection in nanosecond Er:YAG laser ablation of water, liver, and skin. *Appl. Phys. A*, 81(2):329–338, March 2005.

[189] X. Fan and K. K. Murray. Wavelength and Time-Resolved Imaging of Material Ejection in Infrared Matrix-Assisted Laser Desorption. *J. Phys. Chem. A*, 114(3):1492–1497, January 2010.

[190] M. A. Mackanos, J. A. Kozub, D. L. Hachey, K. M. Joos, D. L. Ellis, and E. D. Jansen. The effect of free-electron laser pulse structure on mid-infrared soft-tissue ablation: biological effects. *Phys. Med. Biol.*, 50(8):1885, 2005.

[191] A. Rohlfing, A. Leisner, F. Hillenkamp, and K. Dreisewerd. Investigation of the Desorption Process in UV Matrix-Assisted Laser Desorption/Ionization with a Liquid 3-Nitrobenzyl Alcohol Matrix by Photoacoustic Analysis, Fast-Flash Imaging, and UV-Laser Postionization. *J. Phys. Chem. C*, 114(12):5367–5381, April 2010.

[192] D. Breitling, A. Ruf, and F. Dausinger. Fundamental aspects in machining of metals with short and ultrashort laser pulses. *Proc. SPIE*, 5339:49–64, July 2004.

[193] J. Noack and A. Vogel. Laser-induced plasma formation in water at nanosecond to femtosecond time scales: calculation of thresholds, absorption coefficients, and energy density. *IEEE J. Quantum Electron.*, 35(8):1156–1167, August 1999.

[194] N. Linz, S. Freidank, X.-X. Liang, H. Vogelmann, T. Trickl, and A. Vogel. Wavelength dependence of nanosecond infrared laser-induced breakdown in water: Evidence for multiphoton initiation via an intermediate state. *Phys. Rev. B*, 91(13):134114, April 2015.

[195] P. E. Nielsen and G. H. Canavan. Laser Absorption Waves in the Atmosphere. In *Laser Interaction and Related Plasma Phenomena*, pages 177–189. Springer, Boston, MA, 1974.

[196] S.-B. Wen, X. Mao, R. Greif, and R. E. Russo. Laser ablation induced vapor plume expansion into a background gas. II. Experimental analysis. *J. Appl. Phys.*, 101(2):023115, January 2007.

[197] A. Gojani. Laser ablation at the hydrodynamic regime. *EPJ Web Conf.*, 45:01124, April 2013.

[198] M. H. Goetz, F. Baptista, J. P. Fischer, C. Messer, N. Suhm, and J. F. Bille. Plasma-mediated ablation using picosecond UV and IR laser pulses and spectroscopical investigations of the plasma spark. In H. J. Albrecht, G. P. Delacretaz, T. H. Meier, R. W. Steiner, L. O. Svaasand, and M. J. C. van Gemert, editors, *Proc. SPIE*, volume 2323 of *Laser Interaction with Hard and Soft Tissue II*, pages 218–226, 1995.

[199] V. Dribinski, A. Ossadtchi, V. A. Mandelshtam, and H. Reisler. Reconstruction of Abel-transformable images: The Gaussian basis-set expansion Abel transform method. *Rev. Sci. Instrum.*, 73(7):2634–2642, July 2002.

[200] PyAbel. Documentation v. 0.7.

[201] J. H. Gladstone and T. P. Dale. Researches on the Refraction, Dispersion, and Sensitiveness of Liquids. *Phil. Trans. R. Soc. Lond.*, 153:317–343, January 1863.

[202] K. P. Birch and M. J. Downs. An Updated Edlén Equation for the Refractive Index of Air. *Metrologia*, 30(3):155, 1993.

[203] R. A. Alpher and D. R. White. Optical Refractivity of High-Temperature Gases. I. Effects Resulting from Dissociation of Diatomic Gases. *Phys. Fluids*, 2(2):153, 1959.

[204] C. Porneala and D. A. Willis. Time-resolved dynamics of nanosecond laser-induced phase explosion. *J. Phys. D*, 42(15):155503, 2009.

[205] L. I. Sedov. *Similarity and dimensional methods in mechanics.* Academic Press, New York, NY, 1959.

[206] X. Feng, B.-F. Liu, J. Li, and X. Liu. Advances in coupling microfluidic chips to mass spectrometry. *Mass Spectrom. Rev.*, 34(5):535–557, September 2015.

[207] X. Wang, L. Yi, N. Mukhitov, A. M. Schrell, R. Dhumpa, and M. G. Roper. Microfluidics-to-mass spectrometry: A review of coupling methods and applications. *J. Chromatogr. A*, 1382:98–116, February 2015.

[208] W. Feng, E. Ueda, and P. A. Levkin. Droplet Microarrays: From Surface Patterning to High-Throughput Applications. *Adv. Mater.*, 30(20):1706111, May 2018.

[209] S. K. Küster, M. Pabst, K. Jefimovs, R. Zenobi, and P. S. Dittrich. High-Resolution Droplet-Based Fractionation of Nano-LC Separations onto Microarrays for MALDI-MS Analysis. *Anal. Chem.*, 86(10):4848–4855, May 2014.

[210] M. Pabst, S. R. Fagerer, R. Köhling, S. K. Küster, R. Steinhoff, M. Badertscher, F. Wahl, P. S. Dittrich, K. Jefimovs, and R. Zenobi. Self-Aliquoting Microarray Plates for Accurate Quantitative Matrix-Assisted Laser Desorption/Ionization Mass Spectrometry. *Anal. Chem.*, 85(20):9771–9776, October 2013.

[211] W. Nischkauer, F. Vanhaecke, and A. Limbeck. Self-aliquoting micro-grooves in combination with laser ablation-ICP-mass spectrometry for the analysis of challenging

liquids: quantification of lead in whole blood. *Anal. Bioanal. Chem.*, 408(21):5671–5676, August 2016.

[212] F. Lapierre, G. Piret, H. Drobecq, O. Melnyk, Y. Coffinier, V. Thomy, and R. Boukherroub. High sensitive matrix-free mass spectrometry analysis of peptides using silicon nanowires-based digital microfluidic device. *Lab Chip*, 11(9):1620–1628, May 2011.

[213] A. Zarrine-Afsar, C. Müller, F. O. Talbot, and R. J. D. Miller. Self-Localizing Stabilized Mega-Pixel Picoliter Arrays with Size-Exclusion Sorting Capabilities. *Anal. Chem.*, 83(3):767–773, February 2011.

[214] K. L. Vodopyanov. Saturation studies of H2o and HDO near 3400 cm-1 using intense picosecond laser pulses. *J. Chem. Phys.*, 94(8):5389–5393, April 1991.

[215] J. M. Martin-Garcia, C. E. Conrad, J. Coe, S. Roy-Chowdhury, and P. Fromme. Serial femtosecond crystallography: A revolution in structural biology. *Arch. Biochem. Biophys.*, 602:32–47, July 2016.

[216] Z. Huang, T. Ossenbrüggen, I. Rubinsky, M. Schust, D. A. Horke, and J. Küpper. Development and Characterization of a Laser-Induced Acoustic Desorption Source. *Anal. Chem.*, 90(6):3920–3927, March 2018.

[217] A. V. Bulgakov, N. Goodfriend, O. Nerushev, N. M. Bulgakova, S. V. Starinskiy, Y. G. Shukhov, and E. E. B. Campbell. Laser-induced transfer of nanoparticles for gas-phase analysis. *J. Opt. Soc. Am. B*, 31(11):C15–C21, November 2014.

[218] Y. Dong, B. Li, S. Malitsky, I. Rogachev, A. Aharoni, F. Kaftan, A. Svatoš, and P. Franceschi. Sample Preparation for Mass Spectrometry Imaging of Plant Tissues: A Review. *Front. Plant Sci.*, 7, 2016.

[219] R. W. Nelson, R. M. Thomas, and P. Williams. Time-of-flight mass spectrometry of nucleic acids by laser ablation and ionization from a frozen aqueous matrix. *Rapid Commun. Mass Spectrom.*, 4(9):348–351, 1990.

[220] D. M. Schieltz, C.-W. Chou, C.-W. Luo, R. M. Thomas, P. Williams, and C. H. Becker. Mass spectrometry of DNA mixtures by laser ablation from frozen aqueous solution. *Rapid Commun. Mass Spectrom.*, 6(10):631–636, 1992.

[221] P. Williams. Time of flight mass spectrometry of DNA laser-ablated from frozen aqueous solutions: applications to the Human Genome Project. *Int. J. Mass Spectrom. Ion Process.*, 131:335–344, February 1994.

[222] J. I. Berry, S. Sun, Y. Dou, A. Wucher, and N. Winograd. Laser Desorption and Imaging of Proteins from Ice via UV Femtosecond Laser Pulses. *Anal. Chem.*, 75(19):5146–5151, October 2003.

[223] C. Focsa, B. Chazallon, and J. L. Destombes. Resonant desorption of ice with a tunable LiNbO3 optical parametric oscillator. *Surf. Sci.*, 528(1):189–195, March 2003.

[224] B. L. Henderson and M. S. Gudipati. Plume Composition and Evolution in Multicomponent Ices Using Resonant Two-Step Laser Ablation and Ionization Mass Spectrometry. *J. Phys. Chem. A*, 118(29):5454–5463, July 2014.

[225] C. Mihesan, M. Ziskind, B. Chazallon, C. Focsa, and J. L. Destombes. Formation of large water clusters by IR laser resonant desorption of ice. *Appl. Surf. Sci.*, 248(1):238–242, July 2005.

[226] A. Leisner, A. Rohlfing, S. Berkenkamp, F. Hillenkamp, and K. Dreisewerd. Infrared laser post-ionization of large biomolecules from an IR-MALD(I) plume. *J. Am. Soc. Mass Spectrom.*, 15(6):934–941, June 2004.

[227] D. M. Murphy and T. Koop. Review of the vapour pressures of ice and supercooled water for atmospheric applications. *Q. J. Royal Meteorol. Soc.*, 131(608):1539–1565, 2005.

[228] K. Amann-Winkel, R. Böhmer, F. Fujara, C. Gainaru, B. Geil, and T. Loerting. Colloquium: Water's controversial glass transitions. *Rev. Mod. Phys.*, 88(1):011002, February 2016.

[229] M. Schürenberg, K. Dreisewerd, S. Kamanabrou, and F. Hillenkamp. Influence of the sample temperature on the desorption of matrix molecules and ions in matrix-assisted laser desorption ionization. *Int. J. Mass Spectrom. Ion Process.*, 172(1):89–94, January 1998.

[230] W. C. Wiley and I. H. McLaren. Time-of-Flight Mass Spectrometer with Improved Resolution. *Review of Scientific Instruments*, 26(12):1150–1157, December 1955.

[231] M. L. Vestal. Modern MALDI time-of-flight mass spectrometry. *J. Mass Spectrom.*, 44(3):303–317, March 2009.

[232] A. Holle, A. Haase, M. Kayser, and J. Höhndorf. Optimizing UV laser focus profiles for improved MALDI performance. *J. Mass Spectrom.*, 41(6):705–716, June 2006.

[233] D. Feldhaus, C. Menzel, S. Berkenkamp, F. Hillenkamp, and K. Dreisewerd. Influence of the laser fluence in infrared matrix-assisted laser desorption/ionization with a 2.94 µm Er : YAG laser and a flat-top beam profile. *J. Mass Spectrom.*, 35(11):1320–1328, November 2000.

[234] L. A. McDonnell and R. M. Heeren. Imaging mass spectrometry. *Mass Spectrom. Rev.*, 26(4):606–643, July 2007.

[235] A. Vertes, L. Balazs, and R. Gijbels. Matrix-assisted laser desorption of peptides in transmission geometry. *Rapid Commun. Mass Spectrom.*, 4(7):263–266, July 1990.

[236] Bruker. Guide to MALDI Sample Preparation, 2015.

[237] K. Dreisewerd, M. Schürenberg, M. Karas, and F. Hillenkamp. Influence of the laser intensity and spot size on the desorption of molecules and ions in matrix-assisted laser desorption/ionization with a uniform beam profile. *Int. J. Mass Spectrom. Ion Process.*, 141(2):127–148, February 1995.

[238] R. Liu, Q. Li, and L. M. Smith. Detection of Large Ions in Time-of-Flight Mass Spectrometry: Effects of Ion Mass and Acceleration Voltage on Microchannel Plate Detector Response. *J. Am. Soc. Mass Spectrom.*, 25(8):1374–1383, August 2014.

[239] G. R. Kinsel, L. M. Preston, and D. H. Russell. Fragmentation of vitamin B12 during 337 nm matrix-assisted laser desorption ionization. *Biol. Mass Spectrom.*, 23(4):205–211, 1994.

[240] S. L. Cohen and B. T. Chait. Influence of Matrix Solution Conditions on the MALDI-MS Analysis of Peptides and Proteins. *Anal. Chem.*, 68(1):31–37, January 1996.

[241] J. B. Fenn. Electrospray Wings for Molecular Elephants (Nobel Lecture). *Angew. Chem. Int. Ed.*, 42(33):3871–3894, 2003.

Acknowledgments

I would like to start by thanking Prof. R. J. Dwayne Miller for his untamed enthusiasm, for providing a goal to work towards, and for letting me be part of his vision of where science can take us. Thank you for your guidance and patience. I would like to thank Prof. Dr. Robert H. Blick for his willingness to co-referee my work, and Prof. Dr. Arwen Pearson, Prof. Dr. Daniela Pfannkuche, and Dr. Sadia Bari for being part of my thesis defense committee. I also thank Arwen for always keeping the doors of her labs open to us. Special thanks go to our sub-group leaders: Dr. Wesley D. Robertson, thank you for your trust, calmness, and support during the first three years of my PhD and beyond. It was this atmosphere of no wrong ideas and your encouragement for out-of-the-box thinking that let me grow confident in our work. To Dr. Sascha W. Epp, for the numerous interesting chats and discussions, for always asking the right questions, and for the ability to get to the bottom of things. And to Dr. Heinrich-Schwoerer, for making sure no one was left hanging.

I also want to thank all the engineers and technicians who were an invaluable source of knowledge and contributed substantially to the success of the project: Friedjof Tellkamp who could probably write a whole thesis of his own on the design of the ion source and load-lock, Hendrik Schikora who did an exceptional job of installing the cryo-cooling and was always there to help with the vacuum instrumentation, Joseph Gonschior who designed the vacuum chamber and more, Djordje Gitaric who never tired of our ideas for improvement of the ion optics and designed the multiple iterations that were tried out over the years, Martin Kollewe who helped whenever there was an electronics problem more difficult than soldering a single contact, Jan-Philipp Leimkohl who helped with improving the sample mount, and Toru Matsuyama who provided valuable insights into high-frequency electronics and semiconducting surfaces. Moreover, I am deeply grateful for the many helping hands behind the scenes, especially Ulrike Krieger, Tania Hartin, Carolin Wodars, Kathja Schroeder, Nadja Bardenheuer and Kirsten Teschke. Important contributions to the work presented in this thesis were also made by Sebastian Kruber, Kristina Strahlendorff, Brandon Reber, Dennis Eggert, and Ayman Mostafa, as was mentioned in each chapter's preamble. A big thanks to all of you.

On a more personal note, I want to thank my closest colleagues and friends in the Miller group: Lourie Pieterse, Johannes Kaub, and Andrey Krutilin, for the inexhaustible discussions, moral support, and companionship that made my time at the Max Planck Institute so enjoyable. Thanks also go to the rest of the group, and especially to Stefanie Meyer and my officemate Robert Bücker, for providing discussions, tools, and an atmosphere that welcomed life beyond science. The same goes for all my PhD fellows within the International Max-Planck Research School for Ultrafast Imaging (IMPRS-UFAST). I had a wonderful time over the last few years. Thanks also to our coordinators Sonja Utermann, Julia Quante, and Neda Lotfiomran.

Finally, I would like to thank my friends and family who have supported me and stood by my side throughout this time. To my parents, who always found kind and motivating words to cheer me up. Thank you for trusting in my decisions, and helping me out whenever I encountered obstacles in life. To my newfound friends in Hamburg, Marta, Lorena, Diana, Riccardo, for being the amazing people you are. To all the people I have woefully neglected during the last stressful months, thank you for keeping in touch. And to Shruti Patel, for your example, your wisdom, and your love.